

International Journal of Antennas and Propagation

# Small Antennas: Miniaturization Techniques and Applications 2016

Guest Editors: Wenhua Yu, Yingsong Li, and Manos M. Tentzeris





---

**Small Antennas: Miniaturization Techniques  
and Applications 2016**



International Journal of Antennas and Propagation

---

**Small Antennas: Miniaturization Techniques  
and Applications 2016**

Guest Editors: Wenhua Yu, Yingsong Li, and Manos M. Tentzeris



---

Copyright © 2016 Hindawi Publishing Corporation. All rights reserved.

This is a special issue published in “International Journal of Antennas and Propagation.” All articles are open access articles distributed under the Creative Commons Attribution License, which permits unrestricted use, distribution, and reproduction in any medium, provided the original work is properly cited.

## Editorial Board

Ana Alejos, Spain  
Mohammad Ali, USA  
Jaume Anguera, Spain  
Rodolfo Araneo, Italy  
Alexei Ashikhmin, USA  
Herve Aubert, France  
Paolo Baccarelli, Italy  
Xiulong Bao, Ireland  
Toni Björninen, Finland  
Stefania Bonafoni, Italy  
Djuradj S. Budimir, UK  
Paolo Burghignoli, Italy  
Shah Nawaz Burokur, France  
Giuseppe Castaldi, Italy  
Luca Catarinucci, Italy  
Felipe Catedra, Spain  
Marta Cavagnaro, Italy  
Deb Chatterjee, USA  
Shih Yuan Chen, Taiwan  
Yu Jian Cheng, China  
Renato Cicchetti, Italy  
Riccardo Colella, Italy  
Lorenzo Crocco, Italy  
Claudio Curcio, Italy  
Francesco D'Agostino, Italy  
M. E. de Cos Gómez, Spain  
Tayeb A. Denidni, Canada  
Giuseppe Di Massa, Italy  
Michele D'Urso, Italy  
Hala A. Elsadek, Egypt

Francisco Falcone, Spain  
M. Ferrando Bataller, Spain  
Flaminio Ferrara, Italy  
Vincenzo Galdi, Italy  
Claudio Gennarelli, Italy  
Farid Ghanem, Algeria  
Sotirios K. Goudos, Greece  
Rocco Guerriero, Italy  
Kerim Guney, Turkey  
Song Guo, Japan  
Mohamed Himdi, France  
Tamer S. Ibrahim, USA  
Mohammad T. Islam, Malaysia  
M. R. Kamarudin, Malaysia  
Kyeong Jin Kim, USA  
Slawomir Koziel, Iceland  
Luis Landesa, Spain  
Ding-Bing Lin, Taiwan  
Angelo Liseno, Italy  
Pierfrancesco Lombardo, Italy  
Giampiero Lovat, Italy  
Lorenzo Luini, Italy  
Atsushi Mase, Japan  
Diego Masotti, Italy  
Giuseppe Mazzeola, Italy  
C. F. Mecklenbräuker, Austria  
M. Migliozzi, Italy  
A. T. Mobashsher, Australia  
Ananda S. Mohan, Australia  
J.-M. Molina-Garcia-Pardo, Spain

Marco Mussetta, Italy  
N. Nasimuddin, Singapore  
Miguel Navarro-Cia, UK  
Mourad Nedil, Canada  
Symeon Nikolaou, Cyprus  
Giacomo Oliveri, Italy  
Pablo Otero, Spain  
A. D. Panagopoulos, Greece  
Ikmo Park, Republic of Korea  
Josep Parrón, Spain  
Matteo Pastorino, Italy  
Massimiliano Pieraccini, Italy  
Xianming Qing, Singapore  
Ahmad Safaai-Jazi, USA  
S. Safavi-Naeini, Canada  
M. Salazar-Palma, Spain  
Stefano Selleri, Italy  
Prabhakar Singh, India  
Raffaele Solimene, Italy  
Gino Sorbello, Italy  
Seong-Youp Suh, USA  
Sheng Sun, Hong Kong  
Larbi Talbi, Canada  
Luciano Tarricone, Italy  
Parveen Wahid, USA  
Wen-Qin Wang, China  
Shiwen Yang, China  
Yuan Yao, China  
Jingjing Zhang, Denmark



# Contents

---

**Small Antennas: Miniaturization Techniques and Applications 2016**

Wenhua Yu, Yingsong Li, and Manos M. Tentzeris  
Volume 2016, Article ID 9410108, 2 pages

**Spiral Slotted Microstrip Antenna Design for 700 MHz Band Application**

Ricardo Meneses González, R. Linares y Miranda, and R. Leyva Hernández  
Volume 2016, Article ID 1879287, 7 pages

**Miniaturized Dielectric Resonator Antenna Array for GNSS Applications**

S. Caizzone, G. Buchner, and W. Elmarissi  
Volume 2016, Article ID 2564087, 10 pages

**Design of a Compact Quad-Band Slot Antenna for Integrated Mobile Devices**

Jian Dong, Xiaping Yu, and Guoqiang Hu  
Volume 2016, Article ID 3717681, 9 pages

**A Novel Compact Dual-Polarized Antenna**

Yong Cheng, Yadan Li, and Wenjun Lu  
Volume 2016, Article ID 6304356, 5 pages

**A Miniaturized Meandered Dipole UHF RFID Tag Antenna for Flexible Application**

Xiuwei Xuan, Lianrong Lv, and Kun Li  
Volume 2016, Article ID 2951659, 7 pages

**An Optimal Electric Dipole Antenna Model and Its Field Propagation**

Yidong Xu, Lili Guo, Wei Xue, Korochentsev Vladimir, and Junwei Qi  
Volume 2016, Article ID 8601497, 8 pages

## Editorial

# Small Antennas: Miniaturization Techniques and Applications 2016

Wenhua Yu,<sup>1</sup> Yingsong Li,<sup>2</sup> and Manos M. Tentzeris<sup>3</sup>

<sup>1</sup>2COMU Inc., Fairfax, VA, USA

<sup>2</sup>College of Information and Communications Engineering, Harbin Engineering University, Harbin 150001, China

<sup>3</sup>School of Electrical and Computer Engineering, Georgia Institute of Technology, Atlanta, GA 30308, USA

Correspondence should be addressed to Wenhua Yu; [wenyu@2comu.com](mailto:wenyu@2comu.com)

Received 1 September 2016; Accepted 1 September 2016

Copyright © 2016 Wenhua Yu et al. This is an open access article distributed under the Creative Commons Attribution License, which permits unrestricted use, distribution, and reproduction in any medium, provided the original work is properly cited.

The development of small antennas for modern communications, for both portable terminals and radar purposes, has been widely studied over many years. In recent decades, this topic is experiencing an ever increasing concentration, thanks to the antenna miniaturization techniques and printed antenna techniques. Recently reported antenna techniques pave the way to new added-value designs of small antennas for mobile devices and military applications and even for healthcare detections and enable full exploitation for the integration of the antenna and radio frequency front-ends. However, the antennas used in modern communication equipment have unique challenges in design theory and in implementation, which need new development in the antenna design and geometry design in small antenna creation.

The papers included in this special issue provide a wide view of small antenna designs, which includes the antenna designs and applications in communication system. This special issue comprises the antenna designs for long-term evolution (LTE), radio-frequency identification (RFID), global navigation satellite system (GNSS), and mobile devices. Additionally, the optimal electric dipole antenna model and its application have also been included in this special issue.

As for the LTE antenna design, the authors created a spiral slotted microstrip antenna to meet the requirements of 700 MHz band application, which can also be used for terrestrial digital television. The antenna has been well designed and measured for obtaining good impedance

and gain. For mobile communications, a quad-band slot antenna and a dual-polarization antenna have been reported and investigated in detail. The quad-band slot antenna has been presented for personal communications service (PCS), universal mobile telecommunications system (UMTS), wide-band code-division multiple access (WCDMA), Bluetooth, wireless local area networks (WLAN), and worldwide interoperability for microwave access (WiMAX) applications and the dual-polarization antenna has been developed for 1801 MHz–1827 MHz applications. Also, an RFID antenna has been designed for ultrahigh frequency (UHF) at 860–960 MHz, which has been verified by both simulation and experiments. The results demonstrated that the UHF RFID antenna can provide a read range of 3 m–4 m with a minimum threshold power of 23–26 dBm. Furthermore, a dielectric resonator antenna (DRA) array has been presented herein for giving a good service for GNSS to exploit the potentialities of precise and reliable navigation. The antenna operates at E5/L5, L2, and E6 bands with an overall footprint of only 3.5". In addition, an optimal electric dipole antennas model has been presented, analyzed, and measured in a through-the-earth communication system to obtain a vertical transmission depth about 30 m.

We hope that this special issue can give useful information and light the antenna designs within the minimization and high performance and can attract much more attention by the academia and industrial community to pursue further investigations to promote the rapid design of small antennas.

## **Acknowledgments**

We appreciatingly thank all the authors for their useful designs and informative contributions. We also give thanks to all the reviewers for their continuous support and their constructive comments for promoting the publication process.

*Wenhua Yu*  
*Yingsong Li*  
*Manos M. Tentzeris*

## Research Article

# Spiral Slotted Microstrip Antenna Design for 700 MHz Band Application

**Ricardo Meneses González, R. Linares y Miranda, and R. Leyva Hernández**

*Instituto Politécnico Nacional, Escuela Superior de Ingeniería Mecánica y Eléctrica, Laboratorio de Compatibilidad Electromagnética, Campus Zacatenco, Colonia Lindavista, 07738 Ciudad de México, Mexico*

Correspondence should be addressed to Ricardo Meneses González; [rmeneseg@ipn.mx](mailto:rmeneseg@ipn.mx)

Received 4 February 2016; Revised 29 June 2016; Accepted 11 July 2016

Academic Editor: Yingsong Li

Copyright © 2016 Ricardo Meneses González et al. This is an open access article distributed under the Creative Commons Attribution License, which permits unrestricted use, distribution, and reproduction in any medium, provided the original work is properly cited.

This work describes the design and implementation of spiral slotted microstrip antenna. Recently, just like other countries, in Mexico, terrestrial digital television has been implemented (analogic shutdown); as a consequence, the 700 MHz UHF Band (698–806 MHz) has been opened to new telecommunications services, particularly wireless mobile communication. This technological advance represents a radio mobile antenna design challenge because it is necessary to design an antenna whose dimensions must be small enough, which satisfies gain, resonance frequency, and bandwidth requirements and is of low cost.

## 1. Introduction

It is widely known that, a long time ago and nowadays, the frequency bands have been assigned by the government through laws implemented by itself or by owners of big businesses; as consequence, the transmitted information quantity using the free space as transmission media (radio communications services) is too much, that is, radio, TV, radio cellular, and so forth, which have saturated the electromagnetic spectrum causing slow communications and ineffective utilization of the radio spectrum, and particularly radio cellular bands are overloaded in most countries; this way, a great part of the radio frequency electromagnetic spectrum is used in an inefficient way; most of the time, some other frequency bands are only partially or largely unoccupied and the remaining frequency bands are heavily used [1–4].

As far as that is concerned, it is a unique opportunity in order to make the end of the old analogic TV and the beginning of the digital TV easy; just like in other countries, the Mexican Government has established some changes to telecommunications laws since June 2013.

Particularly, according to one of the states, “the concessionaires and official agents have an essential requirement to give the frequency bands back to the Mexican State, which

initially were granted permission to attend the TV broadcasting service, as soon as the transition to the terrestrial digital television (TDT) has already been done, in order to guarantee the efficient use of the radio electric spectrum, as well as encourage a fair competition and an optimal use of the 700 MHz UHF Band” [2].

This work proposes a spiral slotted microstrip antenna, single turn and half turn, whose resonance frequency can be designed along the 700 MHz UHF Band (698–806 MHz) LTE, variable when some antenna dimensions are adjusted. To determine the performance of the design parameter, as impedance, resonance frequency, radiation pattern, and polarization, HFSS simulation software has been used and experimental tests under an anechoic camera have been applied.

The paper is organized as follows. Section 2 describes brief antenna design foundations; Section 3 describes simulation and measurements results; Section 4 presents a discussion; and Section 5 comprises conclusions and references.

## 2. Antenna Design

*2.1. Design Foundations.* Some of the most used design techniques to miniaturize an antenna are the vertical meandering

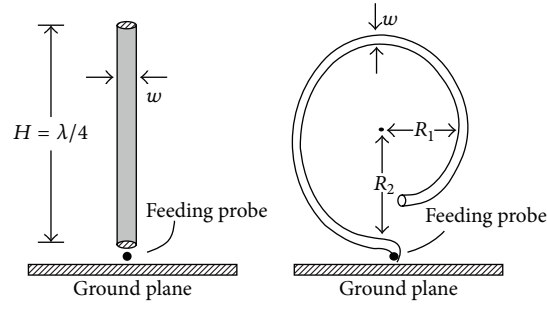


FIGURE 1: Quarter wavelength monopole,  $\lambda/4$ , twisted to form a single turn spiral microstrip antenna.

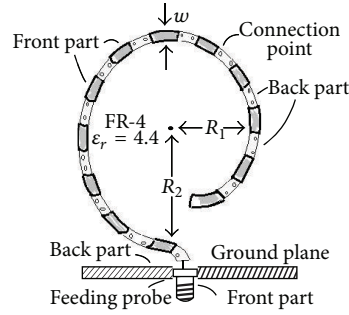


FIGURE 2: Single turn spiral slotted microstrip antenna geometry.

and the slotted line. Several papers have used these techniques in order to reduce the antenna size; for instance, [5–7] apply the first one to  $\lambda/2$  dipole, meandering the wire; on the other hand [7, 8], the second technique applies to a printed spiral patch antenna using slots or small truncated segments.

In our case, these techniques are applied to a single  $\lambda/4$  monopole, a quarter-wavelength monopole which is reduced to form a single turn spiral microstrip antenna [9], as shown in Figure 1. Based on [7], it is divided into a set of symmetric rectangular small segments jointly connected in both faces and firmly fastened to small rectangular ground plane, in order to perturb the TM modes and produce circular polarization, as shown in Figure 2.

Two orthogonal modes are produced by the effect of perturbation created by the slots or small truncated segments. The paper [7] has proved that if the number of segments increases, the resonance frequency value decreases. Also, in order to achieve the resonance frequency value along the 700 MHz UHF Band and satisfy the small size antenna, we propose a second antenna, half-turn spiral slotted microstrip antenna, as shown in Figure 3.

On the other hand, because the circuit has been broken down into unit sections, the antenna can be seen as a transmission line divided into circuit elements and considered to be lumped, so the currents on the symmetric and adjacent segments have opposite phase, in accordance with the line transmission theory. Meanwhile,  $N$  increases, the antenna shows a smaller resonant width because the wire is folded, the gain is achieved with the highest radiation resistance when the total wire length is the smallest, and the main lobe of the radiation pattern tends to be thin.

Hence, the antenna can be considered as  $N$  segments and circuit elements, circularly aligned; all elements adjacent to each other are separated by a distance  $d$  (expressed in wavelengths) and if it is considerably small, they can be seen as linearly uniform; thus, the linear array theory [10, 11] can be applied, which establishes the notion that the electric field in the far field is given by [12, 13]

$$|E_T| = |E_0 + E_1 e^{j\Psi} + E_2 e^{j2\Psi} + E_3 e^{j3\Psi} + \dots + E_{N-1} e^{j(N-1)\Psi}|. \quad (1)$$

But a modification in the phase factor  $\Psi$  should be considered, an increment of  $\phi$  angle, caused by the circular orientation of each element, given by

$$\Psi = \beta d \cos[\phi + n(\Delta\phi)] + \alpha, \quad (2)$$

where  $\Delta\phi = 2\pi/N$ , which is azimuth angle, and  $E_n$  is the electric field amplitude generated by each element.  $d(\lambda)$  is the spacing distance between adjacent elements.  $\alpha$  is the progressive phase shift between elements.  $N$  is the number of elements. And  $n = 1, 2, 3, \dots, N-1$ ,  $\beta = 2\pi/\lambda$ , and  $\alpha$  is the angle by which the current in any element leads the current in the preceding element.

This way, the relative electric field can be expressed as

$$\left| \frac{E_T}{E_0} \right| = \left[ \frac{\sin(N\Psi/2)}{\sin(\Psi/2)} \right]. \quad (3)$$

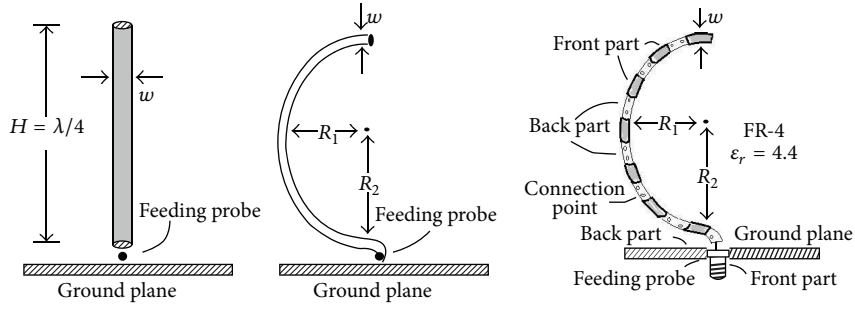


FIGURE 3: Half-turn spiral slotted microstrip antenna geometry.

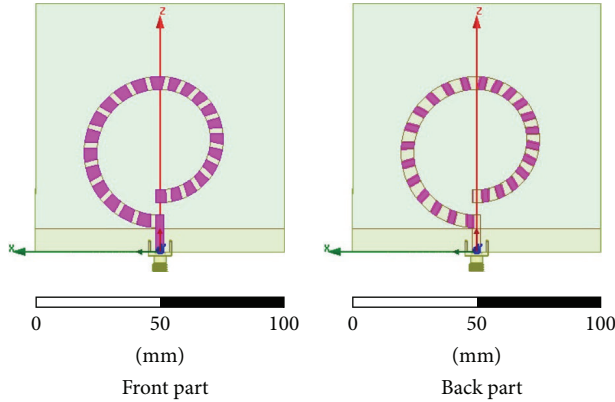


FIGURE 4: Spiral slotted antenna simulation.

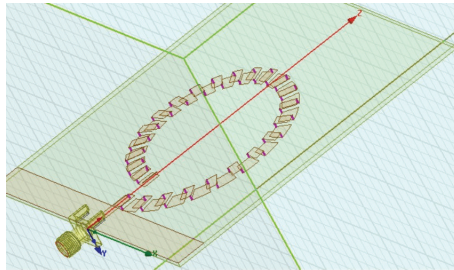


FIGURE 5: Perspective view.

On the other hand, in order to calculate the resonance frequency, [14] proposes the following expression:

$$f_r = \frac{nc}{4\pi r \sqrt{\epsilon_r}}, \quad (4)$$

where  $f_r$  is resonance frequency,  $r$  is spiral radius,  $\epsilon_r$  is electric permittivity, and  $n = 1$ .

Applying this expression and considering  $r = 0.015$  m,  $\epsilon_r = 4.4$  (FR-4), and  $n = 1$ , the calculated resonance frequency value is approximately 750 MHz.

### 3. Simulation and Measurement

Both antennas have been simulated and measured. HFSS software [15] has been used to simulate the designed antennas, satisfying the following requirements:

- (i) Operation frequency  $f_{res} = 750$  MHz ( $\lambda \approx 40$  cm).
- (ii) Internal radius  $R_1 = 1.5$  cm.

- (iii) External radius  $R_2 = 2.5$  cm.
- (iv) Material: FR4.
- (v) Spacing distance between adjacent segments:  $\phi = 15^\circ$  ( $\pi/12$ ).
- (vi) Spiral perimeter ( $2\pi R_1 = \lambda/4 \approx 10$  cm).

**3.1. Single Turn Spiral Slotted Microstrip Antenna.** Figure 4 shows the front part and back part of the simulated antenna, where  $N = 24$ , and Figure 5 shows a perspective view. Figure 6 shows magnitude versus frequency simulation graphic, parameter  $S_{11}$ , which represents how much power is reflected from the antenna and hence is known as the reflection coefficient or return loss. It is possible to observe that the resonance frequency value is equal to 700 MHz, and the wideband is equal to 100 MHz. The simulation process allowed identifying the necessary dimension adjustments in

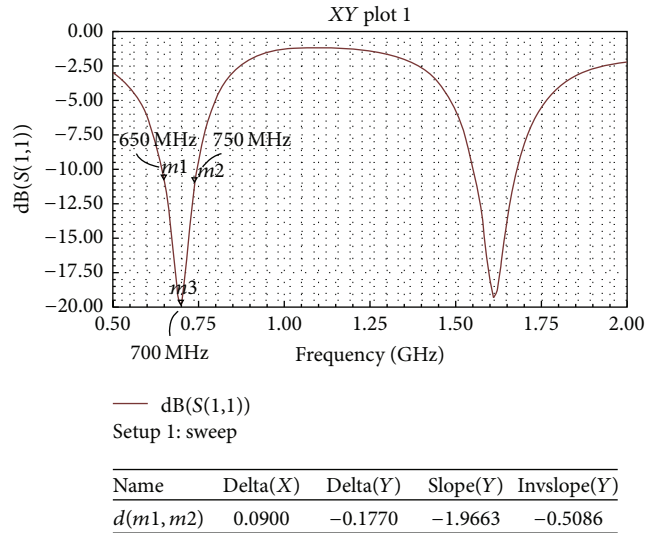


FIGURE 6: Magnitude versus frequency (simulation).

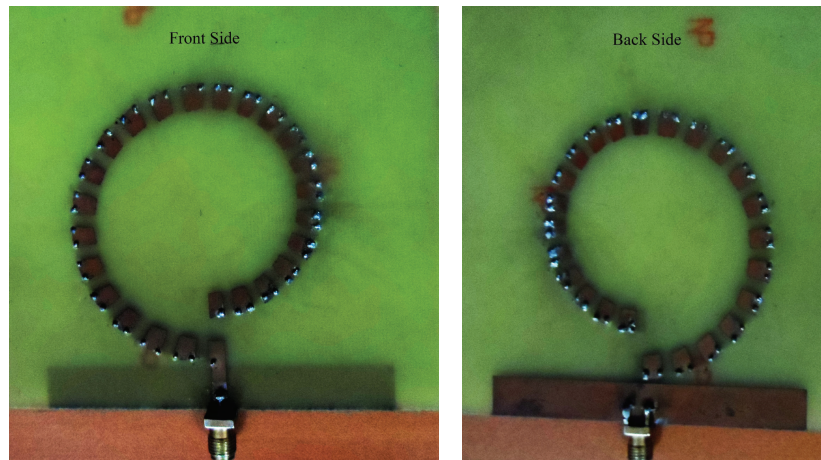


FIGURE 7: Prototype antenna.

order to achieve the resonance frequency along the 700 MHz UHF Band.

Figures 7 and 8 show the prototype antenna and the antenna under test in the anechoic camera, respectively, which is built using Epoxy glass fibre FR-4; hence,  $\epsilon_r = 4.4$ , which is electric permittivity, and SMA connector is used. Vector Network Analyzer ZVB 40, calibrated in the band 500 MHz–2 GHz, has been used to measure the resonance frequency of the designed antenna, and Figure 9 shows the obtained measurement, magnitude versus frequency graphic, parameter  $S_{11}$ . It is possible to observe that the resonance frequency of the designed antenna is equal to 717 MHz, with magnitude  $-16$  dB and wideband approximately 50 MHz.

Figure 10 shows the simulated and measured (Plane E) radiation pattern. It can be seen as a semicircle shape, due to scan-blindness phenomena and the scattering behavior in the printed phased arrays.

3.2. Half-Turn Spiral Slotted Microstrip Antenna. In the same way, HFSS software [15] has been used to simulate the



FIGURE 8: Prototype antenna under test (anechoic camera).

designed antenna; Figure 11 shows the prototype antenna, but unlike the single turn spiral antenna this one uses  $N = 12$ ,



FIGURE 9: Magnitude versus frequency (measurement).

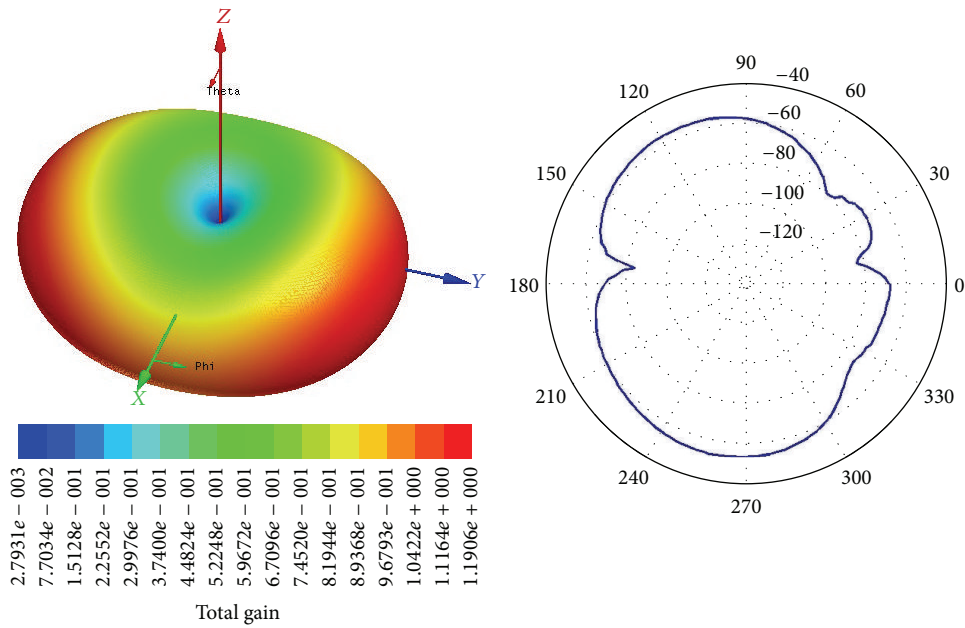


FIGURE 10: Radiation pattern graphic (measurement), single turn spiral.



FIGURE 11: Prototype antenna.

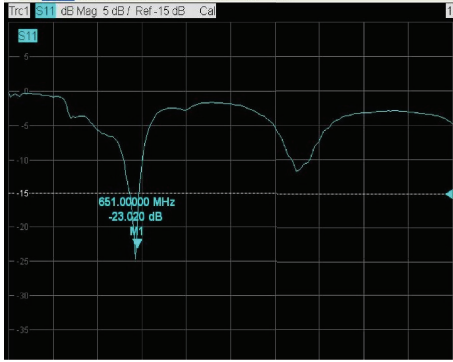


FIGURE 12: Magnitude versus frequency (measurement).

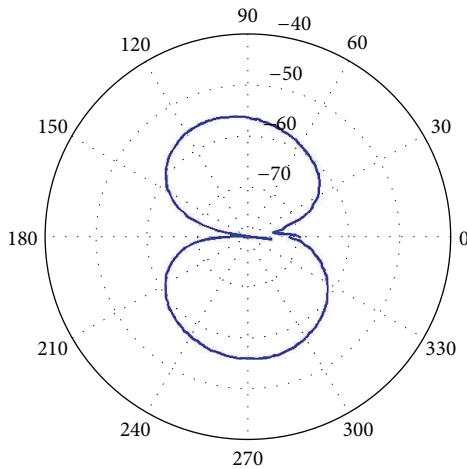


FIGURE 13: Radiation pattern graphic (measurement).

and the radius dimensions have changed; that is,  $R_1 = 2.5$  cm and  $R_2 = 3$  cm.

Figure 12 shows magnitude versus frequency measured graphic, parameter  $S_{11}$ . It is possible to observe the resonance frequency value equal to 651 MHz,  $-23$  dB, below 700 MHz Band; this value can be increased if the number of segments decreases, in this case by 10 or 11 segments.

Figure 13 shows the radiation pattern. It is possible to observe nulls in the radiation pattern, along the  $0^\circ$ – $180^\circ$  position; the radiation is low, reducing the efficiency of the antenna.

#### 4. Discussion

It is possible to observe that there are small differences, in particular the resonance frequency value of the half-turn spiral antenna, 651 MHz, between the simulation and experimental results, due to construction anomalies, that is, inappropriate soldering, unequal segments, the low quality of the SMA connector, and so forth; this can be corrected by decreasing the number of segments. On the other hand, mismatch, large radiation loss, polarization distortion, several nulls, relatively narrow bandwidth, and low directivity can be improved by combining more segments into the

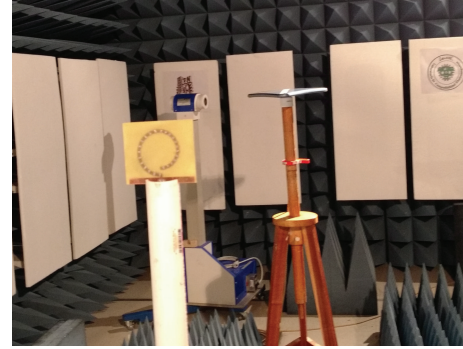


FIGURE 14: Antenna gain measurement method.

array, but this action carries serious problems, that is, scan-blindness phenomena and the scattering behavior in printed phased arrays. In that respect, [16] refers scan blindness to a condition where, for a certain scan angle, no real power can be transmitted (or received) by a phased array. This situation is observed in the radiation pattern achieved, which shows along the  $170^\circ$ ,  $45^\circ$ , and  $15^\circ$  position. Even though it is a counterproductive action, the current method to improve the bandwidth consists of increasing the ground patch separation using a thicker substrate, because the interaction between the segments degrades array efficiency, producing surface wave modes; mutual coupling results in impedance mismatch, considerable radiation loss, and scan blindness in phase array antennas [17]; therefore, in order to avoid these collateral harmful effects which reduce the antenna efficiency, the insertion of a defected ground structure (DGS) is recommended; in that sense, the spiral acts as a DGS, because it can be seen as a defect etched in the ground plane of the microstrip, disturbing the shield current distribution circulating along it, modifying the characteristics of a transmission line, and increasing effective capacitance and inductance; this situation can be seen comparing the radiation patterns of the designed antennas.

Finally, in order to measure and calculate the antenna gain, a second known antenna was used as a reference, placing both antennas into the anechoic camera, spaced 2.1 m apart, as shown in Figure 14; this way, considering the overall transmission loss (free space and cable loss), antenna gain is approximately equal to 1.5 dB.

#### 5. Conclusion

Spiral microstrip antennas have been designed, single turn and half turn, using uniform slotted line technique, meeting the resonance frequency, with an appropriate geometry of the radiation pattern. The achieved results show the feasibility of this kind of small antenna to be used on radio mobile devices operating at 700 MHz UHF Band.

#### Competing Interests

The authors declare that they have no competing interests.

## References

- [1] “700 MHz Device Flexibility Promotes Competition,” Peter Cramton, <http://www.cramton.umd.edu/papers2010-2014/cramton-700-mhz-device-flexibility-promotes-competition.pdf>.
- [2] <http://eleconomista.com.mx/industrias/2015/07/05/banda-700mhz-estara-liberada-100-septiembre-sct>.
- [3] L. K. Moore, “The first responder network and next-generation communications for public safety: issues for congress,” Congressional Research Service (CRS) Report for Congress 7-5700, 2012.
- [4] M. McHenry, “Frequency agile spectrum access technologies,” in *Proceedings of the FCC Cognitive Radio Workshop*, Washington, DC, USA, May 2003.
- [5] K.-L. Wong, *Compact and Broadband Microstrip Antennas*, John Wiley & Sons, Inc., New York, NY, USA, 2002.
- [6] J. Rashed and C.-T. Tai, “A new class of resonant antennas,” *IEEE Transactions on Antennas and Propagation*, vol. 39, no. 9, pp. 1428–1430, 1991.
- [7] L. Deng, S.-F. Li, K.-L. Lau, and Q. Xue, “Vertical meandering approach for antenna size reduction,” *International Journal of Antennas and Propagation*, vol. 2012, Article ID 980252, 5 pages, 2012.
- [8] J. M. Kim and J. G. Yook, “Compact mender-type slot antennas,” in *Proceedings of the IEEE Antennas and Propagation Society International Symposium*, vol. 2, pp. 724–727, IEEE, Boston, Mass., USA, July 2001.
- [9] F.-S. Zhang, Y.-T. Wan, D. Yu, and B. Ye, “A microstrip-fed multiband spiral ring monopole antenna with improved radiation characteristics at higher resonant frequencies,” *Progress In Electromagnetics Research C*, vol. 41, pp. 97–109, 2013.
- [10] J. D. Krauss and R. J. Marhefka, *Antennas for All Applications*, McGraw-Hill, New York, NY, USA, 2002.
- [11] M. Polivka and A. Holub, “Collinear and coparallel principles in antenna design,” in *Proceedings of the Progress in Electromagnetics Research Symposium (PIERS '07)*, pp. 337–341, Prague, Czech, August 2007.
- [12] E. C. Jordan and K. G. Balmain, *Electromagnetic Waves and Radiating Systems*, Prentice Hall, Upper Saddle River, NJ, USA, 1968.
- [13] C. A. Balanis, *Antenna Theory, Analysis and Design*, John Wiley & Sons, 1982.
- [14] L.-H. Hsieh and K. Chang, “Simple analysis of the frequency modes for microstrip ring resonators of any general shape and correction of an error in the literature,” *Microwave and Optical Technology Letters*, vol. 38, no. 3, pp. 209–213, 2003.
- [15] Ansoft Corporation HFSS, <http://www.ansys.com/Products/Electronics/ANSYS-HFSS>.
- [16] D. M. Pozar and D. H. Schaubert, “Scan blindness in infinite phase arrays of printed dipoles,” *IEEE Transactions on Antennas and Propagation*, vol. AP-32, no. 6, pp. 602–610, 1984.
- [17] G. E. Antilla and N. G. Alexopoulos, “Surface wave and related effects on the RCS of microstrip dipoles printed on magnetodielectric substrates,” *IEEE Transactions on Antennas and Propagation*, vol. 39, no. 12, pp. 1707–1715, 1991.

## Research Article

# Miniaturized Dielectric Resonator Antenna Array for GNSS Applications

**S. Caizzone, G. Buchner, and W. Elmarissi**

*Institute of Communications and Navigation, German Aerospace Center (DLR), 82234 Wessling, Germany*

Correspondence should be addressed to S. Caizzone; stefano.caizzone@dlr.de

Received 2 May 2016; Revised 6 June 2016; Accepted 13 June 2016

Academic Editor: Yingsong Li

Copyright © 2016 S. Caizzone et al. This is an open access article distributed under the Creative Commons Attribution License, which permits unrestricted use, distribution, and reproduction in any medium, provided the original work is properly cited.

The increase in global navigation satellite systems (GNSS) availability and services is fostering a new wave of applications related to satellite navigation. Such increase is also followed by more and more threats, aiming at signal disruption. In order to fully exploit the potentialities of precise and reliable navigation, being able at the same time to counteract threats such as interference, jamming, and spoofing, smart antenna systems are being investigated worldwide, with the requirements of multiband operation and compactness. In order to answer such need, the present work proposes a miniaturized dielectric resonator antenna (DRA)  $2 \times 2$  array able to operate at E5/L5, L2, and E6 bands, with an overall footprint of only 3.5" (89 mm).

## 1. Introduction

The increase in GNSS constellations and services alongside with the GPS system, as, for instance, the forthcoming Galileo system, enables a plethora of novel applications concerning the precise positioning of people, vehicles, and goods. Such spreading of the relevance of satellite navigation in different applications also causes more and more interest in malicious attacks, for instance, through jamming or spoofing, to deny the service [1] or even try to deceive the navigation functionality [2].

In order to fully exploit the offered possibilities and at the same time counteract possible threats, high-performance systems, able to steer the antenna pattern and hence place nulls against interferences and maxima at the direction of arrival (DOA) of signals, are being developed all over the world (see, e.g., [3]). These new systems might be particularly useful in mobile applications, such as aircraft or vehicles, where precise localization can play an important role. However, the canonical dimensions of the antennas and of receivers do not fit with the requirements of low profile and low weight, typical of mobile applications: in the aeronautic sector, for instance, the tolerable size is regulated by ARINC standard dimensions [4]. There is hence a need for miniaturization both of the single

radiator and of the overall antenna array, to enable real-life implementation of the developed systems.

Moreover, benefits can be easily foreseen if antennas and receivers are able to process at the same time signals coming from multiple bands, with increases in precision, availability, and robustness [5].

A few different works are already available regarding robust and reliable satellite navigation receivers: in [3], a single band  $2 \times 2$  array is shown, together with a complete receiver, demonstrating the smart antenna capability for interference suppression. Proper algorithms for adaptive array processing for robust navigation are, for instance, reported in [6–8]. Concerning the geometry of the antenna array, different nonplanar geometries are studied in [9–11], showing optimal array performance at low-elevation, but having relatively large dimensions.

On the other hand, in [12], miniaturization of the system (and hence of the antenna array) for use at L1 band is pursued, achieving a size of  $10 \times 10 \text{ cm}^2$  (diameter 141 mm). Moreover, a dual-band system at L1 and L2 bands is reported in [13], having however an overall diameter of 165 mm, hence still too big, for instance for, aeronautical requirements.

The need for further work on antenna miniaturization for GNSS arrays is therefore evident. Antenna miniaturization

can be pursued by means of different techniques (see [14] for a broad review): the geometry of the antenna can be changed by using meandering, effectively enlarging the current path, and hence lowering the resonance frequency [15]; however, this technique usually strongly degrades the polarization purity of circularly polarized antennas, hence not being suited for precise GNSS applications. Material loading is also possible, by using materials with high dielectric or magnetic constants, which effectively provide a wave slowdown and hence antenna miniaturization, normally at the cost of reduced bandwidth. At L-band, there are a few low loss materials with high dielectric constant (DK), while materials with high magnetic constants usually are more lossy at these frequencies and find therefore little application at L-band. Finally, metamaterials, as well as electromagnetic band gap (EBG) materials [16], can be used to pursue miniaturization: they are however usually bulky and would increase relevantly the cost of the antenna.

Among the above techniques, material loading with high DK materials seems particularly promising in GNSS applications, because it allows for strong miniaturization of structures, without affecting polarization purity and without the need for additional layers, as instead is the case for metamaterials.

In this work, therefore, a bulk glass ceramic material with a DK of  $\sim 30$  will be used: this will enable a single antenna diameter of only 30.5 mm, which will then allow obtaining the very compact  $2 \times 2$  array footprint of 89 mm (3.5 inches), remarkably smaller than the ones previously reported and fulfilling compactness requirements.

The single antennas are dielectric resonator antennas (DRAs) and are designed for operation at E5/L2/E6 bands. Special measures will be shown that minimize mutual coupling between the very close radiators.

The paper is therefore divided as follows: Section 2 shows the single antenna design, while array design is explained in Section 3. Measurement results are reported in Section 4. Finally, conclusions are drawn in Section 5.

## 2. Single Antenna Design

*2.1. Modality of Operation.* Dielectric resonators (DRs) [17, 18] have been thoroughly analyzed in the last decades and are now used for various applications, such as microwave filters and oscillators. They have the characteristic property of having very few metal parts and hence exhibit quite low losses even at very high frequency. Thanks to such feature, their use as antennas is now becoming popular, because low losses allow high radiation efficiency. Their behaviour is based on the resonant mode(s) of a dielectric cavity, established by means of a feeding element. Such mode will however not be totally confined into the dielectric material but will also leak out, leading to radiation.

By using dielectric resonator antennas (DRAs) [18] for miniaturized arrays, two additional advantages are available: on one hand, they can make use of very high DK dielectric materials, hence enabling strong miniaturization, while exhibiting a relatively broader bandwidth than microstrip antennas [19]. On the other hand, they are not planar, but

volumetric structures and hence give designers additional degrees of freedom during the design phase.

In the present work, a bulk glass ceramic material from Schott AG (Schott GHz 33, with DK of about 33) has been taken into consideration for the DRA. The high DK value will allow strong miniaturization of the single antenna and therefore permit obtaining a more compact array. The material has superior properties in terms of purity (and hence has minimal DK tolerances) and temperature dependence. The antenna has a cylindrical shape and is placed on a 3.5'' metallic plate (Figure 1(a)).

Two metallic strips, conformal to the DRA surface and soldered to the inner conductor of SMA connectors, act as feeds for the DRA, exciting orthogonal linear polarized fields (namely, mode  $HEM_{11\delta}$  along  $x$ - or  $y$ -axis, resp.). The height of the metallic strips can be properly chosen for optimal matching, hence providing an additional tuning parameter. RHCP polarization is then obtained with the use of a commercial  $90^\circ$  hybrid combiner (ZX10Q-2-19-S+ from Mini-Circuits, exhibiting good behaviour in the whole L-band), connected to the two SMA connectors, that is, to the feeds of the two orthogonal linear fields. Finally, the upper surface of the cylinder is fully covered by copper ("copper cap," Figure 1(a)): this helps [20] in obtaining even further miniaturization.

*2.2. Analysis of the DRA.* In order to fully master the behaviour of the antenna and to identify the tuning parameters for optimal matching, a series of numerical simulations have been performed with an electromagnetic (e.m.) solver, ANSYS HFSS, showing the effect of variable geometrical parameters on the antenna characteristics. In particular, the radius ( $r$ ) and height ( $h$ ) of the DRA cylinder and the length of the copper strips ( $l_{cs}$ ) and the radius of the copper cap ( $r_{cc}$ ) have been taken into account. The results are shown in Figures 2 and 3.

The radius of the cylinder and the radius of the copper cap are mostly effective on the resonance frequency, while the length of the copper strip and the height of the cylinder act mostly on the impedance values (i.e., sharpening or flattening the resonant peaks), hence turning useful in the search for optimal matching once the correct resonance frequency has been found.

The copper cap actually perturbs the fields of mode  $HEM_{11\delta}$  (excited through probe feeding), by imposing a metal boundary condition (i.e., the need for nonzero  $E$ -field components directed only normally to the surface) at the upper face of the DRA. Such perturbation however does not change the essential radiation characteristics of the antenna [21], which remains, as for the pure  $HEM_{11\delta}$  mode, substantially pointing towards zenith (i.e.,  $z$ -axis in Figure 1), as requested for GNSS antennas.

Nevertheless, the presence of the cap produces a shift of the resonance towards lower frequencies, hence providing an easy, yet powerful, way for further miniaturization.

*2.3. Final Design for the Single Antenna.* Using the precious information of the former paragraph, it is possible to optimally match the antenna (in standalone configuration): best

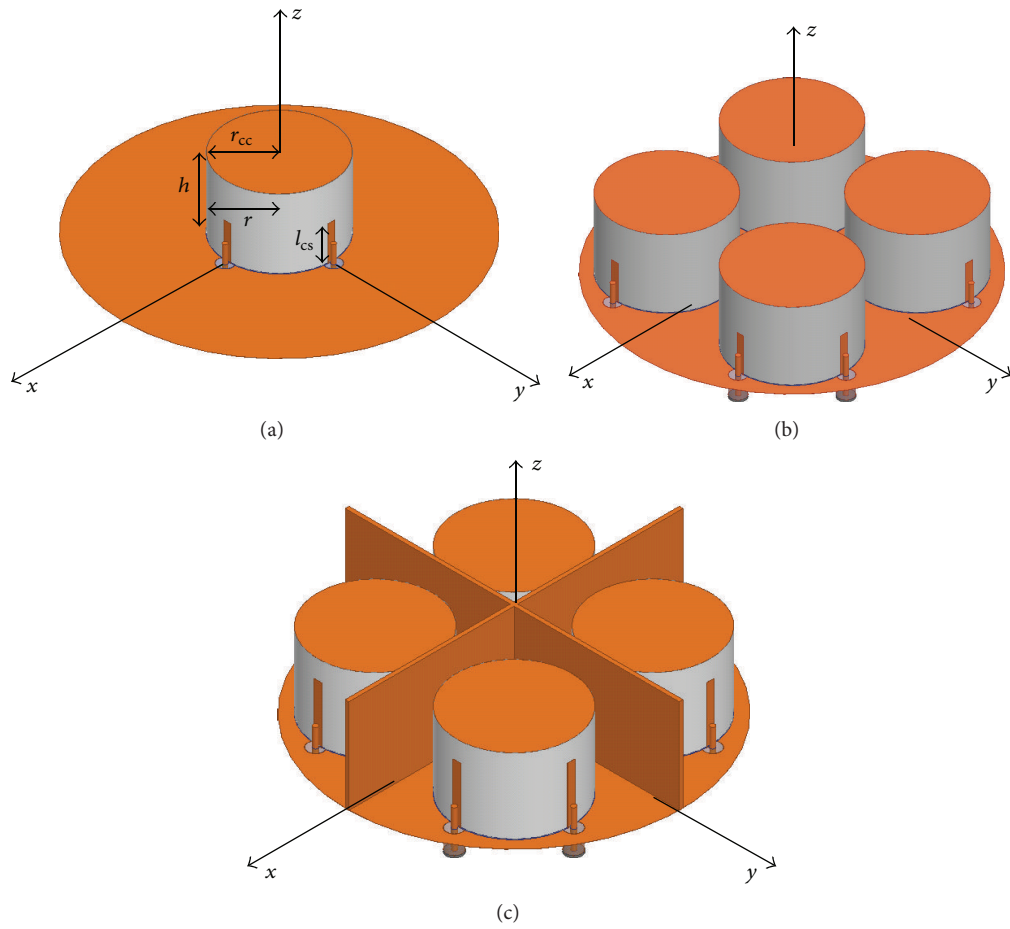


FIGURE 1: 3D view of the single DRA (a) and  $2 \times 2$  DRA array, either without (b) or with metallic fence (c) on a circular ground plane (diameter: 3.5").

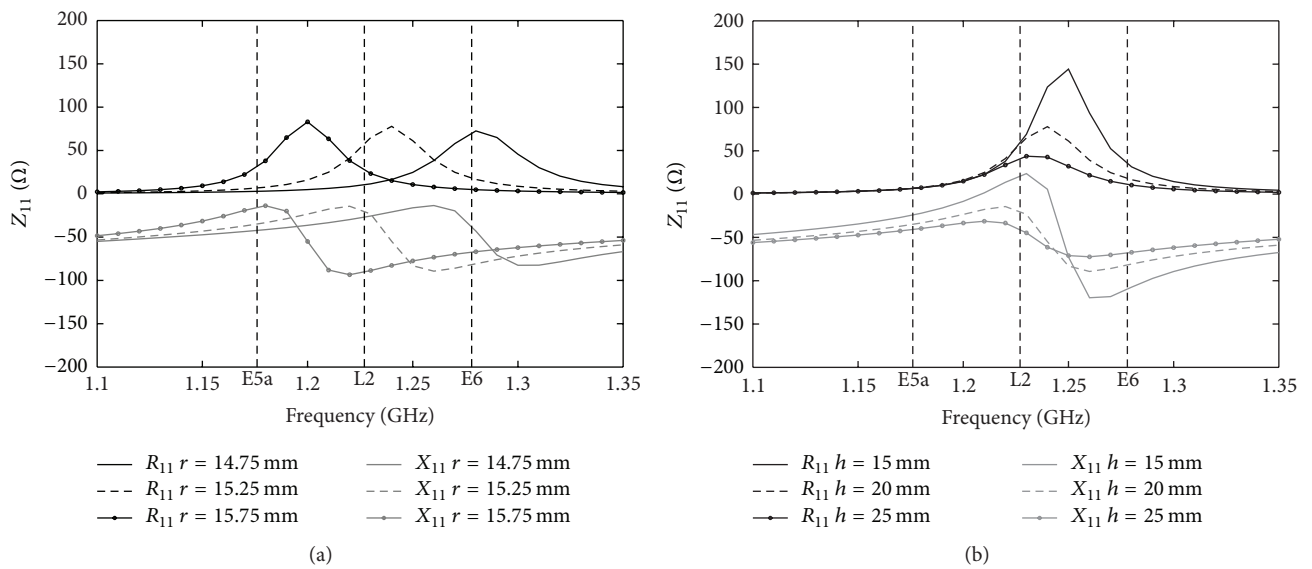


FIGURE 2:  $Z_{11}$  of the single DRA with varying parameters: (a) radius of the DRA cylinder; (b) height of the DRA cylinder.

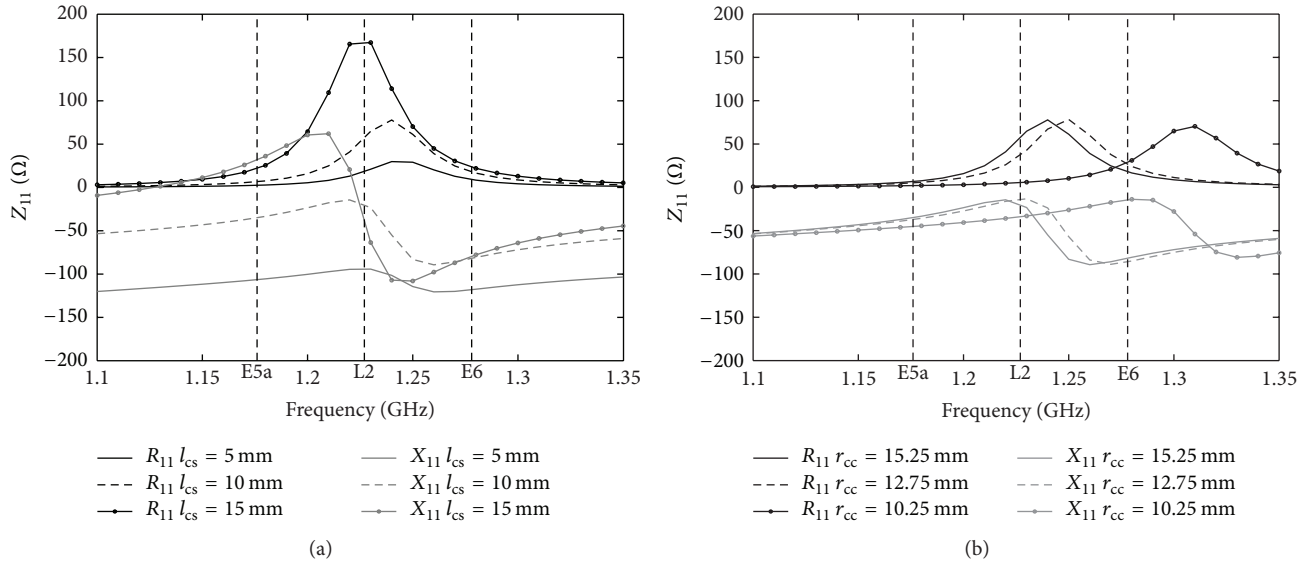


FIGURE 3:  $Z_{11}$  of the single DRA with varying parameters: (a) length of the copper strip; (b) radius of the copper cap.

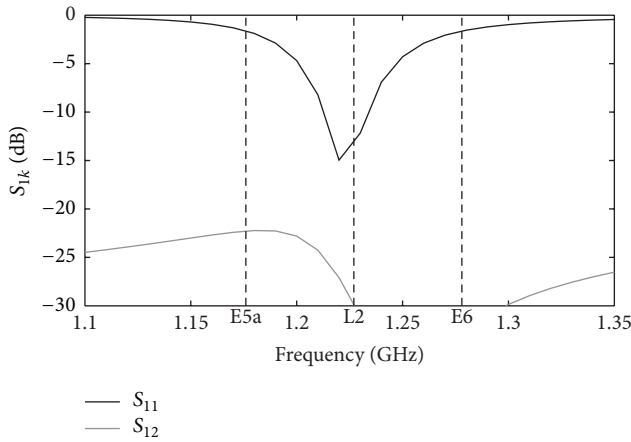


FIGURE 4:  $S_{11}$  and  $S_{12}$  of the single DRA on a circular ground plane (diameter: 3.5'').

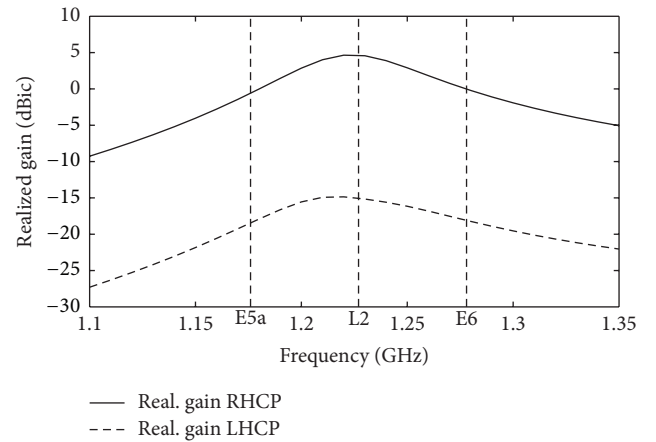


FIGURE 5: Boresight realized gain of the single DRA on a circular ground plane (diameter: 3.5'').

performance is found when the single antenna element has a diameter of 30.5 mm, a height of 20 mm, a length of the copper strips of 10 mm, and a radius of the copper cap of 15.25 mm (Figure 4).

In this case, the antenna achieves the realized gain depicted in Figure 5. As it can be observed, the single antenna has optimal performance both for gain and for matching at L2 band, that is, in the middle of the frequency range covering also E5 and E6 bands. At  $f = 1228$  MHz, the simulated realized gain towards zenith is 4.5 dBic, while it is higher than  $-3$  dBic also at E5a and E6 bands.

### 3. Array Design

The single antenna shown in the previous section has been used as ‘‘building block’’ for the  $2 \times 2$  array. Thanks to

the reduced dimension of the single antenna, very small mutual distances between neighbouring elements are achievable, hence allowing obtaining the required very compact footprint. The antennas have been positioned following a sequentially rotated geometry, in order to help in improving polarization purity of the overall array. A 3D view of the array is shown in Figure 1(b). The array footprint size is 89 mm and the distance between antennas is  $d = 37$  mm. Results for such configuration will be shown in Section 3.1. Metallic fences have later been placed between the antennas, to limit the mutual coupling effects, due to the very close vicinity of antennas ( $d = 37$  mm  $\approx \lambda/7$  at E5 band), as discussed in Section 3.2. Finally, an absorber substrate has been added on top of the fence edges to minimize spurious radiation as shown in Section 3.3.

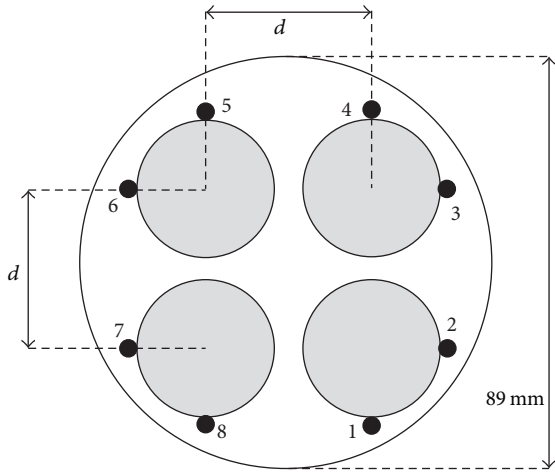


FIGURE 6: Schematic view of the array: each antenna has two ports (exciting two orthogonally polarized fields).

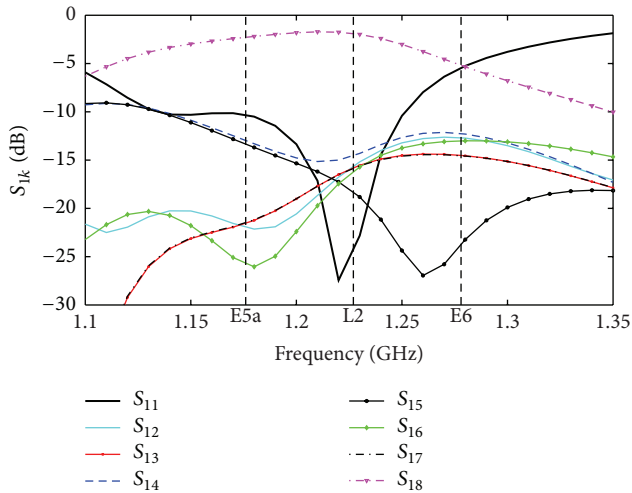


FIGURE 7:  $S_{1k}$  parameters of the DRA array without fences.

3.1. *Miniaturized  $2 \times 2$  Array.* When the antennas are placed in array configuration (sequentially rotated to improve polarization purity), strong mutual coupling is expected between them, due to the very close vicinity.

As a matter of fact, such mutual coupling can be observed in the  $S$ -parameters for port 1 (each antenna has two ports, representing the two feeding probes. The port numbering can be seen in Figure 6) in Figure 7: for instance,  $S_{18} \sim -2$  dB at  $f = 1.228$  GHz, implying that more than half of the power of port 1 is coupled to port 8.

This situation is detrimental, because it strongly reduces both the gain of the antenna (as power is coupled with other ports instead of being radiated/received) and degrades the independence of the signals coming out of each antenna (since the signal will now contain information of multiple ports due to coupling). Moreover, the maximum gain of the embedded antenna decreases and is shifted in frequency (Figure 8).

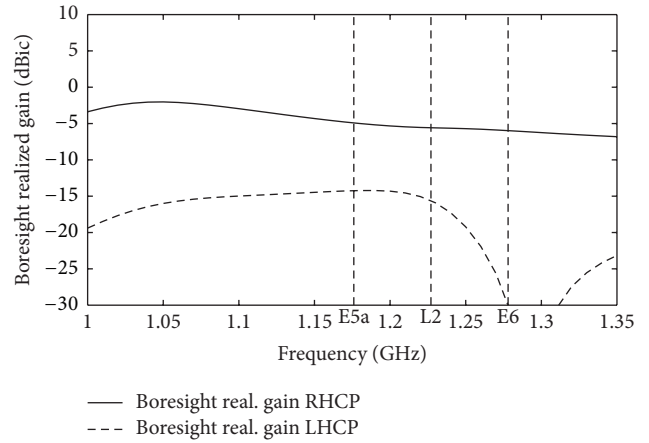


FIGURE 8: Bore sight realized gain of the  $2 \times 2$  array of DRAs without fence for the embedded case (only antenna 1 fed).

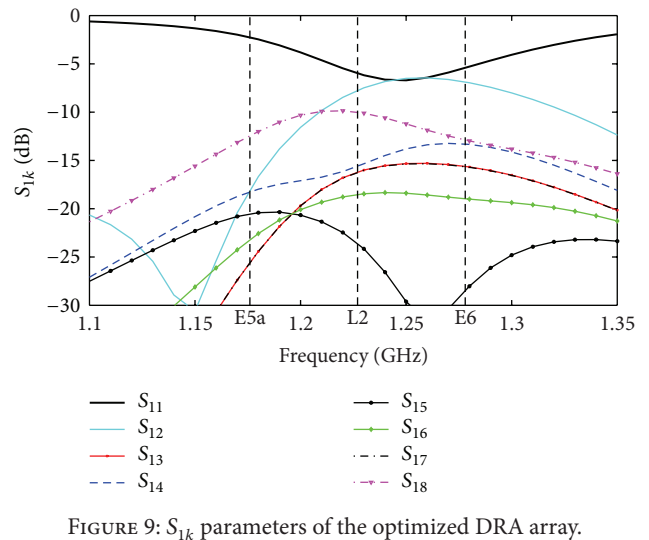


FIGURE 9:  $S_{1k}$  parameters of the optimized DRA array.

A possible solution to the problem is shown in the next subsections.

3.2. *Miniaturized  $2 \times 2$  Array with Metallic Fences.* In order to limit the crosstalk between the different ports of the array, metallic fences (Figure 1(c)) can be used in-between them [22, 23].

The positive effect of fences in reducing mutual coupling can be clearly observed in Figure 9, where  $S$ -parameters for port 1 are shown: all mutual  $S$ -parameters are now below  $-10$  dB, apart from  $S_{12}$ , which is  $\sim -8$  dB at  $L2$  frequency. ( $S_{12}$  expresses the power flow between the two probes of the *same* antenna and therefore does not benefit from the addition of the metallic fences. Actually, the fence has even a detrimental effect for  $S_{12}$ , as it contributes to coupling signal from port 1 to port 2 by mirroring radiated power back towards the antenna itself.)

A substantial decrease in coupling is therefore achieved, which also allows for maximum embedded gain in the bands of interest, as shown in Figure 10. Due to the residual

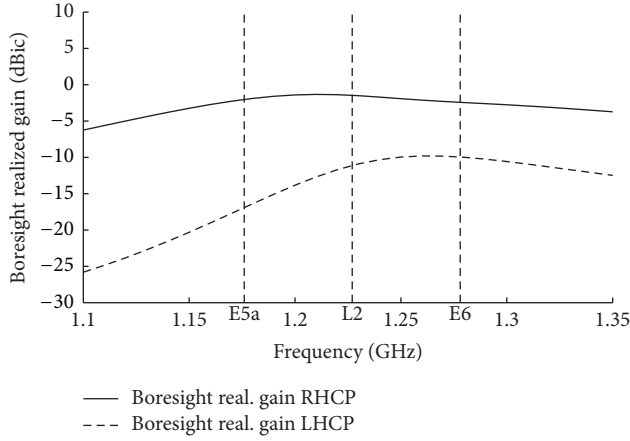


FIGURE 10: Boresight realized gain of the  $2 \times 2$  array of DRAs with fence for the embedded case (only antenna 1 fed).

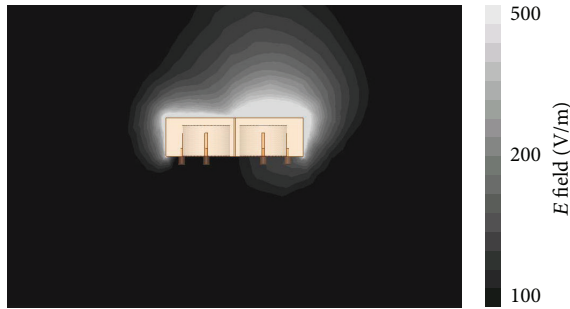


FIGURE 11:  $E$ -field in the  $xz$  plane (vertical plane passing through the fence) for the  $2 \times 2$  array of DRAs with fences when one antenna (on the right of the image) is fed. Strong radiation from the fence, for example, on the left side, is clearly visible.

coupling, the gain is however lower than for the standalone configuration. Moreover, high cross polarization is obtained.

The high cross polarization can be ascribed mostly to the spurious radiation caused by the currents flowing on the upper edges of the metallic fence, whose radiation then interferes with the fields originated from the antenna itself (Figure 11). The metallic fences effectively behave as a near field scatterer and hence diminish the polarization purity of the antenna. In order to limit such effect, an absorber can be used, as shown in the next subsection.

**3.3. Miniaturized  $2 \times 2$  Array with Metallic Fences and Absorber.** In order to limit the spurious radiation due to the fence edges, an absorber material can be placed on top of the fence, with the effect of strongly attenuating the currents radiating from the fence edges.

A flexible rubber based microwave absorber from ARC (UD-11091-7), having a thickness of 5.08 mm, has been used (Figure 12). The absorber protrudes vertically 5 mm from the upper edge of the fences in order to minimize the additional vertical height of the antenna. On the other hand, the depth of the absorber from the fence edges ( $d_{\text{abs}}$  in Figure 12) shall take into account two contrasting requirements: on one

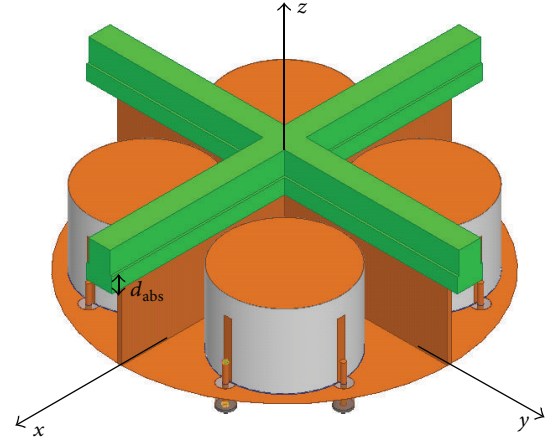


FIGURE 12: 3D view of the  $2 \times 2$  DRA array with fences and absorber mounted on their upper edges.

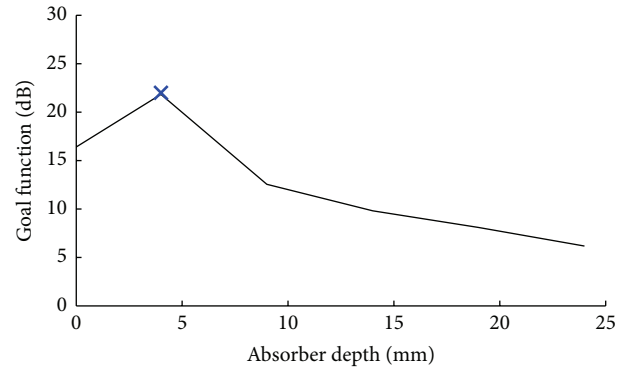


FIGURE 13: Goal function versus absorber depth. The best solution is indicated with the cross ( $w_1 = 0.5$ ,  $w_2 = 0.5$ ).

hand, having an absorber on the whole lateral face of the fence would help in minimizing also the field reflected from the fence and coupled back into the DRA, hence further improving polarization purity; on the other hand, it would also lower the achievable gain, due to the higher energy dissipation in the near field of the antenna.

An optimal result can be found by maximizing the goal function

$$\text{gf} = w_1 G_{R,f_0} + w_2 \text{XPD}_{f_0}, \quad (1)$$

where  $w_1$  and  $w_2$  are weighting coefficients and  $G_{R,f_0}$  is the realized gain at boresight at the center frequency  $f_0 = 1200$  MHz and  $\text{XPD}_{f_0}$  is the cross polarization discrimination in boresight direction at  $f_0$ .

An optimal result is found (blue cross in Figure 13) when the absorber depth is 5 mm from the edge (hence implying a total height of the absorber of 10 mm): for such case, the RHCP gain at  $f_0$  is  $-1.8$  dBic and the  $\text{XPD} = 20$  dB (Figure 14), hence substantially improved with respect to the case with no absorber.

It is worth noticing how the gain, though having a lower peak value, has a broader 3 dB bandwidth in the array configurations, both with and without absorber, with respect

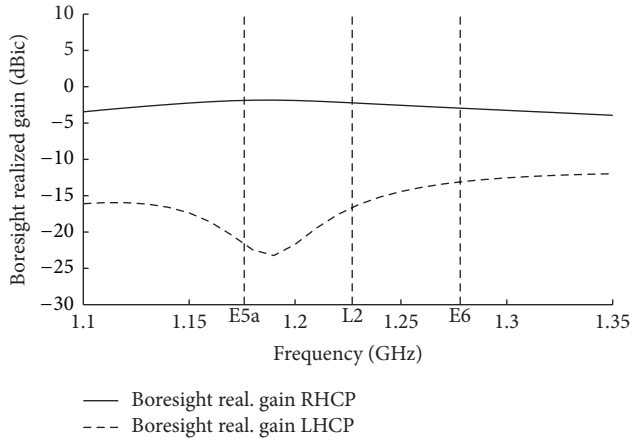


FIGURE 14: Boresight realized gain of the  $2 \times 2$  array of DRAs with fence and absorber for the embedded case (only antenna 1 fed).

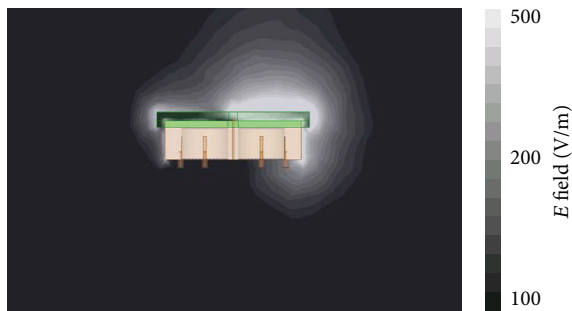


FIGURE 15:  $E$ -field in the  $xz$  plane (vertical plane passing through the fence) for the  $2 \times 2$  array of DRAs with fences and absorber. Only one antenna is fed. A reduced radiation from the fence is now visible.

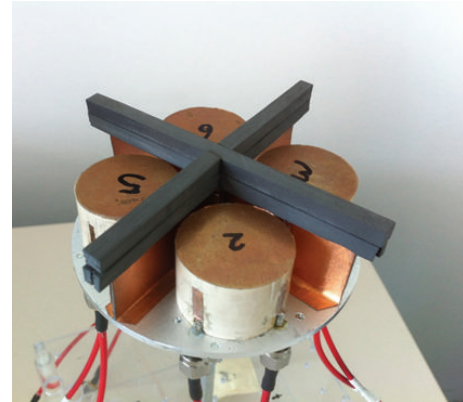
to the single antenna configuration (see, e.g., Figure 20 and Figure 17): this is however a favourable property for our application, as it allows satellite signals received at all bands to have similar power levels, due to the similar antenna gain. Relatively low gain levels are however not too problematic for GNSS applications, as long as the signals can properly be tracked, as is, for instance, the case in mobile phone GNSS antennas, having gains also 15 dB smaller than high-level antennas, due to their extremely small size [24].

In our case, it is therefore more useful to have multiple antennas closely packed together with lower gain, but providing the possibility for beamsteering and nulling, than a single antenna with fixed pattern and higher gain.

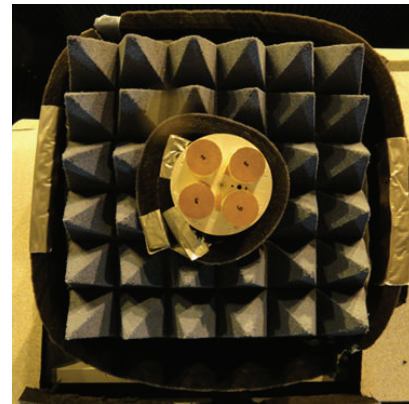
The field radiated by the fence edge is moreover substantially diminished (Figure 15), actively contributing to a better polarization purity. The manufacturing and measurement of the proposed arrays are reported in next section.

#### 4. Measurement

The antennas were manufactured in house. In order to enable an easier manufacturing, the copper strips and cap have been obtained through adhesive copper sheet glued to the surface of the glass ceramic cylinder. The DRA has



(a)



(b)

FIGURE 16: Manufactured array: (a) array with metallic fences and absorber; (b) array without metallic fences, mounted on the movable support of the antenna measurement facility.

then been fixed on the ground plane by means of an RF adhesive tape and the copper strips have been soldered to the inner conductors of SMA connectors. Both the antenna and the arrays (without fences or with fences and absorber) were measured in a near field antenna measurement facility (Satimo StarLab) (Figure 16). External  $90^\circ$  hybrids are used in field measurement to excite circular polarization, that is, to impose a  $90^\circ$  shift between the two orthogonal ports of the antenna.

**4.1. Single Antenna.** The single antenna was measured in the center of a metallic plate with diameter of 3.5 inches (i.e., the same plane size used for the array). The results are shown in Figures 17 and 18, where the measured gain at boresight versus frequency and the  $S$ -parameters are reported.

The measured  $S_{11}$  is slightly worse than the simulated one, most probably due to the nonperfect manufacturing of the strips: improvements are expected if the feeding parts are directly printed on the DRA instead of manually attaching them. The slight mismatch contributes also to a slight degradation of maximum gain, but with an improvement of the bandwidth. Nevertheless, a maximum gain of 3.9 dBic at L2 band is found, quite close to the simulated results.

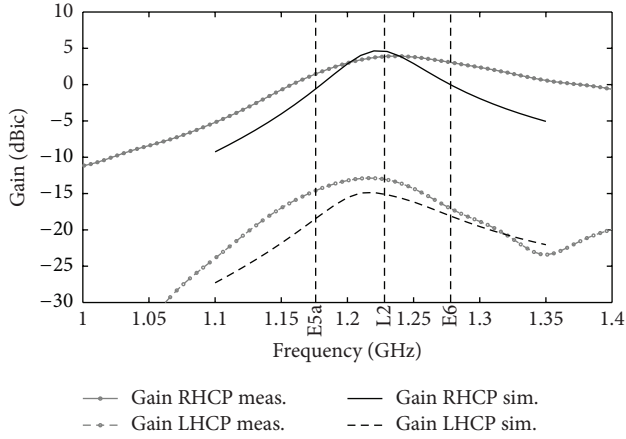


FIGURE 17: Boresight realized gain of the single DRA versus frequency.

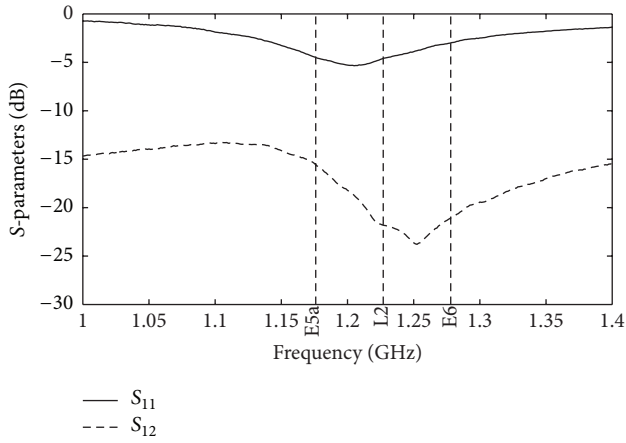


FIGURE 18: Measured S-parameters of the single DRA versus frequency.

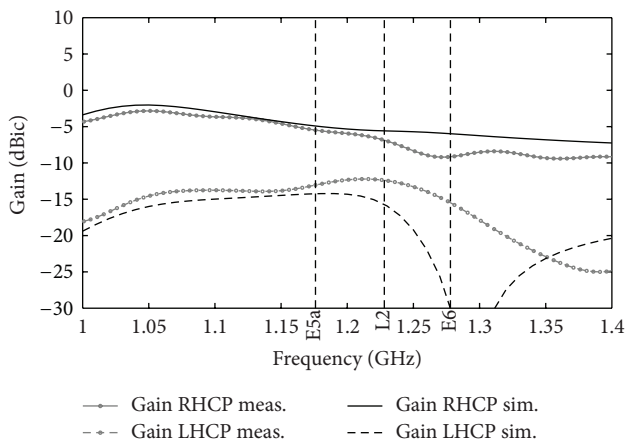


FIGURE 19: Boresight realized gain of the  $2 \times 2$  DRA array versus frequency for the embedded case (one antenna fed).

**4.2. Miniaturized  $2 \times 2$  Array.** The miniaturized  $2 \times 2$  array without fences has then been measured, with gain results as shown in Figure 19. Sequential rotation of the

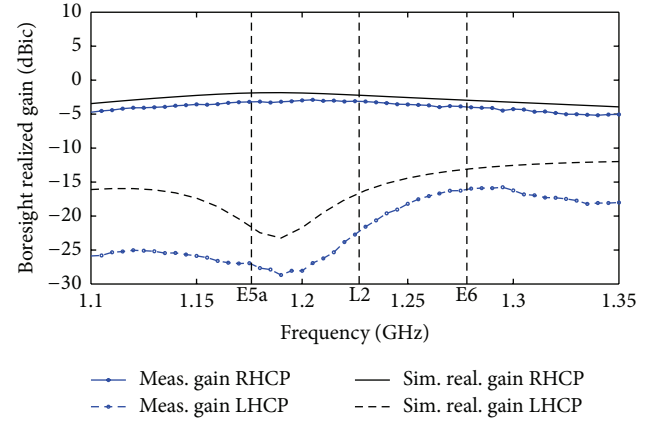


FIGURE 20: Boresight realized gain of the  $2 \times 2$  DRA array with metallic fences and absorber versus frequency (one antenna fed).

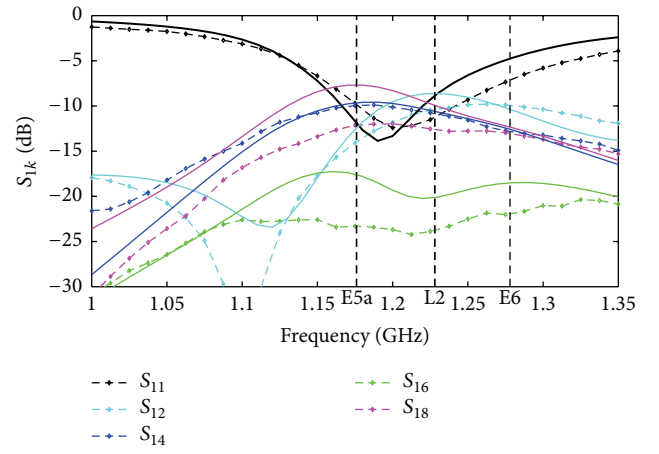


FIGURE 21: S-parameters (both simulated straight lines and measured dashed lines) of the  $2 \times 2$  DRA array with metallic fences and absorber versus frequency (only the most relevant ones are shown for clarity's sake).

excitation between different antennas has been obtained with a commercial 1-to-4 sequential power combiner. As expected from simulation, a strong deterioration is experienced in embedded gain, due to mutual coupling effects. A relevant frequency shift is also clearly distinguishable, inhibiting the use of the array for the bands of interest.

**4.3.  $2 \times 2$  Array with Fences and Absorber.** A cross-like metallic fence (25 mm high and 1 mm thick) with 10 mm absorber (5 above and 5 below the edge) has then been added in-between the antennas in order to reduce mutual coupling, as shown in Section 3.2. The results of the measurements performed with the fence between the antennas are shown in Figures 20–22.

In this case, good agreement between simulation and measurement is found for both S-parameters and gain. For this configuration, optimal matching is obtained at  $f_0 = 1200$  MHz, that is, in the middle of the bands of interest. A gain of  $-3.2$ ,  $-3.1$ , and  $-3.8$  dBic is achieved, respectively, at E5, L2, and E6 central frequencies. Though smaller than the

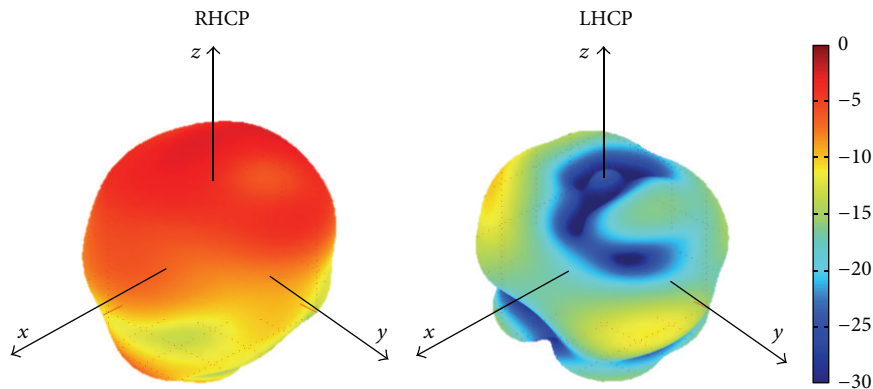


FIGURE 22: 3D embedded pattern for the RHCP and LHCP components of the  $2 \times 2$  array with fences and absorber at  $f_0 = 1200$  MHz.

one of the single antenna configuration, the gain obtained in array configuration is still sufficient for successful satellite tracking and acquisition even when using only one output of the array: however, the use of multiple antennas in such a reduced footprint provides the additional capability of null steering and hence substantially improves robustness against interference with respect to the single antenna case. The 3D embedded pattern is moreover shown in Figure 22, with a clear indication of the almost hemispherical behaviour of the RHCP polarization and reduced cross polarization, hence enabling an optimal use of the array for precise and robust navigation purposes.

## 5. Conclusions

A miniaturized  $2 \times 2$  array, made of dielectric resonator antennas, for robust GNSS navigation at E5/L2/E6 band has been shown. The use of a high DK material enables good miniaturization, helping to pack the  $2 \times 2$  array in a footprint of  $3.5''$  ( $=89$  mm) and hence making it suitable for mobile applications, for instance, in airplanes or cars. Metallic fences and a planar absorber are used to decrease mutual coupling due to the close vicinity of the antennas, hence managing to obtain strong cross polarization discrimination and reduced cross talk between the antennas and therefore promising optimal behaviour as miniaturized array for interference suppression in robust navigation applications.

## Competing Interests

The authors declare that they have no competing interests.

## Acknowledgments

The authors wish to thank Dr. M. Letz from Schott ag for valuable support with the dielectric material, Mr. L. Mair from Telemeter Electronic GmbH for providing the absorber, and B. Gabler for his help in measurement.

## References

- [1] D. Borio, C. O'Driscoll, and J. Fortuny, "Jammer impact on Galileo and GPS receivers," in *Proceedings of the International Conference on Localization and GNSS (ICL-GNSS '13)*, pp. 1–6, IEEE, Turin, Italy, June 2013.
- [2] J. A. Larcom and H. Liu, "Modeling and characterization of GPS spoofing," in *Proceedings of the 13th IEEE International Conference on Technologies for Homeland Security (HST '13)*, pp. 729–734, Waltham, Mass, USA, November 2013.
- [3] M. V. T. Heckler, M. Cuntz, A. Konovaltsev, L. A. Greda, A. Dreher, and M. Meurer, "Development of robust safety-of-life navigation receivers," *IEEE Transactions on Microwave Theory and Techniques*, vol. 59, no. 4, pp. 998–1005, 2011.
- [4] ARINC 743 Specification, <http://www.aviation-ia.com>.
- [5] C. Fernández-Prades, L. L. Presti, and E. Falletti, "Satellite radiolocalization from GPS to GNSS and beyond: novel technologies and applications for civil mass market," *Proceedings of the IEEE*, vol. 99, no. 11, pp. 1882–1904, 2011.
- [6] A. Konovaltsev, D. S. De Lorenzo, A. Hornbostel, and P. Enge, "Mitigation of continuous and pulsed radio interference with GNSS antenna arrays," in *Proceedings of the 21st International Technical Meeting of the Satellite Division of The Institute of Navigation (ION GNSS '08)*, Savannah, Ga, USA, September 2008.
- [7] M. G. Amin and W. Sun, "A novel interference suppression scheme for global navigation satellite systems using antenna array," *IEEE Journal on Selected Areas in Communications*, vol. 23, no. 5, pp. 999–1012, 2005.
- [8] R. L. Fante and J. J. Vaccaro, "Wideband cancellation of interference in a GPS receive array," *IEEE Transactions on Aerospace and Electronic Systems*, vol. 36, no. 2, pp. 549–564, 2000.
- [9] I. J. Gupta, T.-H. Iee, K. A. Griffith et al., "Non-planar adaptive antenna arrays for GPS receivers," *IEEE Antennas and Propagation Magazine*, vol. 52, no. 5, pp. 35–51, 2010.
- [10] J. R. Lambert, C. A. Balanis, and D. DeCarlo, "Spherical cap adaptive antennas for GPS," *IEEE Transactions on Antennas and Propagation*, vol. 57, no. 2, pp. 406–413, 2009.
- [11] K. Yinusa, W. Elmarissi, S. Caizzzone, and A. Dreher, "A multi-band conformal antenna array for GNSS applications," in *Proceedings of the IEEE Antennas and Propagation Symposium (APS '16)*, Fajardo, Puerto Rico, USA, June–July 2016.
- [12] N. Basta, A. Dreher, S. Caizzzone et al., "System concept of a compact multi-antenna GNSS receiver," in *Proceedings of the 7th German Microwave Conference (GeMiC '12)*, Ilmenau, Germany, March 2012.

- [13] M. Chen and C.-C. Chen, "A compact dual-band GPS antenna design," *IEEE Antennas and Wireless Propagation Letters*, vol. 12, pp. 245–248, 2013.
- [14] J. Volakis, C.-C. Chen, and K. Fujimoto, *Small Antennas: Miniaturization Techniques and Applications*, McGraw-Hill, 2010.
- [15] X. Ren, X. Chen, and K. Huang, "A novel electrically small meandered line antenna with a trident-shaped feeding strip for wireless applications," *International Journal of Antennas and Propagation*, vol. 2012, Article ID 757429, 7 pages, 2012.
- [16] M. S. Alam, N. Misran, B. Yatim, and M. T. Islam, "Development of electromagnetic band gap structures in the perspective of microstrip antenna design," *International Journal of Antennas and Propagation*, vol. 2013, Article ID 507158, 22 pages, 2013.
- [17] A. Sharma and S. C. Shrivastava, "Analysis of resonant frequency and quality factor of dielectric resonator at different dielectric constant materials," in *Proceedings of the International Conference of Recent Advances in Microwave Theory and Applications (MICROWAVE '08)*, pp. 593–595, IEEE, Jaipur, India, November 2008.
- [18] A. Petosa and A. Ittipiboon, "Dielectric resonator antennas: a historical review and the current state of the art," *IEEE Antennas and Propagation Magazine*, vol. 52, no. 5, pp. 91–116, 2010.
- [19] Q. Lai, G. Almpanis, C. Fumeaux, H. Benedickter, and R. Vahldieck, "Comparison of the radiation efficiency for the dielectric resonator antenna and the microstrip antenna at Ka band," *IEEE Transactions on Antennas and Propagation*, vol. 56, no. 11, pp. 3589–3592, 2008.
- [20] D. Mitra, S. M. Haque, and B. Ghosh, "Metal loaded miniaturized CPW fed DRA," in *Proceedings of the Applied Electromagnetics Conference (AEMC '09)*, Kolkata, India, December 2009.
- [21] Z.-N. Chen, K.-W. Leung, K.-M. Luk, and E. K.-N. Yung, "Effect of parasitic disk on a coaxial probe-fed dielectric resonator antenna," *Microwave and Optical Technology Letters*, vol. 15, no. 3, pp. 166–168, 1997.
- [22] S. Caizzone, "Miniaturized E5a/E1 antenna array for robust GNSS navigation," *IEEE Antennas and Wireless Propagation Letters*, 2016.
- [23] S. Caizzone and A. Dreher, "Miniaturized DRA array for GNSS applications," in *Proceedings of the 9th European Conference on Antennas and Propagation (EuCAP '15)*, pp. 1–2, Lisbon, Portugal, May 2015.
- [24] K. M. Pesyna, R. W. Heath, and T. E. Humphreys, "Centimeter positioning with a smartphone-quality GNSS antenna," in *Proceedings of the 27th International Technical Meeting of the Satellite Division of the Institute of Navigation (ION GNSS '14)*, Tampa, Fla, USA, September 2014.

## Research Article

# Design of a Compact Quad-Band Slot Antenna for Integrated Mobile Devices

Jian Dong, Xiaping Yu, and Guoqiang Hu

*School of Information Science and Engineering, Central South University, Changsha 410083, China*

Correspondence should be addressed to Jian Dong; [dongjian@csu.edu.cn](mailto:dongjian@csu.edu.cn)

Received 9 February 2016; Revised 2 June 2016; Accepted 9 June 2016

Academic Editor: Wenhua Yu

Copyright © 2016 Jian Dong et al. This is an open access article distributed under the Creative Commons Attribution License, which permits unrestricted use, distribution, and reproduction in any medium, provided the original work is properly cited.

In order to incorporate different communication standards into a single device, a compact quad-band slot antenna is proposed in this paper. The proposed antenna is composed of a dielectric substrate, T-shaped microstrip patch with a circle slot and an inverted L-slot, and a comb-shaped ground on the back of the substrate. By adopting these structures, it can produce four different bands, while maintaining a small size and a simple structure. Furthermore, a prototype of the quad-band antenna is designed and fabricated. The simulated and measured results show that the proposed antenna can operate over the 1.79–2.63 GHz, 3.46–3.97 GHz, 4.92–5.85 GHz, and 7.87–8.40 GHz, which can cover entire PCS (Personal Communications Service, 1.85–1.99 GHz), UMTS (Universal Mobile Telecommunications System, 1.92–2.17 GHz), WCDMA (wideband code-division multiple access, 2.1 GHz), Bluetooth (2.4–2.48 GHz), WiBro (Wireless Broad band access service, 2.3–3.39 GHz), WLAN (Wireless Local Area Networks, 2.4/5.2/5.8 GHz), WiMAX (Worldwide Interoperability for Microwave Access, 2.5/3.5/5.5 GHz), and X-band SATcom applications (7.9–8.4 GHz). The proposed antenna is particularly attractive for mobile devices integrating multiple communication systems.

## 1. Introduction

Modern wireless communication devices are often required to integrate multiple standards and services, operating at different frequency bands, into a single portable handset [1]. Thus, it is highly desirable to design multiband antennas to meet the needs of multiple communication standards. For PCS, UMTS, and WCDMA operations, the ideal frequency bands are 1.9 GHz and 2.1 GHz in a single antenna. As for WLAN/WiMAX applications, the operating bands assigned by IEEE 802.11 are 2.4 GHz (2.4–2.484 GHz), 5.2/5.8 GHz (5.15–5.35 GHz/5.725–5.825 GHz), and 2.5/3.5/5.5 GHz (2.5–2.69/3.4–3.69/5.25–5.85 GHz). Many antennas have been recently reported in the literature to cover such applications, but most of them are single-band or dual-band [2–4]. Obviously, few bands limit their applications. Thus, some designs were proposed to operate covering triband applications [5, 6]. In [5], a symmetrical L-slot antenna was designed covering 2.34–2.82 GHz, 3.16–4.06 GHz, and 4.69–5.37 GHz. A triband microstrip slot antenna for WLAN/WiMAX application was presented in [6]. The common problem is that these designs can only cover more than 2.3 GHz frequency

applications, but lower frequency band applications are not involved, such as PCS (1.9 GHz) and WCDMA (2.1 GHz). Furthermore, many antennas have large size and complex structure which are not suitable for space-constrained portable wireless terminals. In [7], an antenna with I-shaped monopole was printed in the area of 28 mm × 29 mm. A multiband antenna with H-shaped slot was presented in [8] with the area of 60 mm × 60 mm. A multiband internal antenna for all commercial mobile communication bands and 802.11a/b/g/n WLAN was designed in [9] with the area of 40 mm × 20 mm. In [10], a small CPW- (coplanar-waveguide-) fed multiband antenna consisting of a square-spiral patch with two L-shape strips was reported. However, the coverage of WiMAX/WLAN applications in [9, 10] is not complete. In [11], a compact antenna with symmetrical L-strips was reported for WLAN/WiMAX operations; however, the three resonant frequencies cannot be adjusted independently. A CPW-fed monopole antenna was proposed in [12], which covers lots of applications but all are below 3 GHz frequency.

In this paper, a compact quad-band antenna with a circle slot and an inverted L-slot on the radiating patch as well as a comb-shaped ground structure is proposed not only to obtain

TABLE 1: Performance comparison of the proposed antenna with other reported antennas.

Reference	Size	Operating bands (GHz)	Peak gain (dBi)	Remarks
[2]	$60 \times 12$	0.9–1.9	5.2	Few useful frequency bands or too large overall size
[3]	$40 \times 35$	2.26–2.42, 3.29–3.6	3.3	
[4]	$40 \times 10$	2.38–2.52, 3.40–3.62	2.7	Few useful frequency bands
[5]	$23 \times 36.5$	2.33–2.76, 3.05–3.88, 5.57–5.88	3.0	Only >2.3 GHz applications
[6]	$38 \times 25$	2.4–2.7, 3.1–4.15, 4.93–5.89	2.9	
[7]	$29 \times 28$	0.79–0.92, 1.71–2.28	3.25	Few useful frequency bands
[8]	$60 \times 60$	1.55–1.57, 2.395–2.695, 4.975–5.935	3.7	Too large overall size
[9]	$40 \times 20$	0.82–2.69, 5.15–5.825	3.5	Incomplete coverage of WIMAX/WLAN applications
[10]	$20 \times 20$	2.33–2.809, 3.36–3.54, 5.811–5.987, 7.994–8.486	Not mentioned	
[11]	$32 \times 28$	2.34–2.82, 3.16–4.06, 4.69–5.37	3.18	Nonindependently tuned resonant frequencies
[12]	$67 \times 38$	0.863–1.049, 1.49–2.81	Not mentioned	Only <3 GHz applications
Proposed antenna	$20 \times 30$	1.79–2.63, 3.49–3.97, 4.92–5.85, 7.87–8.40	6.9	Compact size and sufficient bands

good quad-band operational performance but also to achieve a smaller size and simpler structure with respect to the previous designs. By combining different resonant structures, the proposed antenna can generate four resonant modes to cater for the desired bands of PCS, WCDMA, UMTS, Bluetooth, WLAN, WiMAX, and X-band applications. It is evident from Table 1 that the proposed antenna has more a compact size and more sufficient frequency bands as compared to the other mentioned antennas. Details of antenna design and simulated and measured results will be carefully examined and discussed in the following sections.

## 2. Antenna Design

A schematic view of the proposed slot microstrip-fed planar antenna for quad-band application is shown in Figure 1. The antenna is printed on a 1.6 mm thick FR4 substrates with relative permittivity of 4.4 and loss tangent 0.02, while the overall areas are only  $20 \times 30 \text{ mm}^2$ . In order to miniaturize the size of the portable devices antenna, the radiator width is set to be the same as the width of the microstrip feed line. The proposed antenna consists of a T-shaped radiating patch and a comb-shaped ground. There is a circular slot (Radius  $R_1$ ) on the broad rectangle of the T-shaped patch and an inverted L-shaped slot of length  $L_{c1}$  and width  $W_{c1}$  on the narrow rectangle of the T-shaped patch. The conventional rectangle ground is transformed into a comb-shaped ground structure by cutting rectangular slots to excite 2.4/5.5 GHz applications. In order to achieve  $50 \Omega$  characteristic impedance, the antenna is fed with a 2.8 mm wide microstrip line. The final antenna design is achieved by tuning the length, width, and the slot dimensions of the radiating patch and the comb-shaped ground structure. All the parameters are optimized with Ansoft HFSS and summarized in Table 2. Detailed

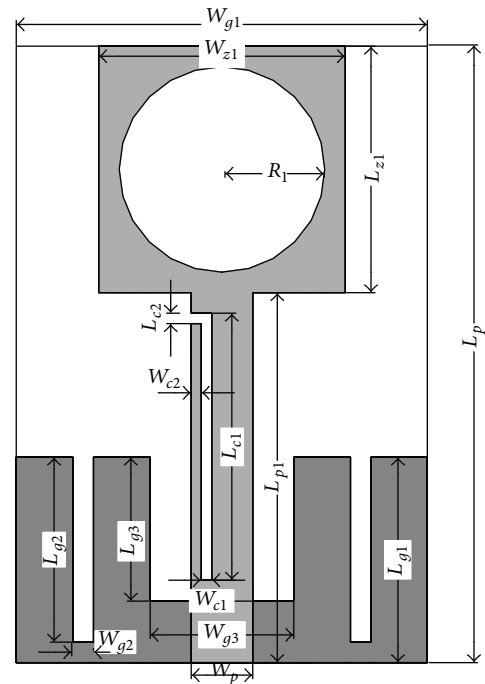


FIGURE 1: Geometry of the proposed quad-band slot antenna.

analysis of the proposed antenna will be given from the following three aspects.

*2.1. Design Principle.* Etching slots is one of the most efficient techniques in multiband antenna miniaturization. For a given shape and size of the radiating patch (or the ground plane), cutting slots on it will change the surface current distribution and increase the effective current path length (see

TABLE 2: Parameters of the proposed antenna (unit: mm).

$W_{g1}$	$L_{g1}$	$L_p$	$L_{p1}$	$W_p$	$W_{z1}$	$L_{z1}$	$L_{g2}$
20	12	30	18	2.8	12	12	9
$W_{g2}$	$L_{g3}$	$W_{g3}$	$L_{c1}$	$W_{c1}$	$L_{c2}$	$W_{c2}$	$R_1$
1	7	7.3	13.4	0.5	0.5	0.5	4.8

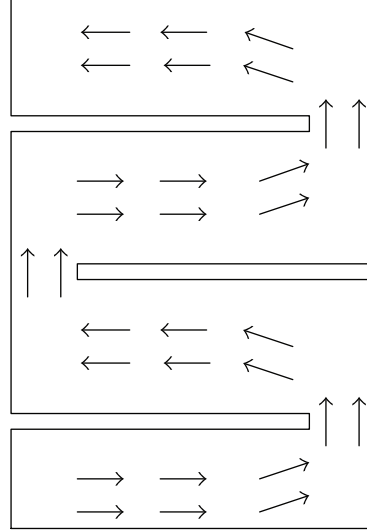


FIGURE 2: Schematic diagram of surface current distribution on rectangular patch with slots.

in Figure 2). Therefore, the resonant frequency will drop significantly. Similarly, for a given resonant frequency, the size of the antenna will be significantly reduced by cutting slots on the radiating patch or on the ground plane. Also, the bandwidth of the antenna will be broadened because of the decreased Q value resulting from etching slots.

In our proposed antenna, the T-shaped radiating patch and the rectangular ground act as wideband impedance matching. Note that the effective length of the slots,  $L$ , can be approximately calculated by [13]

$$L = \frac{c}{4f_0\sqrt{\epsilon_e}}, \quad (1)$$

where  $f_0$  is the resonance frequency,  $c$  stands for the free-space velocity of light,  $\epsilon_e = (\epsilon_r + 1)/2$  is the effective permittivity of the dielectric substrate, and  $\epsilon_r$  is the relative permittivity. Assuming that the antenna works at 3.5 GHz, the inverted L slot length is about 13 mm. Also, the lengths of the other slots can be estimated in the similar way.

**2.2. Structural Analysis.** Figure 3 shows the evolution of the proposed antenna and its corresponding simulated results of return loss. It begins from the design of Antenna (1), which consists of a T-shaped radiation patch (having no slots) and a comb-shaped ground structure. This simple design can obtain two wide bands of 1.92–3.09 GHz and 4.77–6.81 GHz as shown in Figure 3(b), which cover the WLAN/WiMAX standard applications. In order to excite 3.5 GHz resonant mode, an inverted L-slot on the narrow rectangle of the T-shaped radiation patch is introduced in Antenna (2). The

corresponding  $-10$  dB return loss bandwidth is 580 MHz (3.37–3.95 GHz) as shown in Figure 3(b). Finally, in order to generate the high frequency band, a circular slot is designed on the broad rectangle of the T-shaped patch in Antenna (3). The circular slot can independently yield a resonance operating at 8 GHz band.

In order to further explain the quad-band operation property of the proposed antenna, the surface current distributions of the whole antenna at the frequencies of 2.5, 3.5, 5.5, and 8 GHz are given in Figure 4. It can be clearly seen from the figure that the current distributions are different in the four bands. In particular, when the antenna operates at 3.5 GHz, as shown in Figure 4(b), most of the currents are concentrated near the inverted L-shaped slot. As shown in Figure 4(a), the rectangular slot in the middle of the comb-shaped ground with radiation patch produces 2.4 GHz frequency band. As shown in Figure 4(c), the symmetrical rectangular slots on the comb-shaped ground with radiation patch produce 5.5 GHz frequency band. When the antenna works at 8 GHz frequency, as shown in Figure 4(d), currents are mainly distributed near the circular slot on the patch.

**2.3. Parametric Study.** To illustrate the effects of the critical parameters on the four different frequency bands (i.e., band I-2.4 GHz, band II-3.5 GHz, band III-5.5 GHz, and band IV-8 GHz), a parametric study on the quad-band antenna is carried out. From the parametric study, the optimum value for each parameter of the proposed antenna is obtained as listed in Table 2. Note that the presented antenna is sensitive to the geometrical parameters due to the miniaturized size.

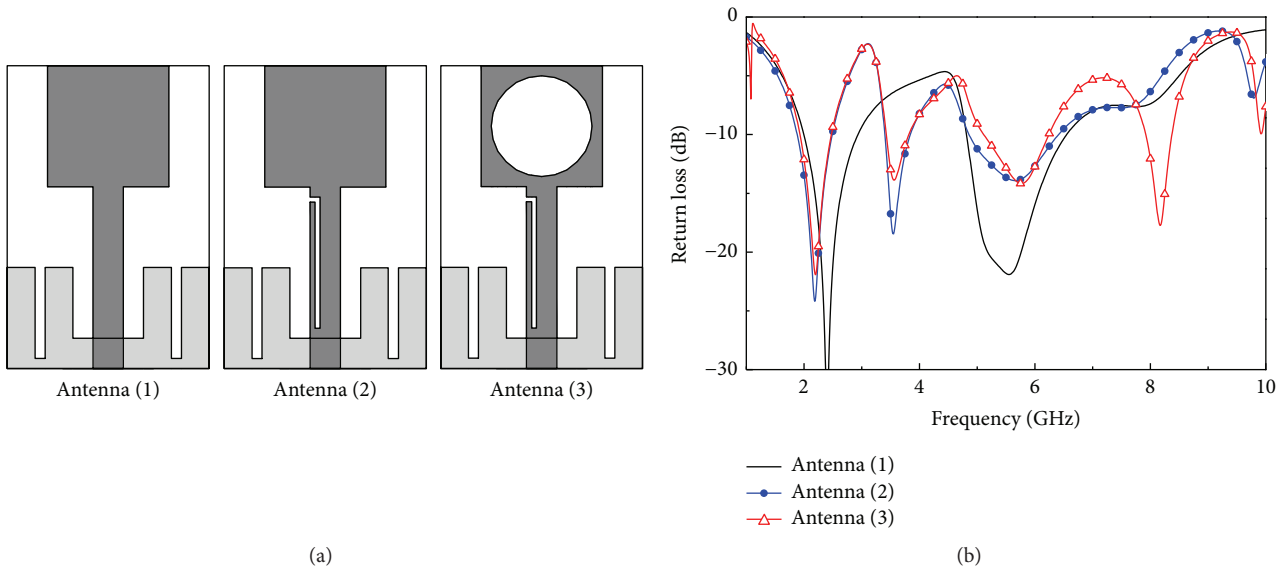


FIGURE 3: (a) Geometries of various antennas involved in the design evolution process. (b) Simulated return loss for the various antenna geometries.

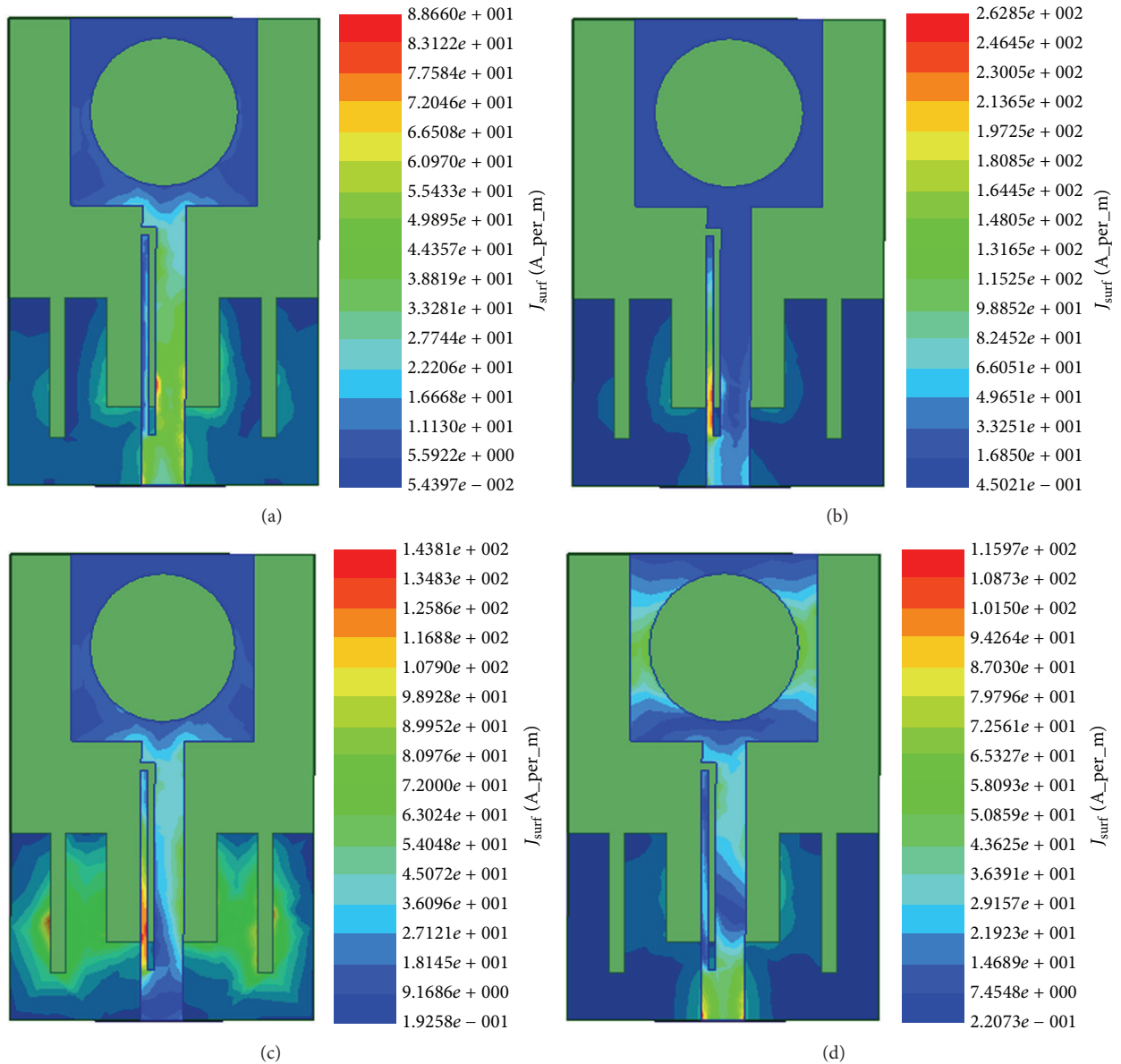


FIGURE 4: Surface current distributions of the proposed antenna at (a) 2.5, (b) 3.5, (c) 5.5, and (d) 8 GHz.

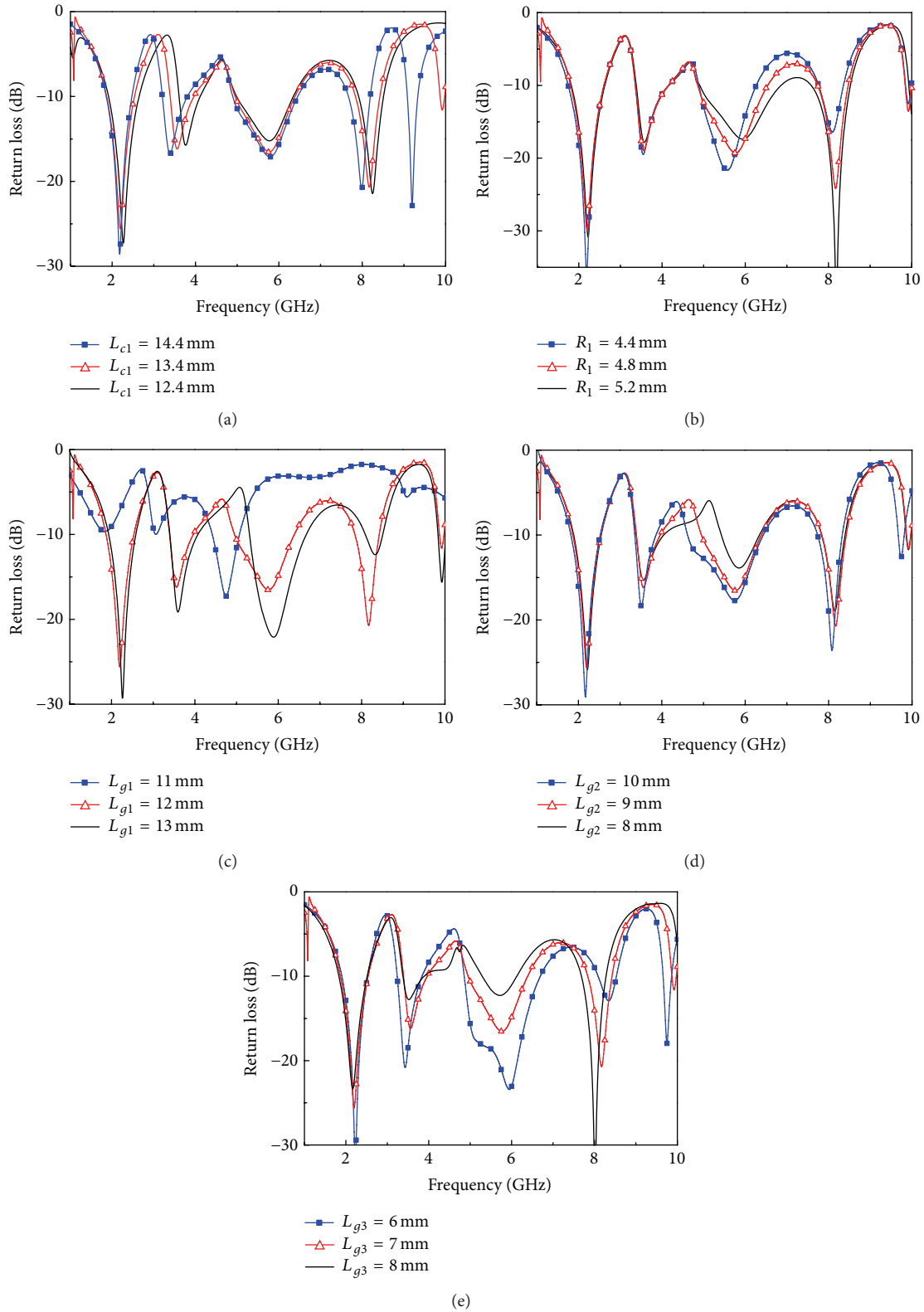


FIGURE 5: Simulated return loss of the antenna (a) as a function of  $L_{c1}$ , the length of the inverted L-slot, (b) as a function of  $R_1$ , the radius of the circle slot, (c) as a function of  $L_{g1}$ , the height of the comb-shaped ground, (d) as a function of  $L_{g2}$ , the length of the symmetrical rectangular slots on the ground, and (e) as a function of  $L_{g3}$ , the length of the middle rectangular slot on the ground; other parameters are the same as given in Table 2.

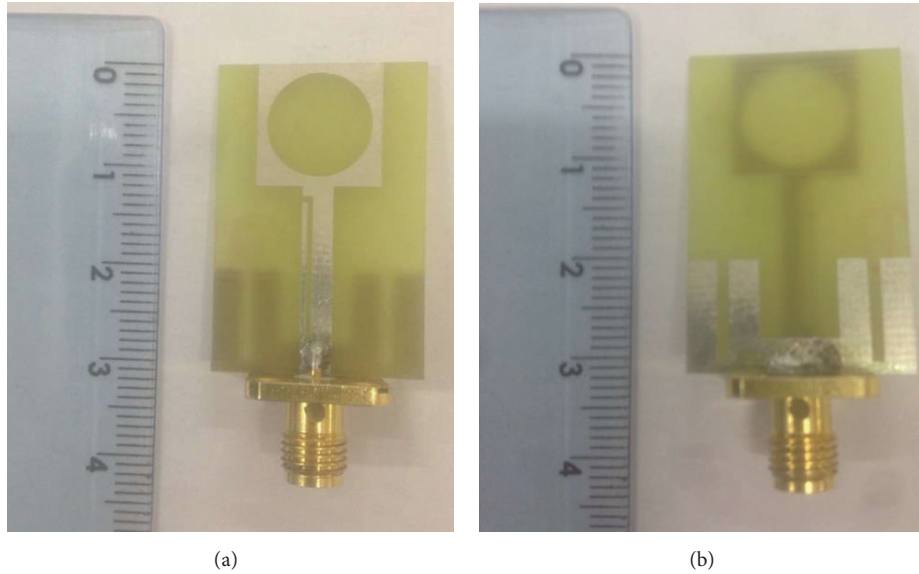


FIGURE 6: Fabricated prototype. (a) Top view. (b) Bottom view.

The dimensions of patch or ground slot are critical parameters in determining the sensitivity of impedance matching.

**2.3.1. Variation of Patch Parameters.** Keeping all the other parameters invariant, the effect of  $L_{c1}$  and the length of the inverted L-slot, on the return loss is depicted in Figure 5(a). It is observed from Figure 5(a) that the frequency bands shift toward lower frequency as  $L_{c1}$  is increased from 12.4 mm to 14.4 mm. All the three curves cover bands I and III applications, but the curve of 12.4 mm cannot cover band II completely and the result of 14.4 mm cannot cover band IV completely. Thus, the value of  $L_{c1}$  is chosen 13.4 mm as an optimum. The effect of the radius of the circle slot,  $R_1$ , on the return loss is depicted in Figure 5(b). It can be observed from simulation results that as the values of  $R_1$  increase from 4.4 mm to 5.2 mm, the frequency bands shift toward higher frequency. It is also found that  $R_1$  mainly affects bands III and IV while bands I and II almost remain unchanged. Combining the coverage of bands III and IV, the value of  $R_1 = 4.8$  mm is chosen as an optimum.

**2.3.2. Variation of Ground Parameters.** The height of the comb-shaped ground,  $L_{g1}$ , on the return loss is depicted in Figure 5(c). It is shown when the value of  $L_{g1}$  is reduced to 11 mm, the return loss has obvious degradation and only one resonant band is formed. Furthermore, at the value equal to 13 mm, the antenna cannot cover bands III and IV completely. Thus, the optimum value for  $L_{g1}$  is chosen as 12 mm.

The effect of the length of the symmetrical rectangular slots on the ground,  $L_{g2}$ , on the return loss is depicted in Figure 5(d). It is shown from Figure 5(d) that as  $L_{g2}$  is increased from 8 mm to 10 mm, the impedance bandwidth of band III is increased while other bands almost remain unchanged. Similar conclusion can be drawn from Figure 5(e)

as the length of the middle rectangular slot on the ground,  $L_{g3}$ , is reduced from 8 mm to 6 mm. It is also found that  $L_{g3}$  slightly affects bands II and IV, but this effect can be adjusted back using other aforesaid parameters.

### 3. Experimental Results and Discussion

Based on the optimal dimensions listed in Table 2, a prototype of the quad-band antenna is fabricated and experimentally investigated. Figure 6 shows a photograph of the fabricated antenna. The simulated and measured results for the return loss of the proposed antenna are shown in Figure 7. The simulated  $-10$  dB bandwidths range from 1.87 to 2.53 GHz, from 3.39 to 3.96 GHz, from 4.95 to 6.38 GHz, and from 7.84 to 8.42 GHz, and the measured bandwidths range from 1.79 to 2.63 GHz, from 3.46 to 3.97 GHz, from 4.92 to 5.85 GHz, and from 7.87 to 8.40 GHz. The discrepancy between the simulated and measured results could be mainly due to errors in processing and effect of the SMA connector. It can be concluded from return loss results that the proposed design has a good quad-band property which evidently covers entire PCS, WCDMA, WLAN, WiMAX, and X-band SATcom applications.

The gain values of the antenna with the frequency are shown in Figure 8. The average gains through all the four bands vary from 2.5 dB to 6.9 dB, showing that the antenna can provide stable gains in the four working frequency bands. The efficiency variations within different frequency bands are shown in Figure 9. It is observed from Figure 9 that the radiation efficiency of the antenna varies from 54% to 86.3%.

Figure 10 shows the simulated and measured far-field radiation patterns in  $xoz$  plane (E-plane) and  $xoy$  plane (H-plane) for frequencies at 2.5, 3.5, 5.5, and 8 GHz, respectively.

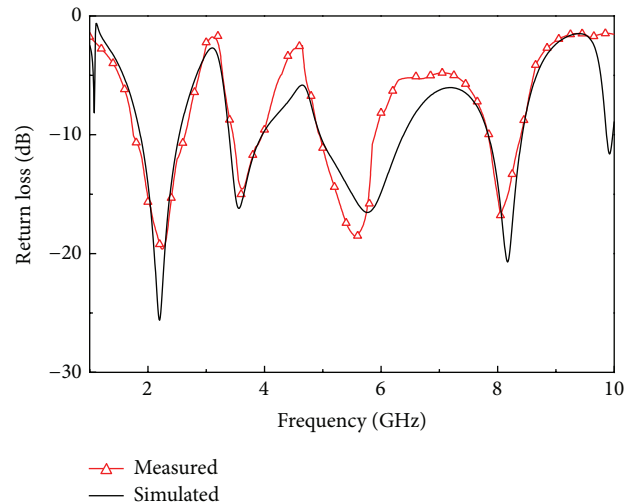


FIGURE 7: Simulated and measured results of the return loss of the proposed quad-band antenna.

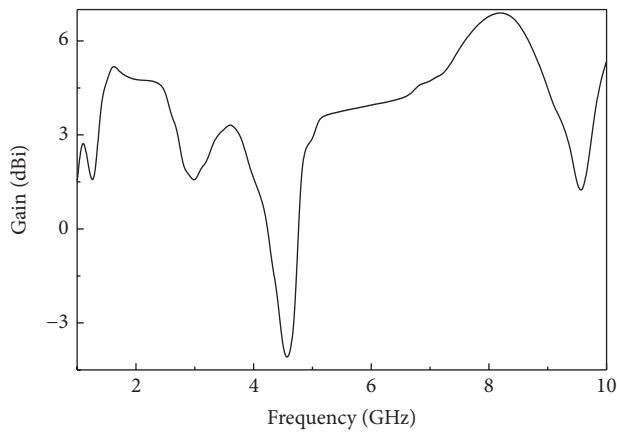


FIGURE 8: Gains of the proposed compact quad-band antenna.

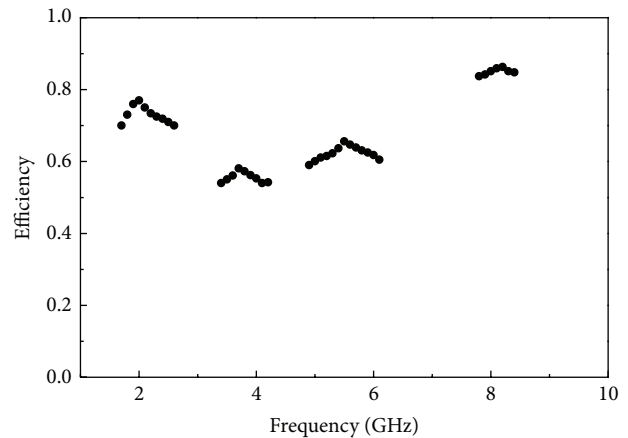


FIGURE 9: Efficiency variations within different frequency bands.

From the figure, we can conclude that the proposed antenna features fairly good omnidirectional H-plane patterns and bidirectional E-plane patterns over the desired operating bands. Radiation characteristics have obvious advantages over other similar multiband antennas; for example, in [8, 14], there are some sidelobes (especially at relatively high frequency band) in the radiation patterns which degrade the antenna radiation performance. The above radiation characteristics show that the proposed antenna is much preferable for the quad-band applications in the terminal design of integrated wireless communication systems.

#### 4. Conclusion

A compact quad-band antenna with a circle slot and an inverted L-slot on the T-shaped radiating patch as well as a comb-shaped ground structure is proposed in this paper for incorporating different communication standards in a single device. The measured return loss indicates that the proposed antenna can operate over the bands of 1.79–2.63 GHz, 3.46–3.97 GHz, 4.92–5.85 GHz, and 7.87–8.40 GHz, which comply

with the frequency needs of PCS, UMTS, WCDMA, Bluetooth, WLAN, WiMAX, and X-band uplink SATcom applications. The antenna exhibits a low profile, a compact size with simple structure, and largely omnidirectional radiation patterns. Since the antenna can be easily integrated with the circuit board and the handset enclosure, it is particularly attractive for portable devices incorporating multiple communication systems.

#### Competing Interests

The authors declare that there are no competing interests regarding the publication of this paper.

#### Acknowledgments

This work was supported in part by the National Science Foundation of China under Grant no. 61201086, in part by the China Scholarship Council under Grant no. 201506375060, in part by the Planned Science and Technology Project of

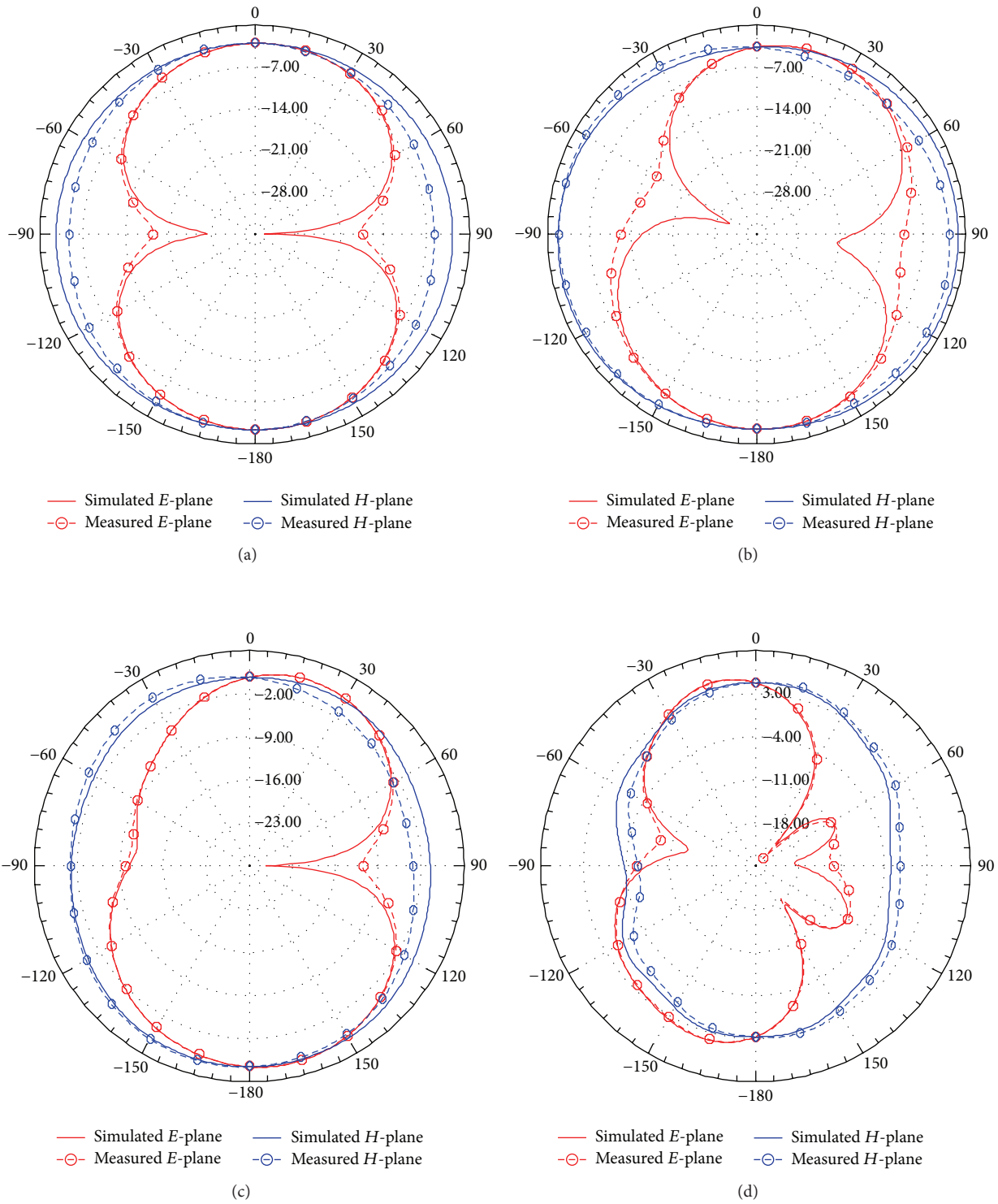


FIGURE 10: Simulated and measured radiation patterns at (a) 2.5 GHz, (b) 3.5 GHz, (c) 5.5 GHz, and (d) 8 GHz resonance frequencies.

Guangdong Province under Grant no. 2013B090500007, in part by the Dongguan Project on the Integration of Industry, Education, and Research under Grant no. 2014509102205, and in part by the Fundamental Research Funds for the Central Universities of Central South University under Grant no. 2016zzts340.

## References

- [1] J. F. V. Valdes, S. Burgos, A. M. Acevedo, and P. Padilla, "Antenna measurement systems and antenna technology for next wireless generation," *International Journal of Antennas and Propagation*, vol. 2013, Article ID 527582, 2 pages, 2013.
- [2] K.-L. Wong and L.-C. Lee, "Multiband printed monopole slot antenna for WWAN operation in the laptop computer," *IEEE Transactions on Antennas and Propagation*, vol. 57, no. 2, pp. 324–330, 2009.
- [3] X. L. Sun, S. W. Cheung, and T. I. Yuk, "Dual-band monopole antenna with compact radiator for 2.4/3.5 GHz WiMAX applications," *Microwave and Optical Technology Letters*, vol. 55, no. 8, pp. 1765–1770, 2013.
- [4] J. Malik, A. Patnaik, and M. V. Kartikeyan, "A compact dual-band antenna with omnidirectional radiation pattern," *IEEE Antennas and Wireless Propagation Letters*, vol. 14, pp. 503–506, 2015.
- [5] P. Liu, Y. Zou, B. Xie, X. Liu, and B. Sun, "Compact CPW-fed tri-band printed antenna with meandering split-ring slot for WLAN/WiMAX applications," *IEEE Antennas and Wireless Propagation Letters*, vol. 11, pp. 1242–1244, 2012.
- [6] J. Pei, A.-G. Wang, S. Gao, and W. Leng, "Miniaturized triple-band antenna with a defected ground plane for WLAN/WiMAX applications," *IEEE Antennas and Wireless Propagation Letters*, vol. 10, pp. 298–301, 2011.
- [7] Y. Jee and Y.-M. Seo, "Triple-band CPW-fed compact monopole antennas for GSM/PCS/DCS/WCDMA applications," *Electronics Letters*, vol. 45, no. 9, pp. 446–448, 2009.
- [8] T.-H. Chang and J.-F. Kiang, "Compact multi-band H-shaped slot antenna," *IEEE Transactions on Antennas and Propagation*, vol. 61, no. 8, pp. 4345–4349, 2013.
- [9] M. Kim, W. Lee, and Y. J. Yoon, "A multi-band internal antenna for all commercial mobile communication bands and 802.11a/b/g/n WLAN," in *Proceedings of the Asia-Pacific Microwave Conference (APMC '11)*, pp. 171–174, Melbourne, Australia, December 2011.
- [10] P. Beigi, J. Nourinia, Y. Zehforoosh, and B. Mohammadi, "A compact novel CPW-FED antenna with square spiral-patch for multiband applications," *Microwave and Optical Technology Letters*, vol. 57, no. 1, pp. 111–115, 2015.
- [11] W. Hu, Y.-Z. Yin, P. Fei, and X. Yang, "Compact triband square-slot antenna with symmetrical L-strips for WLAN/WiMAX applications," *IEEE Antennas and Wireless Propagation Letters*, vol. 10, pp. 462–465, 2011.
- [12] D.-H. Hsieh, J.-W. Wu, Y.-W. Cheng, and C.-J. Wang, "A CPW-fed meandered-shaped monopole antenna with asymmetrical ground planes," in *Proceedings of the IEEE Radio and Wireless Symposium (RWS '15)*, pp. 86–88, IEEE, San Diego, Calif, USA, January 2015.
- [13] Y. F. Cao, S. W. Cheung, and T. I. Yuk, "A multiband slot antenna for GPS/WiMAX/WLAN systems," *IEEE Transactions on Antennas and Propagation*, vol. 63, no. 3, pp. 952–958, 2015.
- [14] B. Yildirim, E. Basaran, and B. Turetken, "Dielectric-loaded compact WLAN/WCDMA antenna with shorted loop and monopole elements," *IEEE Antennas and Wireless Propagation Letters*, vol. 12, pp. 288–291, 2013.

## Research Article

# A Novel Compact Dual-Polarized Antenna

Yong Cheng,<sup>1</sup> Yadan Li,<sup>1</sup> and Wenjun Lu<sup>2</sup>

<sup>1</sup>College of Electronic Science and Engineering, Nanjing University of Posts and Telecommunications, Nanjing, Jiangsu 210003, China

<sup>2</sup>College of Communication and Information Engineering, Nanjing University of Posts and Telecommunications, Nanjing, Jiangsu 210003, China

Correspondence should be addressed to Yadan Li; [lyd2014ydl@163.com](mailto:lyd2014ydl@163.com)

Received 11 January 2016; Revised 10 April 2016; Accepted 8 May 2016

Academic Editor: Wenhua Yu

Copyright © 2016 Yong Cheng et al. This is an open access article distributed under the Creative Commons Attribution License, which permits unrestricted use, distribution, and reproduction in any medium, provided the original work is properly cited.

A novel compact dual-polarized antenna is proposed. The antenna has a 1.43% impedance bandwidth which is from 1801 MHz to 1827 MHz for return loss larger than 10 dB. The isolation between the two ports is above 28 dB in the bandwidth, and the gain is 6.6 dBi. The proposed antenna not only consists of a full-planar structure, but also is easy to be fabricated for its simple structure. Additionally, a section of slots and slits is cut on the radiation patch to reduce the area of it to 54% compared with the conventional square patch.

## 1. Introduction

Recently in modern wireless communication systems and mobile communications base stations, dual-polarized antennas are widely used to achieve polarization diversity, which can increase the capacity and reduce the installation costs. This is because the use of a dual-polarized antenna can reduce multipath fading and double the utilization rate of the frequency spectrum [1, 2].

Dual-polarized antennas with various kinds of structure are designed in the past decades of years. Roughly, the dual-polarized antennas can be divided into two categories: crossed dipole antennas and patch antennas. The crossed dipole antennas have different feeding structures, including C-shape [3], dielectric loading [4], differently driven [5], and shorting metal posts [6]. These feeding structures have been used for high isolation between the two ports. These dual-polarized crossed dipole antenna designs have accomplished bandwidth improvement, radiation pattern control, and so on, while none of these crossed dipole antennas has a full-planar configuration.

The dual-polarized patch antennas normally have a multilayer structure which may include coupling slots and L-shaped probe [7] or meandering probe [8], or a feeding network [9, 10] proposing a dual-polarized microstrip patch antenna fed through H-shaped coupling slots, which can

achieve high isolation and low cross-polarization. A simple dual-polarized antenna achieved by using proximity-coupled feedings was presented in [11]; the antenna achieves the bandwidth of 17% and an isolation of below 30 dB, but the frequency range from 3.07 GHz to 3.81 GHz is not suitable for mobile communications. A compact dual-polarized wide-band patch antenna array for the unlicensed 60 GHz band is designed in [12]. It provides a wide bandwidth for wireless high data rate communication systems while its fabrication process is very complex. Obviously these dual-polarized patch antennas with a multilayer structure have a complicated configuration. To improve those, a full-planar dual-polarized patch antenna with a simple configuration is proposed in this paper.

Good properties, such as high isolation and low cross-polarization levels, are necessary in a dual-polarized antenna, while the sizes are expected to be smaller by the public. Reference [13] proposes a double-polarization base station antenna; the antenna consists of two broadband base station antenna units, which make it has a large size. To reduce the area of the patch antenna, many methods have been used. Among them the most common one is to cut slots on the patch. Reference [14] proposes a single-feed circularly polarize patch antenna; the antenna uses U-slot loaded patch technique to effectively reduce the resonant frequency. In [15], there are two mirror imaged slots placed at the back of each

radiating element in ground plane for reducing operating frequency while maintaining the patch size. In [16], a novel single-feed circularly polarized microstrip antenna is proposed which uses a cross slot in the center of the patch and four slits on the edge to reach compact size. Besides using slots, some other technologies also had been taken. In [17, 18], the proposed antennas used substrates with large thickness and L-probe feeding structures were used to reach the impedance matching.

In this paper, we propose a full-planar dual-polarized antenna with a simple and more compact configuration operating at global system for mobile communication (GSM) frequency 1.8 GHz. The antenna consists of a single-layer structure and two coaxial probe feeds. It will be shown that this antenna has a 1.43% impedance bandwidth and has good isolation between two feeding ports. Additionally, the area of the patch is effectively reduced by using a section of slots and slits.

## 2. Antenna Design

This section describes the design of the dual-polarized antenna. The antenna is initially designed using heuristics and then the design is created by a commercial, electromagnetic field software HFSS. The profits of the proposed antenna can be optimized by adjusting the sizes of the structure.

The length  $L$  of the typical microstrip patch antenna can be calculated by the following equation, where  $\lambda_g$  is the guide wavelength on the substrate:

$$L = \frac{\lambda_g}{2}. \quad (1)$$

So, for the antenna without any slits or slots which works at 1.8 GHz, the length of the patch is about 39 mm.

A set of slots and slits are cut on the radiation patch to reduce its area [19]. With the slots and slits, the length of the current streamlines of the fundamental mode is increased, which can lower the resonant frequency. In another sense, the antenna proposed can use patch with smaller area to get the same resonant frequency. In the abstract, the quantity and sizes of the slots and slits determine the dimensions of the patch.

Figure 1 shows the geometry of the proposed dual-polarized antenna. The proposed antenna is printed on a  $60 \times 60 \text{ mm}^2$  FR4 substrate which has a thickness of 1.6 mm; relative permittivity  $\epsilon_r = 4.4$  and dielectric loss tangent  $\tan \delta = 0.02$ . A slotted square patch fed by two probes is on the front side of the substrate. On the back of the substrate is the ground plane with the same sizes as the surface of the substrate. The inner core of the coaxial cable is 1.2 mm in diameter while the outer core is 3 mm in order to achieve  $50 \Omega$  characteristic impedance. The two feeding ports are on two mutually perpendicular axes and have the same length to the center of the patch.

After careful simulation by the software HFSS, a resonant frequency of 1.8 GHz is obtained. The finally chosen dimensions of the proposed antenna are as follows:  $x_1 = 11 \text{ mm}$ ,  $x_2 = 7 \text{ mm}$ ,  $x_3 = 7.95 \text{ mm}$ , and  $x_4 = 8 \text{ mm}$ . The width of all of the slots and slits  $w$  is 1 mm. After simulation, with four L-shaped slots in the center and eight slits on the edges, the edge

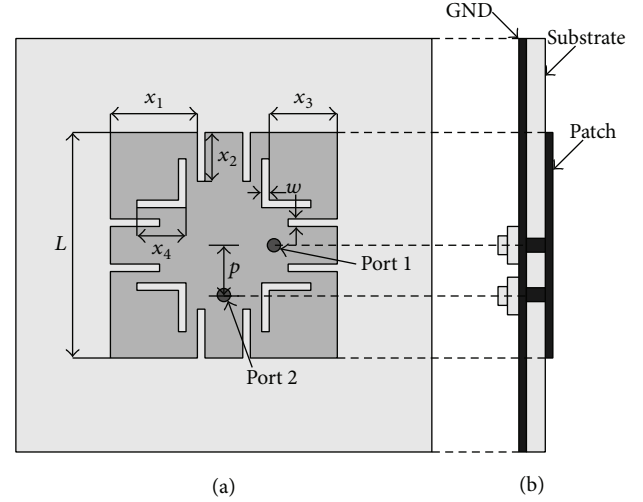


FIGURE 1: Geometry of the antenna: (a) front view; (b) lateral view.

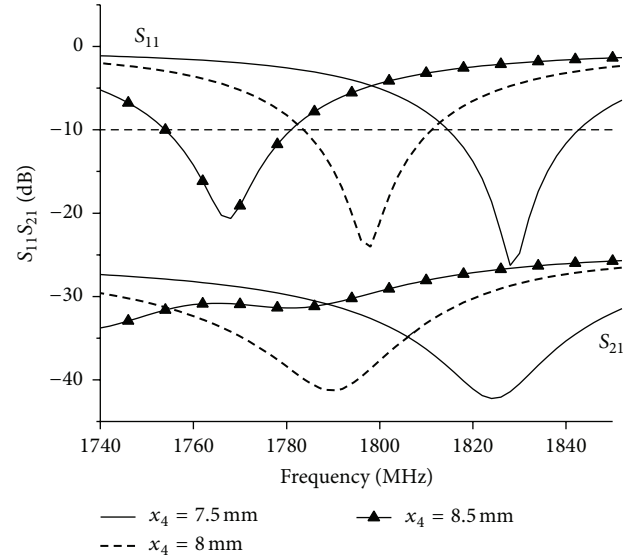


FIGURE 2: Simulated  $S_{11}$  and  $S_{21}$  with different values of  $x_4$ .

length  $L$  is reduced to 28.5 mm, which makes the area of the patch reduced to 54% compared with the conventional square patch.

The position of the ports, which is determined by the parameter  $p$ , influences impedance matching to a large extent. The parameter  $p$  is carefully picked in simulation and set to 5.3 mm.

## 3. Simulation and Measurement

The dimensions of the slots influence the resonant frequency a lot. Figure 2 shows  $S_{11}$  and  $S_{21}$  with different values of  $x_4$ . From the figure it is suggested that with increase of the length of the slots, the resonant frequencies of both  $S_{11}$  and  $S_{21}$  decrease. However, the slots cannot be too long. When  $x_4$  is increased to 8.5 mm, the isolation between two ports becomes

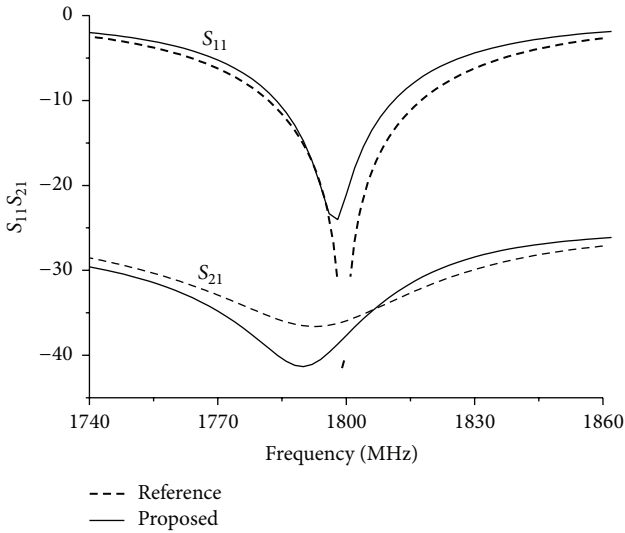


FIGURE 3: Simulated  $S_{11}$  and  $S_{21}$  of the proposed antenna and the typical one without any slots.

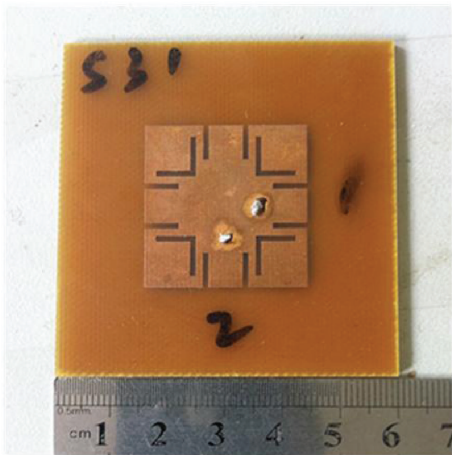


FIGURE 4: Fabricated proposed antenna.

weak and the return loss decreases a lot. At last, this parameter is selected as 8 mm.

After careful simulation, the final dimensions of the proposed antenna are confirmed. A comparison of the proposed one is made with the typical microstrip patch antenna without any slots, as shown in Figure 3.

The isolation of the typical antenna as reference is above 32 dB over the working bandwidth. While the proposed one is above 34 dB, which is slightly higher than the typical one.

The photograph of the fabricated proposed antenna is shown in Figure 4.

Figure 5 shows the simulated and measured return loss of the proposed antenna. As it is shown, the simulated antenna has a 1.5% impedance bandwidth which is 27 MHz from 1784 MHz to 1811 MHz for return loss larger than 10 dB. The simulated curves of  $S_{11}$  and  $S_{22}$  almost overlap because of the symmetrical structure of the antenna. The center frequency is 1800 MHz where the top return loss is

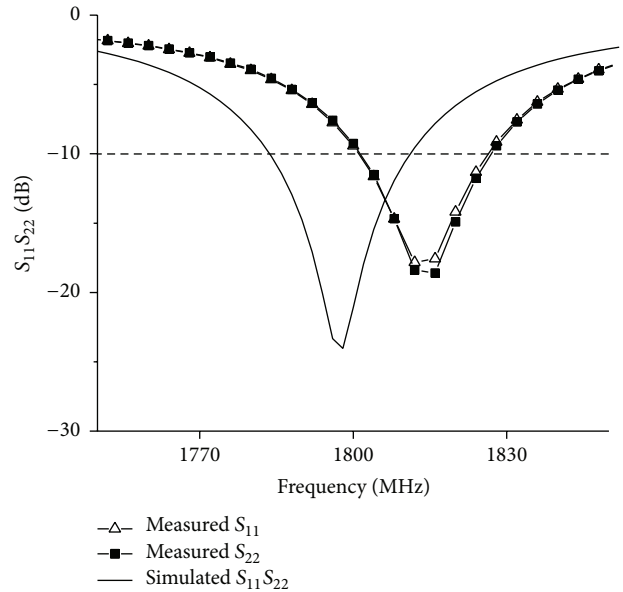


FIGURE 5: Simulated and measured return loss of the antenna.

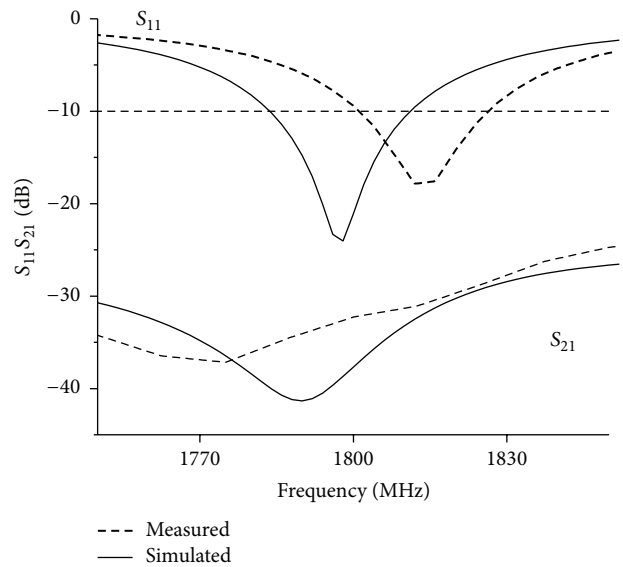
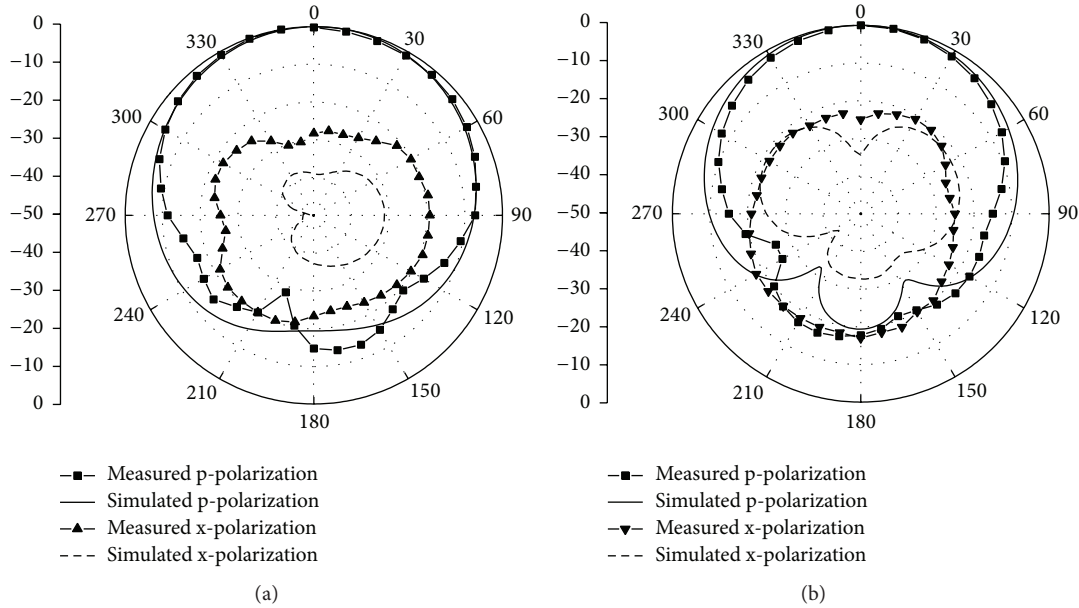
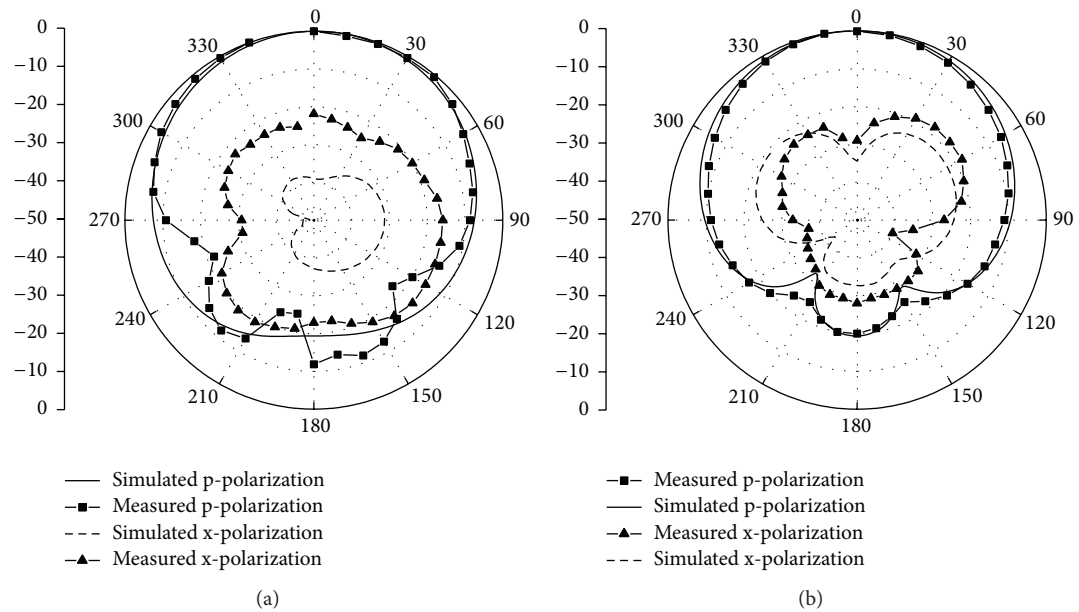


FIGURE 6: Simulated and measured  $S_{11}$  and  $S_{21}$  of the antenna.

23.6 dB. For the fabricated proposed antenna, the measured bandwidth is 26 MHz from 1801 MHz to 1827 MHz, and the top return loss at the center frequency 1814 MHz is 18.6 dB, which is smaller than the simulated result.

The isolation of the proposed antenna is illustrated in Figure 6. It shows that the simulated isolation is 38.6 dB at the center frequency 1800 MHz and is above 34 dB in the whole 10 dB impedance bandwidth. As measured, the isolation of the fabricated antenna is 31 dB at the center frequency 1814 MHz and is above 28 dB in the impedance bandwidth, which meets the design requirements. As for the difference between the measured and simulated center frequency, there are some reasons as follows: the actual permittivity of the substrate FR4 often ranges from 4.2 to 4.6, whereas 4.4 is just

FIGURE 7: Radiation patterns of port 1: (a) *E*-plane; (b) *H*-plane.FIGURE 8: Radiation patterns of port 2: (a) *E*-plane; (b) *H*-plane.

selected to simulate. The fabrication process may also make some differences, which makes the results different between the simulated one and the measured. Besides, the welding technology of the coaxial cable may also bring some errors.

It is observed from Figures 7 and 8 that the simulated radiation patterns of port 1 are the same as the ones of port 2 for the symmetrical structure of the antenna. But there are some differences in the measured results because of the deviations in fabrication and measure. Figures 7 and 8 are the simulated and measured principle polarization (p-polarization) and cross-polarization (x-polarization) patterns

in case of being fed by port 1 and port 2. As it is shown, the differences between measured patterns and those simulated are not much except a part of the x-polarization patterns has large deviations, which is due to the fact that the values are too small for the precision of measuring equipment to satisfy the demand. In the mass, the gain of x-polarization is 20 dB lower than that of p-polarization, which meets the requirement of dual-polarization design. The gain of the antenna is 6.6 dBi.

The current distribution on the patch surface is displayed in Figure 9. From the figure it can be seen that the currents are mainly distributed around the edge of the slots and slits and

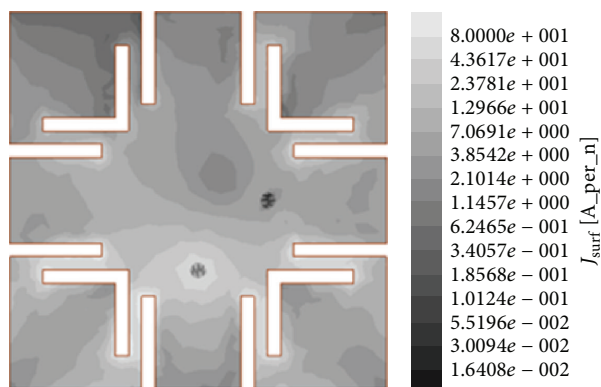


FIGURE 9: Simulated patch surface current magnitude distribution of phase 0 at 1.8 GHz.

at the corner of the patch the currents are weak. It indicates that the surface current path is effectively lengthened by the slots and slits.

#### 4. Conclusion

A novel slotted dual-polarized planar antenna is presented in this paper. This antenna is fed by two mutually perpendicular ports and operates around 1.8 GHz. A set of slots are used to reduce the area of the radiation patch. The measured results suggest that the proposed antenna has a 26 MHz bandwidth, in which the return loss is larger than 10 dB and the isolation is above 28 dB, and a maximum gain of 6.6 dBi.

#### Competing Interests

The authors declare that there is no conflict of interests regarding the publication of this paper.

#### Acknowledgments

This work was supported in part by a project funded by the Priority Academic Program Development of Jiangsu Higher Education Institutions (PAPD), Jiangsu Natural and Science Foundation of Universities under Grant no. 13KJA510002, Research Project of Nanjing University of Posts and Telecommunications (208035), and National Natural Science Foundation of China under Grant no. 61427801.

#### References

- [1] J. R. James and P. S. Hall, Eds., *Handbook of Microstrip Antennas*, Peregrinus, Stevenage, UK, 1989.
- [2] L. M. Burns and C. L. Woo, "Dual orthogonal monopole antenna system," US Patent no. 5990838, 1999.
- [3] B. Q. Wu and K.-M. Luk, "A broadband dual-polarized magneto-electric dipole antenna with simple feeds," *IEEE Antennas and Wireless Propagation Letters*, vol. 8, pp. 60–63, 2009.
- [4] L. Siu, H. Wong, and K.-M. Luk, "A dual-polarized magneto-electric dipole with dielectric loading," *IEEE Transactions on Antennas and Propagation*, vol. 57, no. 3, pp. 616–623, 2009.
- [5] Q. Xue, S. W. Liao, and J. H. Xu, "A differentially-driven dual-polarized magneto-electric dipole antenna," *IEEE Transactions on Antennas and Propagation*, vol. 61, no. 1, pp. 425–430, 2013.
- [6] S.-G. Zhou, P.-K. Tan, and T.-H. Chio, "Low-profile, wideband dual-polarized antenna with high isolation and low cross polarization," *IEEE Antennas and Wireless Propagation Letters*, vol. 11, pp. 1032–1035, 2012.
- [7] Y.-X. Guo, K.-W. Khoo, and L. C. Ong, "Wideband dual-polarized patch antenna with broadband baluns," *IEEE Transactions on Antennas and Propagation*, vol. 55, no. 1, pp. 78–83, 2007.
- [8] H.-W. Lai and K.-M. Luk, "Dual polarized patch antenna fed by meandering probes," *IEEE Transactions on Antennas and Propagation*, vol. 55, no. 9, pp. 2625–2627, 2007.
- [9] S. K. Padhi, N. C. Karmakar, C. L. Law, and S. Aditya, "A dual polarized aperture coupled circular patch antenna using a C-Shaped coupling slot," *IEEE Transactions on Antennas and Propagation*, vol. 51, no. 12, pp. 3295–3298, 2003.
- [10] S.-C. Gao, L.-W. Li, M.-S. Leong, and T.-S. Yeo, "Dual-polarized slot-coupled planar antenna with wide bandwidth," *IEEE Transactions on Antennas and Propagation*, vol. 51, no. 3, pp. 441–448, 2003.
- [11] S. Gao and A. Sambell, "Broadband dual-polarized proximity coupled circular patch antenna," *Microwave and Optical Technology Letters*, vol. 47, no. 3, pp. 298–302, 2005.
- [12] F. Wollenschläger, R. Stephan, L. Xia et al., "A compact dual-polarized wideband patch antenna array for the unlicensed 60 GHz band," in *Proceedings of the 5th European Conference on Antennas and Propagation (EUCAP '11)*, pp. 1873–1877, Rome, Italy, April 2011.
- [13] J. M. Zhou, "A design of 45-degree dual-polarization broadband plane station antenna," *International Journal of Antennas and Propagation*, vol. 2015, Article ID 297521, 9 pages, 2015.
- [14] K. Y. Lam, K.-M. Luk, K. F. Lee, H. Wong, and K. B. Ng, "Small circularly polarized U-slot wideband patch antenna," *IEEE Antennas and Wireless Propagation Letters*, vol. 10, pp. 87–90, 2011.
- [15] M. F. Ismail, M. K. A. Rahim, M. R. Hamid, H. A. Majid, and M. F. M. Yusof, "Compact dual-fed slotted circular polarization antenna with reflector for RF energy harvesting," in *Proceedings of the 7th European Conference on Antennas and Propagation (EuCAP '13)*, pp. 2096–2099, Gothenburg, Sweden, April 2013.
- [16] S. Kumar, B. K. Kanaujia, A. Sharma, M. K. Khandelwal, and A. K. Gautam, "Single-feed cross-slot loaded compact circularly polarized microstrip antenna for indoor WLAN applications," *Microwave and Optical Technology Letters*, vol. 56, no. 6, pp. 1313–1317, 2014.
- [17] J. Wu, X. Yang, Y. Yin, and F. Xu, "Wideband operations for compact single-fed circularly polarized microstrip antenna," *Microwave and Optical Technology Letters*, vol. 55, no. 6, pp. 1254–1257, 2013.
- [18] T. Wu, H. Su, L. Gan, H. Chen, J. Huang, and H. Zhang, "A compact and broadband microstrip stacked patch antenna with circular polarization for 2.45-GHz mobile RFID reader," *IEEE Antennas and Wireless Propagation Letters*, vol. 12, pp. 623–626, 2013.
- [19] D. L. Nguyen, K. S. Paulson, and N. G. Riley, "Reduced-size circularly polarised square microstrip antenna for 2.45 GHz RFID applications," *IET Microwaves, Antennas and Propagation*, vol. 6, no. 1, pp. 94–99, 2012.

## Research Article

# A Miniaturized Meandered Dipole UHF RFID Tag Antenna for Flexible Application

**Xiuwei Xuan, Lianrong Lv, and Kun Li**

*Tianjin Key Laboratory of Film Electronic and Communication Device, Tianjin University of Technology, Tianjin 300384, China*

Correspondence should be addressed to Xiuwei Xuan; [xiuweixuan@163.com](mailto:xiuweixuan@163.com)

Received 29 February 2016; Revised 27 April 2016; Accepted 3 May 2016

Academic Editor: N. Nasimuddin

Copyright © 2016 Xiuwei Xuan et al. This is an open access article distributed under the Creative Commons Attribution License, which permits unrestricted use, distribution, and reproduction in any medium, provided the original work is properly cited.

A miniaturized meandered dipole antenna for UHF RFID tag is proposed. Different resonance frequencies and impedance can be achieved by adjusting the number of the meanders, which can help to reduce the size of the antenna. Due to the radiation patches, the input impedance of the antenna can be flexibly tuned in a large scale. The proposed antenna is printed on polyethylene (PET) substrate with a total volume of  $48\text{ mm} \times 13.7\text{ mm} \times 0.5\text{ mm}$ . Modeling and simulation results show that the reflection coefficient of the antenna is less than  $-15\text{ dB}$  at  $860\text{--}960\text{ MHz}$ . Experimental studies demonstrate that the minimum threshold power of the antenna is between  $23$  and  $26\text{ dBm}$  and the measured read range is  $3\text{--}4\text{ m}$ .

## 1. Introduction

Radio Frequency Identification (RFID) is a noncontact automatic identification and data acquisition technology that uses radio waves. With the excellent features, such as no line-of-sight requirement, long operating range, and working under harsh environment, RFID is widely used in various information systems. Ultrahigh frequency (UHF) RFID has many advantages compared to low-frequency system, such as longer read range and faster data rate and programmability. UHF RFID technology has become popular in everyday life. A typical RFID tag consists of an antenna and an integrated circuit chip. UHF RFID system involves electromagnetic interaction between the antenna of tag and reader. Backscattering modulation will have good performance when the microchip matches its internal load to the antenna [1, 2]. The tag's antenna plays a key role in the system performance, such as read range, the power consumption of the microchip, and the overall size of the tag [3]. Since most UHF RFID tags are attached onto size-constrained objects, it is necessary to design small-geometry antennas with good radiation efficiency. To reduce the size of antenna, there are two strategies: meandering and inverted-F structures.

In order to reduce the size of the planar inverted-F antenna (PIFA), Zhang and Long embedded a slotted via-patch in the middle layer, which made the antenna input impedance flexibly tuned in a large scale [4]. However, the dual-layer antenna is complex for large scale production.

As proposed in [3], to operate on a plurality of materials for ubiquitous applications, antenna with sufficient bandwidth is necessary. The designed antenna can be mounted on a wide variety of dielectric materials of arbitrary thickness. As the permittivity increased, the resonance frequency decreased and the reflection coefficient increased, due to the amplitude-scaling factor. Microstrip antenna often reduces the antenna size by using dielectric slab with a high permittivity or increases communication frequency [5]. However, due to the limited bandwidth and large structure, microstrip antennas are not suitable for some applications. Hence, it is desirable to design small low cost, low profile antenna for simple production process [6]. According to Marrocco [2], the layout of the T-match has a considerable effect on the impedance of antenna. We adopt a T-match network to get a broadband performance.

This paper concentrates on the design of an electrically small flexible tag antenna with high efficiency, simple structure, and low cost. By changing the structure of dipole, we can

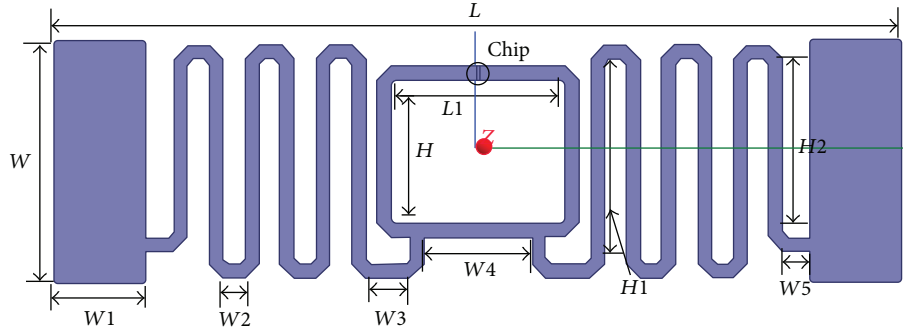


FIGURE 1: Structural configuration of the proposed antenna.

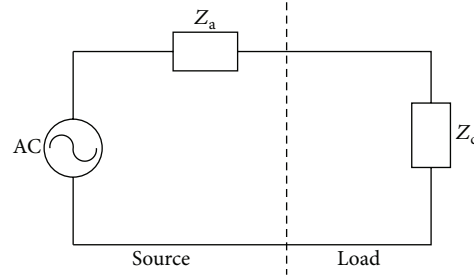


FIGURE 2: The equivalent circuit with two complex impedance instances.

adjust the input impedance of the antenna, so it can match its impedance to the microchip.

## 2. Antenna Configuration

In this section, we present a miniaturized UHF RFID tag antenna with a similar structure to that of 9662, manufactured by Alien Technology. The structural configuration of the antenna is illustrated in Figure 1. The antenna consists of a loop for feeding, a meandered dipole, and two radiators. The coupling between the loop and the dipole is adjusted by the distance between them and the size of loop [7].

The input impedance of the antenna in Figure 1,  $Z_a$ , is given by

$$Z_a = R_a + jX_a = Z_{\text{loop}} + \frac{(2\pi fM)^2}{Z_{\text{md}}} + Z_{\text{rad}}, \quad (1)$$

where  $Z_{\text{loop}}$ ,  $Z_{\text{md}}$ , and  $Z_{\text{rad}}$  are the individual impedance of the loop, meandered dipole, and radiator, respectively.  $M$  is the mutual inductance between the loop and meandered dipole.

We can see the tag as a one-port network, shown in Figure 2, which represents an antenna-chip circuit with complex source and load impedance. The power reflection coefficient between the antenna and chip  $|S_{11}|^2$  shows what fraction of the maximum power available from the generator is not delivered to the load:

$$|S_{11}|^2 = \left| \frac{Z_c - Z_a^*}{Z_c + Z_a} \right|^2, \quad 0 \leq |S_{11}|^2 \leq 1, \quad (2)$$

where  $Z_c = R_c + jX_c$  is the chip impedance and  $Z_a = R_a + jX_a$  is antenna impedance.  $Z_a^*$  is the conjugate of  $Z_a$ .

The power transmission coefficient  $\tau$  is given by [8]

$$\tau = 1 - |S_{11}|^2 = 1 - \left| \frac{Z_c - Z_a^*}{Z_c + Z_a} \right|^2 = \frac{4R_c R_a}{|Z_c + Z_a|^2} \leq 1. \quad (3)$$

The activation distance of the tag  $r$  can be calculated using Friis free-space formula as [8]

$$r = \frac{\lambda}{4\pi} \sqrt{\frac{P_t G_t G_r \tau}{P_{\text{th}}}}, \quad (4)$$

where  $\lambda$  is the wavelength,  $P_t$  is the power transmitted by the reader,  $G_t$  is the gain of the transmitting antenna,  $G_r$  is the gain of the receiving tag antenna, and  $P_{\text{th}}$  is the minimum threshold power to activate the RFID tag chip.

The impedance matching between the antenna and the chip is the primary factor that affects the performance of the antenna. To match the input impedance to the complex impedance value of Higgs-3, a meandered dipole and inductively coupled feed are utilized. The antenna is printed on PET substrate with a thickness of 0.5 mm, a relative permittivity of 2.25, and a dielectric loss tangent of 0.001. The antenna is designed to conjugately match the passive IC chip of Alien Higgs-3 at around 920 MHz. We choose etched aluminum to manufacture the antenna.

*2.1. Antenna with Different Number of Meanders.* In order to validate the design procedure, antennas with different

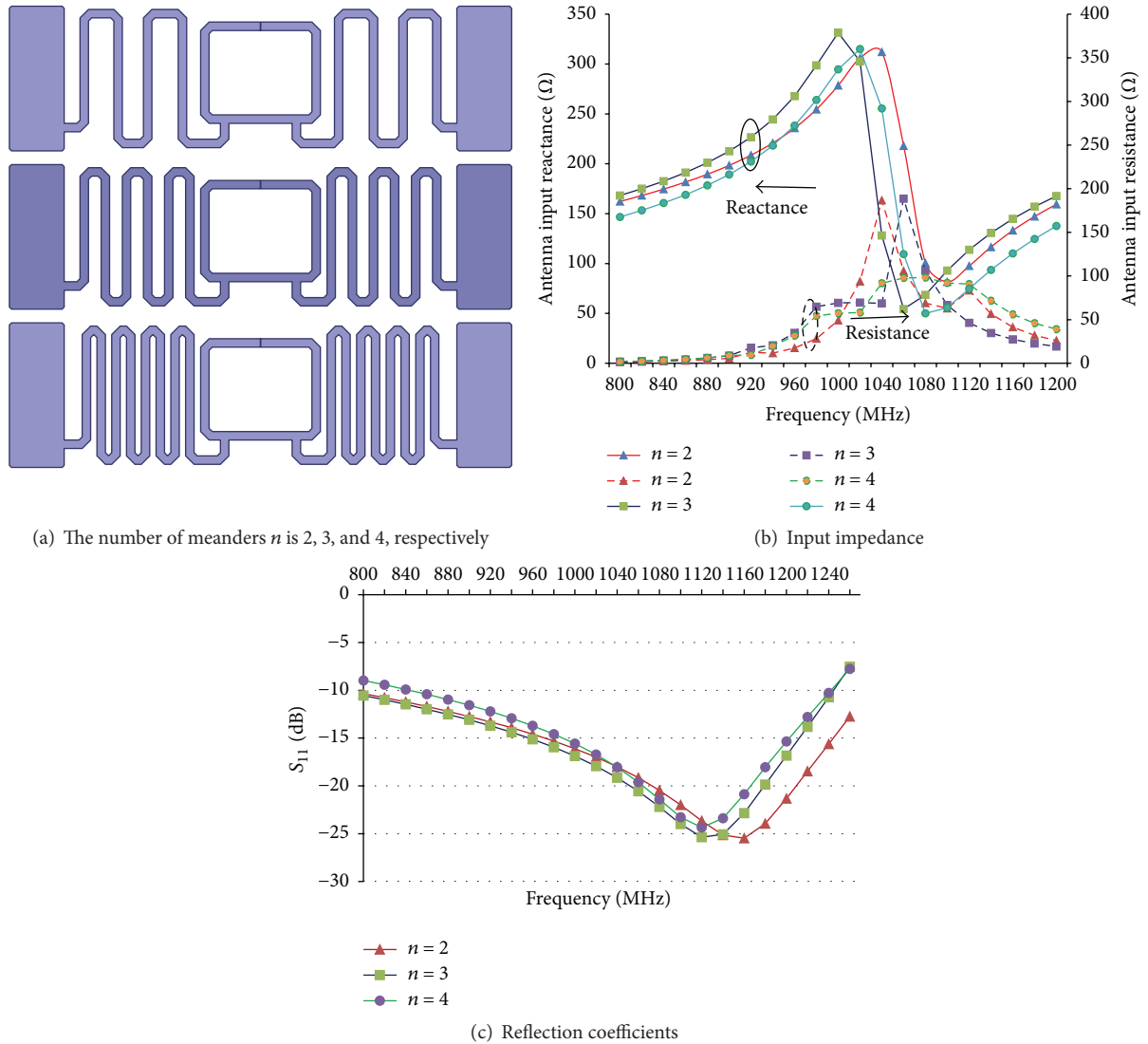


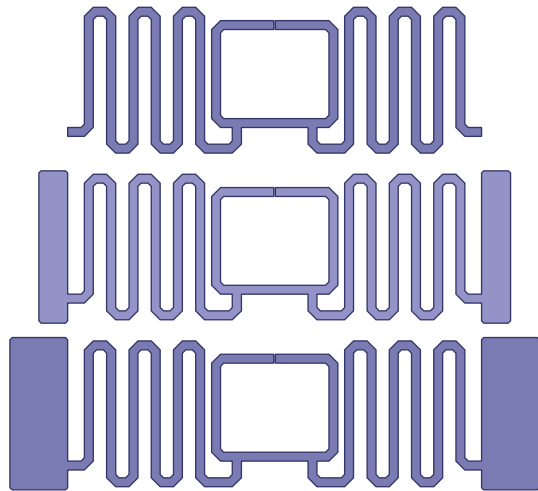
FIGURE 3: Simulated input impedance and reflection coefficients of tag antenna with different meanders.

number of meanders are modeled and simulated using full-wave simulator Ansoft HFSS.  $n$  represents the number of the meanders. Figure 3 illustrates the antenna input impedance and reflection coefficients when  $n = 2, 3, 4$ , respectively.

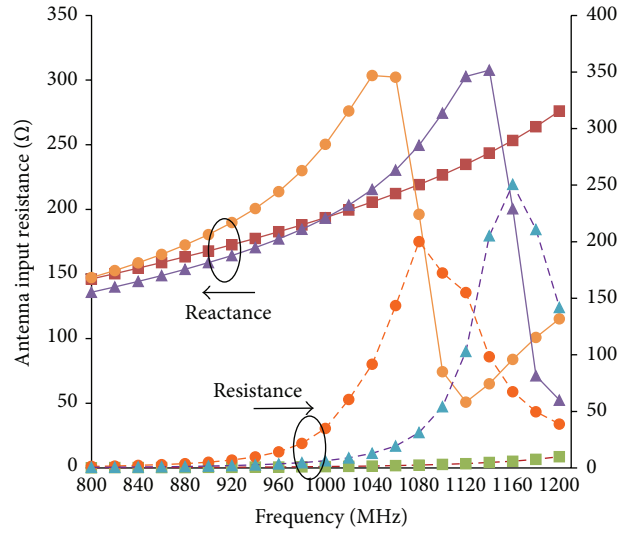
In Figure 3(a), the three antennas have the same total size with different number of meanders. Figure 3(b) shows the impedance characteristic of the three antennas. We can discover that the number of meanders could effectively tune the input impedance of the antenna. Figure 3(c) indicates the corresponding reflection coefficient of  $S_{11}$ . It can be seen that the  $-3$  dB bandwidth stretches across 860–960 MHz, which covers the entire UHF RFID band. As the number of meanders increases, the distances between them become closer and cause more offset coupling. According to Expression (1), the impedance of the meandered dipole  $Z_{md}$  decreases. That is to say, by independently adjusting  $n$ , the conjugate impedance matching different microchips can be easily realized.

**2.2. Antenna with Different Radiators.** Figure 4 illustrates the input impedance and reflection coefficients of antennas with different radiators when  $n = 3$ . The first antenna does not have a radiator. The second antenna has a radiator with width  $W_1 = 2.6$  mm, while the third antenna has a radiator with width  $W_1 = 5.2$  mm. Since a larger radiator has greater impedance, we can easily control the antenna impedance and  $S_{11}$  by changing the width of the radiator, which can be proved by Figures 4(b) and 4(c). Noting that impedance increases with  $W_1$ , we can get conjugate impedance matching different microchips by adjusting  $W_1$ . Similarly, different resonant frequencies and  $-3$  dB bandwidth can also be realized with different  $W_1$ .

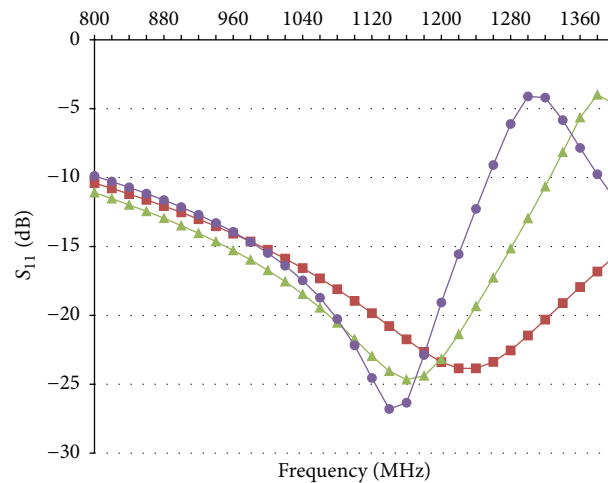
**2.3. Antenna with Different Size of Loops.** Figure 5 illustrates the input impedance and reflection coefficients of antennas with different size of loop when  $n = 3$ . The first antenna



(a) The width of radiators  $W1$  is 0 mm, 2.6 mm, and 5.2 mm, respectively



(b) Input impedance



(c) Reflection coefficients

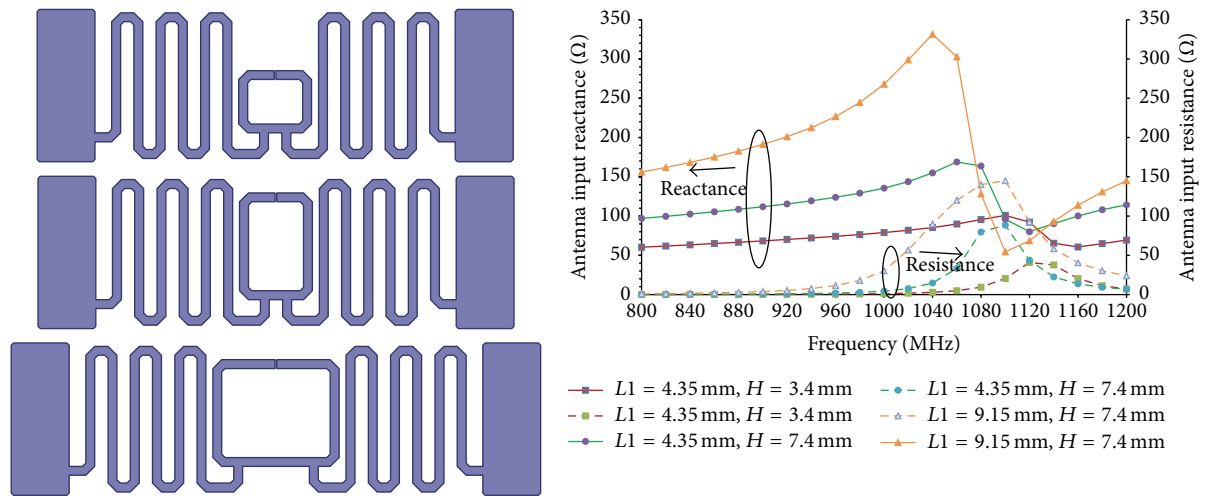
FIGURE 4: Simulated input impedance and reflection coefficients of tag antenna with different radiators.

has a loop with  $L1 = 4.35$  mm and  $H = 3.4$  mm. The second antenna has a loop with  $L1 = 4.35$  mm and  $H = 7.4$  mm, while the size of the loop in the third antenna is  $L1 = 9.15$  mm, with  $H = 7.4$  mm. Figure 5(b) presents that the imaginary part of the antenna impedance is largely determined by the size of the loop. By comparing  $S_{11}$  characteristics of the three antennas in Figure 5(c), we can discover the power reflection coefficient decrease when the size of loop increases. According to Expression (1), loop with larger size has higher impedance  $Z_{loop}$ . Meanwhile, the mutual inductance between the loop and meandered dipole will also increase. Therefore, the conjugate impedance matching

different microchips can be easily realized by adjusting the size of loop.

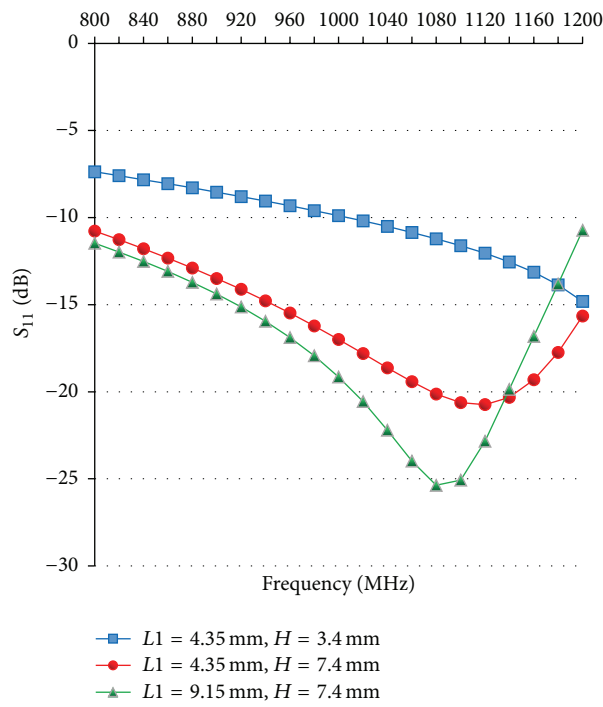
### 3. Antenna Design and Characteristics

In this design, we fix the number of meanders  $n$  at 3 and the width of the radiator  $W1$  at 5.2 mm. The prototype antenna is designed for Alien Higgs-3 RFID chip, whose input impedance is  $Z = (19 - j119)\Omega$  at 925 MHz. A photograph of the fabricated tag is shown in Figure 6. The relevant parameters of the antenna are as follows:  $L = 48$  mm,  $W = 13.7$  mm,  $W1 = 6.2$  mm,  $W2 = 1.2$  mm,  $W3 = 2.5$  mm,



(a) Antennas with different size of loops

(b) Input impedance



(c) Reflection coefficients

FIGURE 5: Simulated input impedance and reflection coefficients of tag antenna with different loops.



FIGURE 6: Photograph of the proposed RFID tag and 9662.

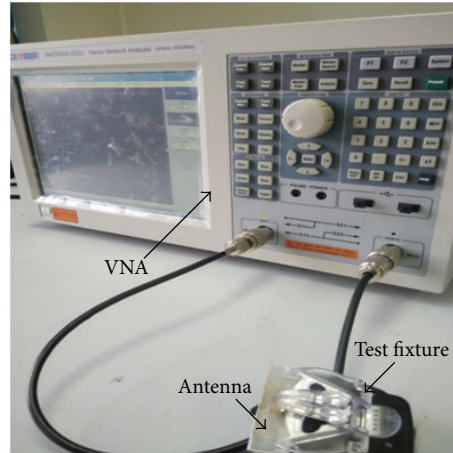


FIGURE 7: Measurement setup using VNA.

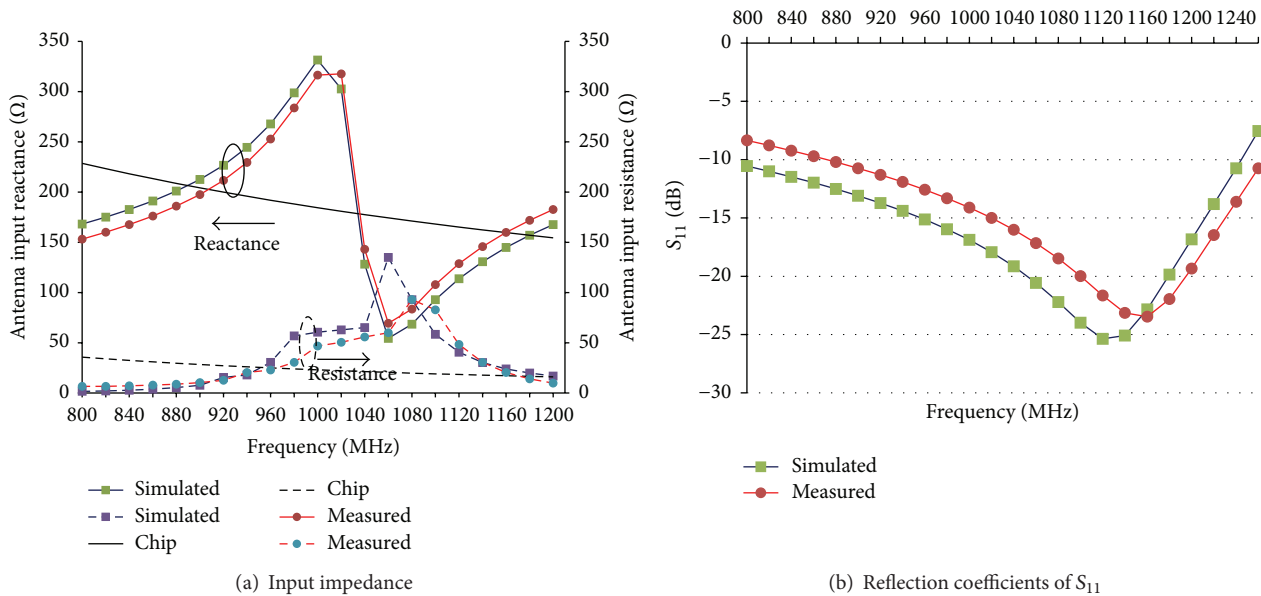


FIGURE 8: Impedance matching performance of the proposed antenna.

$W4 = 6$  mm,  $L1 = 9.15$  mm,  $H1 = 11.2$  mm,  $H2 = 9.7$  mm, and  $W5 = 1.5$  mm. The overall size of our miniaturized tag is  $48$  mm  $\times$   $13.7$  mm  $\times$   $0.5$  mm, while the size of 9662 is  $69$  mm  $\times$   $16$  mm  $\times$   $0.5$  mm.

In order to verify the matching performance, the impedance measurement was carried out using vector network analyzer (VNA) and the port-extension technique proposed in [9]. The configuration of the measurement system is illustrated in Figure 7.

Figure 8 shows the impedance characteristic and the reflection coefficient of the proposed antenna. In Figure 8(a), solid line represents the reactance while dashed line represents the resistance, and chip represents the conjugate value of tag chip's impedance.

The minimum threshold power as well as read range of the tag was measured in an anechoic chamber using a circularly polarized reader antenna with an effective isotropic radiated power (EIRP) of 4 W. From Figure 9, we can discover

that the minimum threshold power is between 23 and 26 dBm over the entire UHF RFID band. Figure 10 shows that the measured read range of the proposed tag is between 3 and 4 m. That is to say, the reading performance of the tag is stable over the entire UHF RFID band.

#### 4. Conclusion

A miniaturized and flexible RFID tag antenna with a total volume of  $48$  mm  $\times$   $13.7$  mm  $\times$   $0.5$  mm is proposed for the UHF RFID band. Different radiation patches and number of meanders can be employed to help get diverse input impedance and small size characteristics. The simulation study of the antenna has been carried out with the help of HFSS, while the measurement study has been implemented in an anechoic chamber. Both the simulation and measurement results indicate that the impedance matching performance is acceptable, which implies that the proposed antenna is

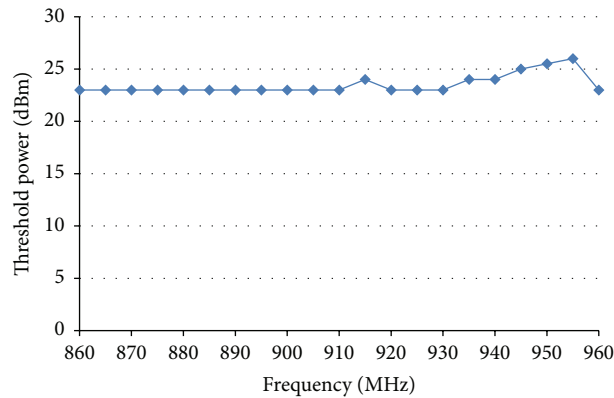


FIGURE 9: The minimum threshold power to activate the tag chip.

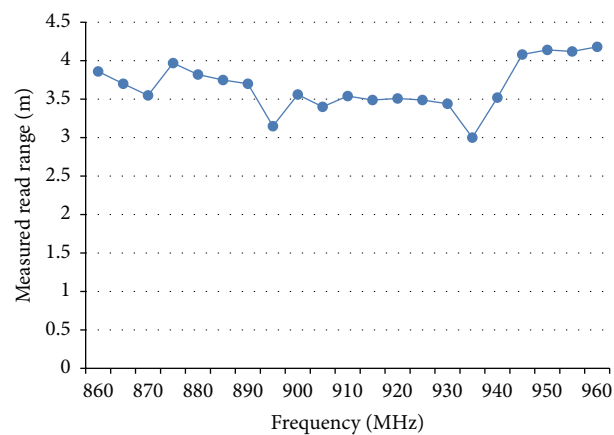


FIGURE 10: Measured read range of the proposed tag antenna.

a good candidate for miniaturized, flexible, and low-power consumption tags.

## Competing Interests

The authors declare that they have no competing interests.

## Acknowledgments

This work is supported by Natural Science Foundation of Tianjin (no. 13JCQNJC01300) and Tianjin Project of Science and Technology (no. 15ZLZLZF00300).

## References

- [1] S. X. Ta, I. Park, and R. W. Ziolkowski, "Crossed dipole antennas: a review," *IEEE Antennas and Propagation Magazine*, vol. 57, no. 5, pp. 107–122, 2015.
- [2] G. Marrocco, "The art of UHF RFID antenna design: impedance-matching and size-reduction techniques," *IEEE Antennas and Propagation Magazine*, vol. 50, no. 1, pp. 66–79, 2008.
- [3] S. Shao, R. J. Burkholder, and J. L. Volakis, "Design approach for robust UHF RFID tag antennas mounted on a plurality of dielectric surfaces [antenna designer's notebook]," *IEEE Antennas and Propagation Magazine*, vol. 56, no. 5, pp. 158–166, 2014.
- [4] J. Zhang and Y. Long, "A Miniaturized via-patch loaded dual-layer rfid tag antenna for metallic object applications," *IEEE Antennas and Wireless Propagation Letters*, vol. 12, pp. 1184–1187, 2013.
- [5] N. Sharma, A. K. Gautam, and B. K. Kanaujia, "Circularly polarized square slot microstrip antenna for RFID applications," *International Journal of Microwave & Wireless Technologies*, 2015.
- [6] B. Wang, "A compact antenna design for UHF RFID applications," *Progress in Electromagnetics Research Letters*, vol. 53, pp. 83–88, 2015.
- [7] W. Choi, H. W. Son, C. Shin, J.-H. Bae, and G. Choi, "RFID tag antenna with a meandered dipole and inductively coupled feed," in *IEEE Antennas and Propagation Society International Symposium (APS '06)*, pp. 619–622, Albuquerque, NM, USA, July 2006.
- [8] J. Zhang and Y. Long, "A dual-layer broadband compact UHF RFID tag antenna for platform tolerant application," *IEEE Transactions on Antennas and Propagation*, vol. 61, no. 9, pp. 4447–4455, 2013.
- [9] X. Qing, C. K. Goh, and Z. N. Chen, "Impedance characterization of rfid tag antennas and application in tag co-design," *IEEE Transactions on Microwave Theory and Techniques*, vol. 57, no. 5, pp. 1268–1274, 2009.

## Research Article

# An Optimal Electric Dipole Antenna Model and Its Field Propagation

Yidong Xu,<sup>1</sup> Lili Guo,<sup>1</sup> Wei Xue,<sup>1</sup> Korochentsev Vladimir,<sup>2</sup> and Junwei Qi<sup>1</sup>

<sup>1</sup>College of Information and Communication Engineering, Harbin Engineering University, Harbin 150001, China

<sup>2</sup>School of Engineering, Far Eastern Federal University, Vladivostok 690950, Russia

Correspondence should be addressed to Wei Xue; [xuewei@hrbeu.edu.cn](mailto:xuewei@hrbeu.edu.cn)

Received 4 February 2016; Revised 5 March 2016; Accepted 17 April 2016

Academic Editor: Christoph F. Mecklenbräuker

Copyright © 2016 Yidong Xu et al. This is an open access article distributed under the Creative Commons Attribution License, which permits unrestricted use, distribution, and reproduction in any medium, provided the original work is properly cited.

An optimal electric dipole antennas model is presented and analyzed, based on the hemispherical grounding equivalent model and the superposition principle. The paper also presents a full-wave electromagnetic simulation for the electromagnetic field propagation in layered conducting medium, which is excited by the horizontal electric dipole antennas. Optimum frequency for field transmission in different depth is carried out and verified by the experimental results in comparison with previously reported simulation over a digital wireless Through-The-Earth communication system. The experimental results demonstrate that the dipole antenna grounding impedance and the output power can be efficiently reduced by using the optimal electric dipole antenna model and operating at the optimum frequency in a vertical transmission depth up to 300 m beneath the surface of the earth.

## 1. Introduction

Electric dipole antennas have been widely used in Through-The-Earth (TTE) communication via a current injected into the earth at the power stage [1–3]. The Coal Mine Security Standard has many restrictions on the permissible transmission power of TTE communication systems. There are many methods which have been proposed and investigated to reduce the output power by changing the shape and material, increasing the interelectrode distance [4, 5], or using only one electrode with different kinds of material, such as parabol, copper braid extended aluminum foil, and steel rod [3]. However, these methods have not discussed the grounding impedance model of several electrodes in-array and still cannot reduce the electrodes grounding impedance to a level less than 300  $\Omega$ . Many reports take the contact impedance between the electrode and the earth into account [2] and suggest lowering it with resistance reducing material but have not given the quantitative relationship between them. Some models have been proposed and investigated the dipole antenna in two- or three-layered conducting medium [6–8]. However, most of them discuss the propagation from surface to surface or for far field transmission and have not given the optimal operating frequency to reduce the TTE

communication power in a stratified dissipative medium vertically. In [9], the author gives the electromagnetic wave radiation propagate in four-layered medium model in the VHF/UHF bands which is a great limitation for TTE communication. References [7, 10] have proposed the models of extremely low frequency electromagnetic field generated by submerged horizontal electric dipole (HED) in three-layer medium, where the field point and the source point are in the same layer. These models cannot be applied in practical TTE communication because the source point and the field point are not in the same layer.

To reduce the output power, a model for the parallel grounding impedance of several HED antennas arrayed in-line is presented and the quantitative relationship between the resistance reducing material and the impedance is proposed in this paper. It is found that the grounding impedance model of several electrodes in-array has good match with the experimental results, and the optimal electric dipole antenna can reduce the grounding impedance to less than 5  $\Omega$ . In order to further lower the output power and to improve communication quality, a full-wave electromagnetic simulation model for the electromagnetic field propagation in layered conducting medium is proposed, which is excited by the HED antennas. An optimum frequency for field

transmission at different propagation depth is carried out by this model. The receiver can get a maximum field when the TTE communication transmitter works at this optimum frequency, which is numerically and experimentally verified over a digital wireless system.

## 2. Modeling and Optimization of an Electrical Dipole Antenna

**2.1. HED Antenna Grounding Model.** Electric dipole antennas are used to inject electrical power into the earth by establishing galvanic coupling between the earth and the power stage of the transmitter. The frequency-dependent grounding impedance includes the wire impedance, the contact impedance between the wire and the electrode, the impedance of the electrode, the earth current divergence impedance, and the contact impedance between the earth and the electrode [2, 11, 12]. However, when the grounding impedance is in the frequency range of lower than 50 kHz, the grounding electrode exhibits the grounding impedance close to the grounding resistance [13]. In this paper, we investigate the earth current divergence impedance.

For a horizontal grounding electrode, with a length  $L$ , a diameter  $d$ , and an embedded depth  $h$ , six possible earth current divergence impedance models are presented in Table 1 [12].

For the sake of simplicity, the resistance of a horizontal grounding electrode with an embedded depth of zero can be expressed by the neutral-point potential method. This states that increasing the earth conductivity and the size of electrode can reduce its current divergence resistance. By placing several electrodes in parallel as one new electrode, the grounding impedance can be further reduced. The new grounding impedance  $R_d$  can be expressed as follows:

$$R_d = \frac{R_L}{n\eta}, \quad (1)$$

where  $R_L$  is the grounding impedance of a single electrode;  $n$  is the number of electrodes;  $\eta$  is the grounding electrode utilization factor, which is determined by the shape and number of electrodes and their relative positions.

The parallel resistance  $R_d$  can be similarly calculated by introducing a hemispherical grounding equivalent model [12]. For a horizontal grounding electrode buried at the subsurface level, its equivalent radius expression can be obtained based on image theory and the neutral-point potential method as

$$r = \frac{L}{2 \ln(2L/d)}. \quad (2)$$

For  $n$  parallel horizontal grounding electrodes arrayed in-line, the distance between two adjacent electrodes is  $D$ . In order to simplify the calculation, a radius ratio  $\alpha = r/D$  is defined. The injection current over each electrode is  $\{I_1, I_2, \dots, I_i, \dots, I_n\}$  with the electric potential  $V$ . The electric potential of the  $i$ th electrode as a reference electrode is given by  $\Phi_i = (1/\sigma)(1/2\pi r)I_i$ , based on the hemispherical grounding equivalent model. The electric potential provided

by the  $i \pm k$ th electrode at the  $i$ th electrode can be expressed as  $\Phi_{i \pm k} = (1/\sigma)(1/2\pi r)(\alpha/k)I_{i \pm k}$ . Then, we obtain the electric potential  $V = \sum_{i=1}^n \Phi_i$  by the superposition principle. By setting each electrode as reference, we have

$$\frac{1}{\sigma} \frac{1}{2\pi r} \begin{bmatrix} 1 & \alpha & \frac{\alpha}{2} & \cdots & \frac{\alpha}{n-1} \\ \alpha & 1 & \alpha & \cdots & \frac{\alpha}{n-2} \\ & & \ddots & & \\ \frac{\alpha}{i-1} & \cdots & 1 & \cdots & \frac{\alpha}{n-i} \\ & & \ddots & & \\ \frac{\alpha}{n-1} & \frac{\alpha}{n-2} & \frac{\alpha}{n-3} & \cdots & 1 \end{bmatrix} \begin{bmatrix} I_1 \\ I_2 \\ \vdots \\ I_i \\ \vdots \\ I_n \end{bmatrix} = \begin{bmatrix} V \\ V \\ \vdots \\ V \\ \vdots \\ V \end{bmatrix} \quad (3)$$

$$R_d = \frac{V}{\sum_{i=1}^n I_i} = \frac{R_L}{n\eta}$$

$$\alpha = \frac{r}{D}.$$

When  $n = \{2, 3, 4, 5, 6\}$ , the expressions of grounding electrode utilization factor  $\eta$  with argument radius ratio  $\alpha$  are obtained and shown in Table 2. The variations of  $\eta$  with  $\alpha^{-1}$  are shown in Figure 1.

From Figure 1, it can be seen that the grounding electrode utilization factor  $\eta$  decreases as the parameter  $\alpha$  increases for the same number of electrodes  $n$ . The main reason is that the shielding effect increases as the contiguous electrodes distance decreases, restricting the current injection into the earth. When there is no shielding effect between electrodes,  $\alpha$  becomes infinitely small and  $\eta$  tends towards 1.

The grounding impedance can be reduced when the grounding electrodes are surrounded by high conductivity resistance reducing material [14].

Semicylinder pits with length  $L$  and radius  $b$ , where  $b \ll L$ , are filled with resistance reducing material with conductivity  $\sigma_s$ . Metal horizontal grounding electrodes with length  $L$  and radius  $a = d/2$  are buried at the pit center. The transitional area is the area between the resistance reducing material and the surrounding soil which depends on the seepage property of the material, and it expands the pits to an equivalent radius  $b_m$ . The soil moisture, temperature, and soil gap have a significant influence on the resistance reducing material seepage property, meaning that  $b_m$  is variable but always larger than  $b$ , as shown in Figure 2.

The grounding resistance  $R_{\text{electrode}}$  is equivalent to a series connection circuit of  $R_{c1}$ ,  $R_{e1}$ ,  $R_{c2}$ , and  $R_{e2}$ , where  $R_{c1}$  is the contact resistance between the resistance reducing material

TABLE 1: Horizontal grounding electrode grounding resistance models.

Model	Formula
Rudenberg, Zingraff	$R = \frac{1}{\sigma} \frac{1}{2\pi L} \ln \frac{2L}{d} \left( 1 + \frac{\ln(L/2h)}{\ln(2L/d)} \right)$
Tagg, Dwight	$R = \frac{1}{\sigma} \frac{1}{2\pi L} \left( \ln \frac{4L}{d} + \ln \frac{L}{h} - 2 + \frac{2h}{L} - \frac{h^2}{L^2} + \frac{h^4}{8L^4} \right)$
Sunde, Schwarz	$R = \frac{1}{\sigma} \frac{1}{\pi L} \left( \ln \frac{2L}{\sqrt{dh}} - 1 \right)$
Neutral-point potential method	$R = \frac{1}{\sigma} \frac{1}{\pi L} \ln \frac{2L}{\sqrt{dh}}$
Average potential method ( $h = 0$ )	$R = \frac{1}{\sigma} \frac{1}{\pi L} \left( \ln \frac{4L}{d} - 1 \right)$
Neutral-point potential method ( $h = 0$ )	$R = \frac{1}{\sigma} \frac{1}{\pi L} \ln \frac{2L}{d}$

 TABLE 2: Functional relationships between  $\eta$  and  $\alpha$ .

Numbers of electrodes	Utilization factor $\eta$
2	$\frac{1}{1 + \alpha}$
3	$\frac{6 - 7\alpha}{6 + 3\alpha - 12\alpha^2}$
4	$\frac{12 - 10\alpha}{12 + 16\alpha - 23\alpha^2}$
5	$\frac{360 - 654\alpha + 241\alpha^2}{360 + 270\alpha - 1495\alpha^2 + 690\alpha^3}$
6	$\frac{2160 - 2952\alpha + 555\alpha^2}{2160 + 3312\alpha - 8439\alpha^2 + 2047\alpha^3}$

and the electrode,  $R_{e1}$  is the resistance reducing material current divergence impedance,  $R_{c2}$  is the contact resistance between the resistance reducing material and the earth, and  $R_{e2}$  is the earth current divergence impedance:

$$R_{\text{electrode}} = R_{c1} + R_{e1} + R_{c2} + R_{e2}. \quad (4)$$

$R_{e1}$  can be obtained by using

$$R_{e1} = \frac{1}{\sigma_s} \frac{1}{\pi L} \ln \frac{b_m}{a}. \quad (5)$$

It can be simplified by considering the semicylinder for the resistance reducing material and the current divergence impedance.  $R_{e2}$  of a horizontal semicylindrical electrode can be derived from a model of a vertical electrode grounding impedance and the principle of mirror image; that is,

$$R_{e2} = \frac{1}{\sigma} \frac{1}{\pi L} \ln \frac{L}{b_m}. \quad (6)$$

It can be seen that the resistance of the horizontal semi-cylindrical grounding electrode buried under the subsurface of the earth is equal to that derived by the midpoint potential method. The resistance reducing material has a gel-like property that keeps it in a certain shape and makes good

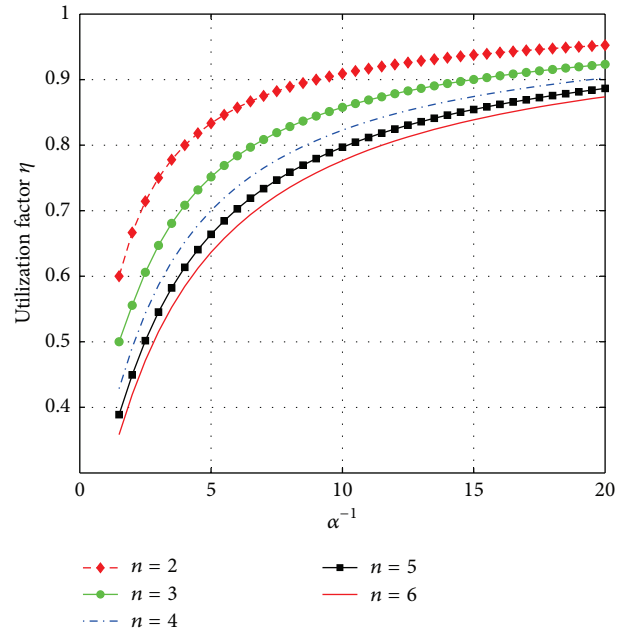
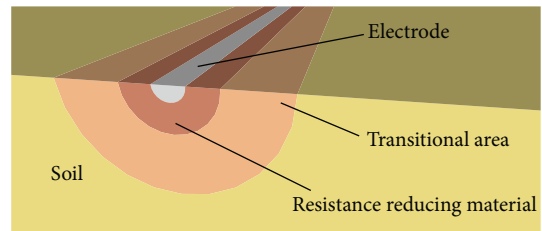

 FIGURE 1: Variation of utilization factor  $\eta$  with  $\alpha^{-1}$  under  $n$  dipole antennas.


FIGURE 2: Grounding electrodes surrounded by resistance reducing material with high conductivity.

electrical contact with the medium surface. Therefore, the impedances  $R_{c1}$  and  $R_{c2}$  can be negligible.

For demonstration purposes, it can be assumed that the conductivity of the moist soil is 0.05 S/m, and the

TABLE 3: Grounding impedance of electrodes and comparison between practical and theoretical utilization factor.

Electrodes configuration	Interval $m$	Number of electrodes	$\alpha$	Measured impedance $\Omega$	$\bar{\eta}$	$\eta$	Utilization factor deviation
A	0.5	1	1	21.00	1	1	1
	0.5	2	1	15.30	1	1	1
	0.5	3	0.46	11.82	0.59	0.58	2.8%
	0.5	4	0.46	10.65	0.49	0.51	-3.7%
	0.5	5	0.46	9.36	0.45	0.47	-4.6%
	1.0	2	0.23	13.14	0.80	0.81	-1.2%
	1.0	3	0.23	10.20	0.69	0.72	-4.2%
	1.5	2	0.15	12.83	0.82	0.86	-4.7%
	2.0	2	0.12	12.39	0.85	0.89	-4.5%
B	1.7	1	1	21.0	1	1	1
	1.7	2	1	13.11	1	1	1
	1.7	3	0.25	9.57	0.73	0.71	2.8%
	3.4	2	0.13	11.94	0.88	0.89	-1.1%

conductivity of the resistance reducing material is 2 S/m. The length of each grounding electrode  $L$  is 1.2 m with radius  $a = 0.035$  m and a grounding hemisphere equivalent radius of  $r = 0.17$  m. The earth current divergence impedance is  $18.6 \Omega$  when the horizontal grounding electrodes are buried at the subsurface of the earth directly without the resistance reducing material. If the horizontal grounding electrodes are buried in semicylindrical pits of radius  $b = 0.2$  m that are filled with resistance reducing material, which gives their equivalent radius  $b_m > b$ , in this case, we obtain  $R_{e1} = 0.25 \Omega$  and  $R_{e2} < 9.5 \Omega$ , meaning that the earth current divergence impedance  $R_{\text{electrode}} < 9.75 \Omega$ . It can be seen that the grounding impedance would be effectively reduced by filling the pit with the resistance reducing material. In order to reduce the grounding impedance to  $9.75 \Omega$  by using the grounding method without the resistance reducing material, there should be at least two electrodes placed parallelly with 3.4 m electrode interval, which would be an inefficient use of space and electrode material.

*2.2. Grounding Impedance Physical Experiment Simulation and Verification.* One set of experiments has been carried out on a sandy beach in Harbin. A stainless steel tube has been used as the test electrode, with length 1.2 m and diameter 0.14 m. An Agilent U1733C LCR meter has been used to measure the impedance.

There are two configurations for placing the antennas: several electrodes are placed in parallel and the distance between any two contiguous electrodes is  $D$  (configuration A), and the electrodes are placed in parallel in a head to tail configuration (configuration B).

The measurement results of the electrodes placed in configuration A and configuration B are shown in Table 3. According to the utilization factor expression in Table 2, the radius ratio can be written as  $\alpha = 2R_L/R_d - 1$  when  $n = 2$ . The radius ratio  $\alpha_0$  is 0.46 with the electrode interval 0.5 m in configuration A when  $R_L = 15.30 \Omega$  and  $R_d = 21.00 \Omega$ . For the electrode intervals 1 m, 1.5 m, and 2 m, the radius

ratios are  $\alpha_0/2$ ,  $\alpha_0/3$ , and  $\alpha_0/4$ . The radius ratio  $\alpha_1$  is 0.25 in configuration B when  $R_L = 13.11 \Omega$ . It is  $\alpha_1/2$  when the interval is 1.7 m. Substituting radius ratios into utilization factor models in Table 2, the theoretical utilization factor  $\eta$  can be derived. We can obtain the practical utilization factor  $\bar{\eta}$  based on (1).

The theoretical utilization factor matches the practical utilization factor well within a  $\pm 5\%$  deviation range. Compared with the electrodes placed in parallel, the grounding impedance of the electrodes arranged in parallel in a head to tail configuration is much smaller when they have the same gap. The arrangement of electrodes in parallel in a head to tail configuration increases the distance between each electrode because of its length, causing different grounding impedance. For instance, the interval in configuration A is 0.5 m with the gap 0.5 m but 1.7 m in configuration B, accounting 1.2 m in length of the electrode itself, and the grounding impedance is  $11.82 \Omega$  in configuration A and  $9.57 \Omega$  in configuration B. It has been proven that an impedance model of the horizontal grounding electrodes buried at the subsurface of the earth could be similarly calculated using the hemisphere grounding model. The electrodes arranged in parallel in a head to tail configuration are more suitable for applications such as in mines where there is a width restriction.

The experiment to optimize the antenna has been investigated at Xinqiang Mine in Qitaihe, Heilongjiang. The electrodes are buried in semicylindrical pits filled with resistance reducing material under the subsurface of the earth and in the mine and are parallelly arranged in a head to tail configuration. Each side of the antenna is composed of three electrodes, which are 1.3 m in length, 0.07 m in diameter, and at an interval of 1.5 m. The antennas are buried in pits that are 1.3 m in length and 0.3 m in diameter. The distance between two sides of the antenna on the ground is 40 m but 80 m within the mine. Moist clay is the predominant soil on the ground, which has a conductivity within the range of 0.01~0.05 S/m. The conductivity in mine is in the range of 0.005~0.02 S/m, due to the fact that the predominant soil is rock.

TABLE 4: Grounding impedance of electrodes on the ground and in the mine.

Frequency kHz	Grounding impedance of electrodes on the ground $\Omega$	Grounding impedance of electrodes in the mine $\Omega$
0.1	5.4	12.7
1	4.5	14.0
10	4.4	13.9

The impedance of each antenna is measured by an Agilent U1733C LCR meter, and the results are shown in Table 4.

As seen in Table 4, the impedance of the dipole antenna on the ground is about  $5 \Omega$ , indicating that the grounding impedance of each side of the antenna is less than  $2.5 \Omega$ . The conductivity in the mine tunnel is lower than that on the ground as the geological material within the mine is mainly rock. The impedance of the dipole antenna in the mine is  $13 \Omega$  and  $6.5 \Omega$  at each side of the antenna.

The output current ability of the TTE communication system and its range can be improved by placing the antennas in parallel in a head to tail configuration and filling the pits with resistance reducing material. This grounding model meets the requirement to reduce the underground communication systems' power.

### 3. Propagation of Dipole Antennas in a Semi-Infinite Layered Conducting Medium

*3.1. Simulation Model of Dipole Antenna in Layered Conducting Medium.* A numerical calculation of the electric field has been employed successfully in many applications, but it cannot describe the propagation successfully for complicated structures, such as layered conducting mediums [15]. To investigate the propagation of dipole antenna in layered conducting medium, the full-wave electromagnetic simulation model with the CST STUDIO SUIT electromagnetic tool is set up to accurately investigate the propagation.

According to a mine regional stratigraphic structural table, the Quaternary, Cretaceous, and Jurassic compositions are the main structural components of mines. The surface is a Quaternary system composed of alluvial sand. The middle layer is a Cretaceous system dominated by purple sandstone and grey-greenish mudstone on the upper layer and purplish-red conglomerate with mudstone in the lower layer. The bottom layer is a Jurassic system, with grey-greenish sandstone, conglomerate, mudstone, and marl on the upper level, volcanic rock, rhyolite, and mudstone in the middle level, and sandstone and conglomerate in the lower level. In order to reduce the influence of boundary conditions, the thickness of the air on the ground is set at 50 m, and the simulation area is 2000 m in length and width. The electrical parameters of these strata are shown in Table 5.

The full-wave electromagnetic simulation results with the CST STUDIO SUIT electromagnetic tool are presented with a moment  $p = 100 \text{ A}\cdot\text{m}$  on the dipole antenna. To understand the full-wave propagation characteristics of the dipole in the

TABLE 5: The electrical parameters of strata.

Strata	Attribute	Conductivity S/m	Thickness m
Quaternary	Alluvial sand, clay	0.01	20
	Sandstone	0.006	180
	Coal	0.01	2
Cretaceous	Conglomerate	0.01	200
	Coal	0.01	3
	Conglomerate mixed with mudstone	0.008	160
Jurassic	Marl	0.003	260
	Volcanic rock	0.001	240
	Conglomerate	0.01	200

TABLE 6: Electric field of the field point.

Frequency kHz	Field strength at -200 m $\mu\text{V}/\text{m}$	Field strength at -300 m $\mu\text{V}/\text{m}$	Field strength at -600 m $\mu\text{V}/\text{m}$
0.1	174.0	56.0	8.8
0.3	187.5	65.2	12.2
1	204.3	66.6	9.0
1.5	204.5	61.9	6.3
2	199.7	56.2	4.5
3	183.7	45.3	2.4
5	147.4	29.0	0.84
10	81.8	10.4	0.096
20	28.2	1.9	0.003
30	11.2	0.5	0.0002
$f_M$ kHz	1.5	1.0	0.3
-3 dB bandwidth kHz	5.0	3.0	1.0

layered conducting earth, the dipole antenna working at operating frequency 1.5 kHz is simulated and shown in Figure 3. It is found that there is a huge change at the interface between every two mediums, making the propagation complicated. As the points investigated are far enough from the boundary, the boundary condition has little influence on the simulation results. The full-wave electromagnetic simulation results of the field point at positions of -200 m, -300 m, and -600 m are shown in Table 6.

As shown in the simulation results, there is an optimum frequency  $f_M$  at each propagation depth. For the field point at position -200 m,  $f_M$  is 1.5 kHz with a -3 dB bandwidth 5 kHz. When the field point is located at position -300 m,  $f_M = 1.0$  kHz and the -3 dB bandwidth decreases to 3 kHz. For the field point at -600 m,  $f_M$  is 0.3 kHz and the -3 dB bandwidth is 1 kHz. In this instance,  $f_M$  and the -3 dB bandwidth decrease as the distance between the source point and the field point increases. For extremely low frequency, the electric field at the field point shows characteristic of a static

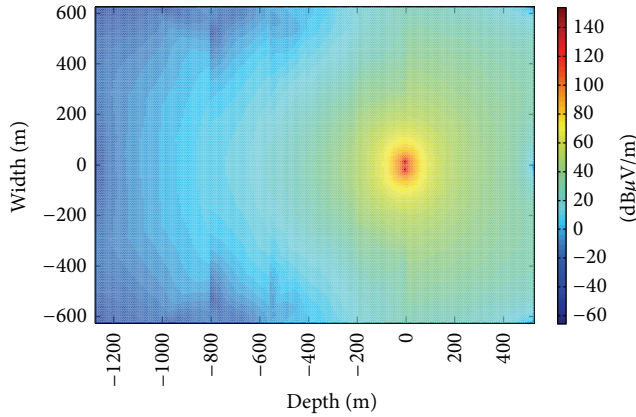


FIGURE 3: Propagation of the dipole in layered conducting earth at operating frequency 1.5 kHz.



FIGURE 4: TTE communication experiment in the mine.

field, and the bandwidth lower than  $f_M$  is within the  $-3$  dB bandwidth. A further simulation result has concluded that when the communication distance is within a range of 200~600 m vertically and the conductivity of the earth is within 0.001~0.05 S/m, the most favorable operating frequencies are below 10 kHz.

### 3.2. Field Experiment for the Propagation of a Dipole Antenna.

As shown in Figure 4, a set of experiments has been carried out at Xinqiang Mine in Heilongjiang Province. The test point at the mine is 300 m from the test point on the ground vertically and 300 m in straight-line distance from the wellhead horizontally. The test point is not connected with the lift shaft directly so that the electromagnetic energy cannot propagate along that. The interelectrode distance for the antenna in the mine is 80 m and for the antenna on the ground is 40 m. The dipole antenna on the ground is parallel to that in the mine, with their azimuth at  $260^\circ$ .

For the propagation measurement, the signal source, power amplifier, low noise linear amplitude to amplify the voltage on the dipole antenna, and scope to store the wave data are used. The power signal output by the power amplifier

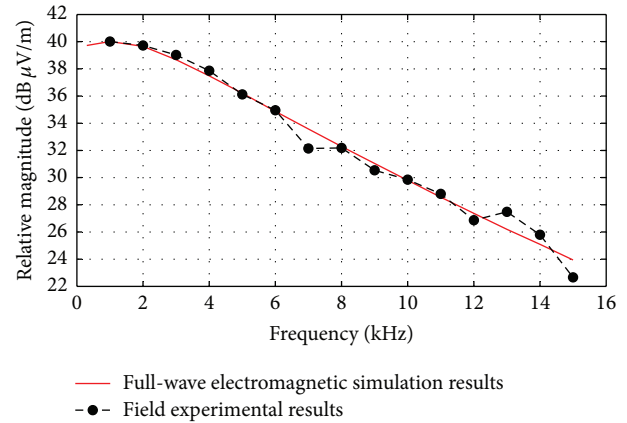


FIGURE 5: The full-wave electromagnetic simulation results and the field experimental results curve.

is loaded onto the dipole antenna, with an operating frequency in the range of 1~15 kHz. The power stage and the dipole antenna are connected by a multifiber copper wire with a length in the range of 20~40 m. There is an additional inductive-resistive component on the total impedance. Therefore, the power amplifier output should be regulated so that the moment on the antenna is a fixed value of  $p = 100$  A·m.

The full-wave electromagnetic simulation model with the CST STUDIO SUIT electromagnetic tool is set, where the thickness of the air on the ground is 50 m, and the simulation area is 2000 m in length and width. The upper layer of the earth is alluvial sand and sandstone with the thickness of about 180 m and conductivity 0.007 S/m. The next layer is conglomerate and coal with the thickness of about 200 m and conductivity 0.005 S/m. The bottom layer is mudstone with the thickness of about 160 m and conductivity 0.008 S/m. Figure 5 shows a comparison of the relative magnitude of the full-wave electromagnetic simulation results and field experimental results.

From Figure 5, the magnitude decreases as the frequency increases, with a slope of about  $-1.2$  dB/kHz for the frequency higher than 3 kHz, but for lower frequency the slope tends to be stable. It can be seen from Table 7 that most of the linear errors between the simulation results and the experimental results are less than 6%. Four of the linear errors deviate from normal value because of the tone interference at certain frequency. But the experimental results are close to the simulation results in Figure 5, indicating that the electromagnetic tool can represent the propagation of a dipole antenna in a layered conducting medium accurately. For the mine studied, the optimal frequency at a depth of  $-300$  m is 1 kHz.

## 4. TTE Communication for Mine

A TTE communication system for mines has been designed, which operates at frequencies of 2 kHz or 8 kHz, with a message data rate of 25 bps and 50 bps for digital voice information. It works in the half duplex, using 2DPSK modulation and demodulation technology. A high-performance speech

TABLE 7: The full region electromagnetic simulation results and the field experimental results.

Frequency kHz	Simulation results dB $\mu$ V/m	Experimental results dB $\mu$ V/m	Linear error %
0.3	39.72	†	†
1	40.01	40.01	0.00
2	39.65	39.72	0.81
3	38.67	39.02	4.11
4	37.48	37.86	4.47
5	36.21	36.12	-1.03
6	34.87	34.95	0.93
7	33.58	32.14	-15.28
8	32.29	32.18	-1.26
9	31.04	30.54	-5.59
10	29.80	29.85	0.58
11	28.56	28.80	2.80
12	27.37	26.87	-5.59
13	26.19	27.48	16.01
14	25.09	25.80	8.52
15	23.94	22.66	-13.70

compression MDV chip is used, with an ultralow voice coding rate of 600 bps. Digital voice data are error correction coded, stored in a buffer, and then transmitted with a low data rate.

The TTE communication experiment has been performed in Xinqiang Coal Mine, Heilongjiang Province. A dipole antenna is placed in the pits with radius 0.2 m filled with a resistance reducing material. Each side of the antenna includes 3 electrodes that are 1.2 m in length and 0.7 m in diameter, parallelly arranged in a head to tail configuration, with a gap of 1 m. The antenna impedance on the ground is reduced to 8  $\Omega$ , with a 40 m electrode interval. The impedance of the antenna in the mine is reduced to 13  $\Omega$ , with an 80 m electrode interval. Thus, the grounding impedance is effectively reduced compared with that in [3]. For an efficient transmitter, the transformer turn ratios 1.4:1 and 1.8:1 are fixed in order to match the ideal power stage load value 4  $\Omega$  [3]. The vertical distance from the ground to the tunnel of the mine is 300 m. The results show that the short message and digital voice can be effectively received at 8 kHz, when the output power is greater than 180 W. However, the system output power is only 30 W at the operating frequency 2 kHz with the same communication performance. Thus, the dipole antenna can be optimized using the optimal electric dipole antenna model and the communication output power can be reduced by transporting information at the carrier frequency  $f_M$ , which further proves the results in this paper.

## 5. Conclusions

In this paper, a grounding impedance model is presented for several horizontal electrodes placed in parallel. The analysis and contrast experiments have shown that the impedance of the dipole antenna on the ground is reduced to 5  $\Omega$  and 13  $\Omega$  in

the mine. Compared with the grounding impedance 300  $\Omega$  in [3], the optimal grounding impedance model can effectively reduce the grounding impedance.

The full-wave electromagnetic simulation model with the CST STUDIO SUIT electromagnetic tool can describe the propagation property of dipole in layered conducting medium and verified by field experiment. There is a single operating frequency for each field point at each depth of the layered earth that can achieve maximum field strength. The  $f_M$  in the full-wave simulation model at position -200 m is 1.5 kHz, 1 kHz at -300 m, and 0.3 kHz at -600 m. The operating frequency decreases as the communication distance or the earth conductivity increases. Thus, TTE communication is suitable for short range communication in the vertical direction.

It is shown that the TTE communication method could be successfully used for communication across a distance of 300 m vertically from the ground into the mine, with an output power reduced from 180 W at 8 kHz to 30 W at 2 kHz and an information data rate of 50 bps. The communication system can be placed in a fixed position and can be used for transmitting low data rate information, such as monitoring information or a distress signal in emergency situation.

## Competing Interests

The authors declare that they have no competing interests.

## Acknowledgments

This research has been supported by International Science & Technology Cooperation Program of China (2014 DFR10240), Harbin Science and Technology Research Projects (2013AE1BE003), Science Foundation of Heilongjiang Province QC2015075, and the Fundamental Research Funds for the Central Universities (China) [HEUCF1508].

## References

- [1] H. Wang, K. Zheng, K. Yang, and Y. Ma, "Electromagnetic field in air produced by a horizontal magnetic dipole immersed in sea: theoretical analysis and experimental results," *IEEE Transactions on Antennas & Propagation*, vol. 62, no. 9, pp. 4647–4655, 2014.
- [2] V. Bataller, A. Muñoz, P. M. Gaudó, A. Mediano, J. A. Cuchí, and J. L. Villarreal, "Earth impedance model for through-the-earth communication applications with electrodes," *Radio Science*, vol. 45, no. 6, Article ID RS6015, pp. 2970–2980, 2010.
- [3] V. Bataller, A. Muñoz, P. M. Gaudó, A. Mediano, J. A. Cuchí, and J. L. Villarreal, "Improving medium access in through-the-earth VLF-LF communications," *Journal of Communications*, vol. 4, no. 4, pp. 284–294, 2009.
- [4] A. A. Abdou, A. Shaw, A. Mason, A. Al-Shamma'a, J. Cullen, and S. Wylie, "Electromagnetic (EM) wave propagation for the development of an underwater Wireless Sensor Network (WSN)," in *Proceedings of the IEEE Sensors*, pp. 1571–1574, IEEE, Limerick, Ireland, October 2011.
- [5] G. Adw, *Channel Characterisation and System Design for Sub Surface Communications*, University of Leeds, Leeds, UK, 2003.

- [6] M. B. Kraichman, *Handbook of Electromagnetic Propagation in Conducting Media*, University of Michigan Library, 1970.
- [7] U. M. Cella, R. Johnstone, and N. Shuley, "Electromagnetic wave wireless communication in shallow water coastal environment: theoretical analysis and experimental results," in *Proceedings of the 4th ACM International Workshop on UnderWater Networks (WUWNet '09)*, pp. 1–8, Berkeley, Calif, USA, November 2009.
- [8] P. R. Bannister, "Quasi-static fields of dipole antennas at the earth's surface," *Radio Science*, vol. 1, no. 11, pp. 1321–1332, 1966.
- [9] Y. H. Xu, K. Li, and L. Liu, "Electromagnetic field of a horizontal electric dipole in the presence of a four-layered region," *Progress in Electromagnetics Research*, vol. 81, pp. 371–391, 2008.
- [10] C. Liu, L.-G. Zheng, and Y.-P. Li, "Study of ELF electromagnetic fields from a submerged horizontal electric dipole positioned in a sea of finite depth," in *Proceedings of the 3rd IEEE International Symposium on Microwave, Antenna, Propagation and EMC Technologies for Wireless Communications (MAPE '09)*, pp. 152–157, Beijing, China, October 2009.
- [11] S. Bourg, B. Sacepe, and T. Debu, "Deep earth electrodes in highly resistive ground: frequency behaviour," in *Proceedings of the IEEE International Symposium on Electromagnetic Compatibility*, pp. 584–589, Atlanta, Ga, USA, August 1995.
- [12] J. He and R. Zeng, *Power System Grounding*, Science Press, 2007.
- [13] K. S. Lee and Y. K. Chung, "Apparatus and method for calculating length of carbon grounding electrode module based on two-layered distributed constant circuit," Patent WO 2012050338 A3, 2013.
- [14] Z. Feng, L. Lu, and J. Feng, "Research on reducing grounding resistance of transmission line tower grounding grid," in *Proceedings of the 2nd Annual Conference on Electrical and Control Engineering (ICECE '11)*, pp. 1216–1219, Yichang, China, September 2011.
- [15] K. Li, *Fields and Waves in Layered Media*, Zhejiang University Press, Zhejiang, China, 2010.